Dormant viral pathways underlie space-induced neural senescence

Aline M.A. Martins[1,2†], Hideyuki Nakashima[3†], Angela Macia[4†], Taichi Umeyama[3], Satoshi Miyashita[5], Livia Luz de Souza Nascimento[1], Luisa Bulcao Vieira Coelho[1], Pinar Mesci[4], Erik Viirre[6], Nicole Suarez[4], Aurian Saleh[4], Alex Savchenko[4], Beatriz Freitas[4], Aline L. Leite[7], Diego M. Assis[7], Masataka Ishizu[3], Tomoo Owa[5], Mikio Hoshino[5], John Yates III[2], Kinichi Nakashima[3]* and Alysson R. Muotri[1,4,8]*

[1]Integrated Space Stem Cell Orbital Research Center, University of California San Diego, La Jolla, CA, USA.

[2]The Scripps Research Institute, La Jolla, CA, USA

[3]Department of Stem Cell Biology and Medicine, Graduate School of Medical Sciences, Kyushu University, 3-1-1 Maidashi, Higashi-ku, Fukuoka, Fukuoka 812-8582, Japan.

[4]Department of Pediatrics and Cellular & Molecular Medicine, School of Medicine, University of California San Diego, La Jolla, CA, USA.

[5]Department of Biochemistry and Cellular Biology National Institute of Neuroscience, National Center of Neurology and Psychiatry (NCNP) Tokyo 187-8502 Japan

[6]Department of Neurosciences, School of Medicine, University of California San Diego, La Jolla, CA, USA.

[7]Bruker Daltonics Corporation, Billerica, MA, USA.

[8]Kavli Institute for Brain and Mind, Center for Academic Research and Training in Anthropogeny, Archealization Center, La Jolla, CA, USA.

[†]These authors contributed equally to this work

*Correspondence: muotri@ucsd.edu or nakashima.kinichi.718@m.kyushu-u.ac.jp

SUMMARY

Long-duration spaceflight is associated with neurological symptoms in astronauts, yet the underlying molecular mechanisms remain unclear. Using human brain organoids cultured aboard the International Space Station, we analyzed three independent spaceflights to demonstrate that exposure to the space environment triggers Space-Induced Neural Senescence (SINS), characterized by chromatin remodeling, mitochondrial dysfunction, and activation of viral-like transcriptional programs in the absence of infection. Multi-omics analyses identified upregulation of endogenous LINE-1 (L1) retroelements, whose activity was markedly enhanced in organoids lacking MECP2, a known L1 repressor implicated in Rett syndrome. The resulting accumulation of cytoplasmic L1 DNA elicited an IL-6–mediated inflammatory and neurotoxic response, which was reversed by reverse transcriptase inhibitors (RTi) such as lamivudine or stavudine. Parallel preclinical experiments in *Mecp2*-deficient mice confirmed that RTi treatment restored neuronal morphology, synaptogenesis, function, cognition, and survival. These findings reveal that the space environment reactivates dormant genomic retroelements, providing an unexpected mechanistic insight into astronaut neurobiology and identifying a potential therapeutic strategy for both space-induced and terrestrial neurological conditions. Our pioneering study demonstrates the value of space-enabling research in accelerating drug discovery and disease treatment on Earth.

KEYWORDS

Brain organoids, space environment, proteomics, transcriptomics, L1, retroelements

INTRODUCTION

In recent years, human space exploration efforts have increased substantially, including the Artemis mission to land on the Moon in preparation for missions to Mars, as well as numerous private companies preparing to build the next generation of space stations in Low-Earth Orbit (LEO) to replace the International Space Station (ISS) [1]. As humans push farther into space, they face hazards like cosmic radiation and prolonged microgravity, which can cause a spectrum of physiological issues, including DNA damage, musculoskeletal degeneration, and neurological problems [2]. Space exposure is known to affect the astronaut's brain, as evidenced by changes such as increased ventricular volume [3,4], altered global white matter volume [5,6], and persistent cognitive decline post-flight [2-4,7-9]. However, the exact mechanisms remain unknown, largely due to limitations of current noninvasive brain imaging technologies. Therefore, successful long-duration exploration requires a comprehensive understanding of spaceflight's impact to develop effective countermeasures [10]. The SpaceX Inspiration4 mission highlighted the value of biomedical research in private space missions by collecting extensive health data, including multi-omic analyses. This contributes to the expanding biomedical database [11] and supports precision astronaut medicine. This "Second Space Age," characterized by commercial participation [12], provides diverse participant data from non-professional astronauts. Recent studies utilize multi-omics and systems biology to characterize the effects of spaceflight. Authors aggregated transcriptomic, proteomic, metabolomic, and epigenetic profiles, revealing alterations converging on mitochondrial and metabolic processes, innate immunity, chronic inflammation, cell cycle regulation, circadian rhythm, and olfactory functions [1-13]. Confirmed by NASA's Twin Study, mitochondrial dysregulation emerged as a consistent phenotype across multiple biological layers [14-16].

Although microgravity is the most recognized abiotic event in the space environment, radiation is among the foremost health risks facing astronauts during space missions, particularly long-duration exploration missions [14]. The chronic low-dose radiation exposure increases their risk of developing cancer, induces DNA damage, and triggers oxidative stress [14,17]. Radiation also contributes to neurological disruptions, such as neurovascular damage and neurodegeneration, in simulated models [18,19], potentially accelerating aging [18].

To understand how the space environment affects the brain, Masarapu and colleagues used single-nucleus multi-omics and spatial transcriptomics on mouse brains flown on the ISS for around 40 days [20]. This study revealed neuroinflammation, oxidative stress, and impaired synaptic signaling, consistent with findings in neurodegenerative disorders and radiation studies. However, similar studies cannot be conducted in humans; thus, the translatability of these observations is unclear.

Due to the inability to study astronaut brains at the cellular level, we used human brain organoids as a model system. These organoids mimic the functional and cellular features of the human brain [21], providing a unique experimental model for investigating the consequences of space exposure [22]. We developed an automated device to sustain organoid culture on the ISS and return live samples, with an Earth replica serving as ground control. Next, both proteomics and transcriptomics analyses were performed on the brain organoid samples returned from the ISS. One of the most representative molecular pathways upregulated in the flight samples relative to the ground control was associated with viral infection. In the absence of any additional viral infections, we hypothesized that this activation resulted from an increase in endogenous Long Interspersed Nuclear Elements-1 (LINE-1, or L1) retroelements. L1 elements are a class of retrotransposons comprising approximately 20% of the mouse and human genomes [23,24]. Several neurological and psychiatric diseases exhibited variation in L1 expression, suggesting L1s could be detrimental when de-regulated [25-31], especially in age-related neurodegenerative diseases [32,33]. The upregulation of this pathway is linked to a series of histone modifications, relaxing the chromatin, and alterations in MECP2, a well-known L1 repressor [34-38].

To translate our observations in space to a clinically relevant model on Earth, we studied L1 upregulation in Rett syndrome (RTT, OMIM#312750), caused by MECP2 mutations [39]. We show that increased L1 expression in MECP2-mutant human astrocytes triggers an Interleukin 6 (IL6)-mediated inflammatory neurotoxic response. Blocking L1 reverse transcription using reverse transcriptase inhibitors (RTi) ameliorates neurotoxicity, improving cognition and survival. Our results contribute to understanding the molecular mechanisms underlying the neurological consequences of spaceflight and offer potential neuroprotective countermeasures for astronauts and therapeutic opportunities for neurological conditions on Earth.

RESULTS

An autonomous platform for human brain organoids at ISS

To investigate how the space environment affects human brain organoids, we used a multi-modal approach, combining proteomics (mass spectrometry-based) and transcriptomics in two different levels of information (bulk and single-nuclei analysis). We used human brain organoids generated using a semi-guided protocol, a robust approach that yields consistent results across different iPSC lines [1,2]. Derivation of brain organoids using this approach yields clear neural rosettes with a spatially organized arrangement of proliferative cells, intermediate progenitor cells, glial cells, and lower- and upper-layer cortical neurons. Based on cell population annotation, 1-month organoids consisted of approximately 70% progenitor and radial glial cells (expressing markers such as SOX2) that would mature into functional neurons (NeuN2-positive) and astrocytes (GFAP-positive). Over the course of organoid maturation, neurons exhibit a characteristic pyramidal morphology, and mature synaptic ultrastructure

118 develops, enabling the formation of functional populations of inhibitory interneurons, which in turn
119 facilitate the establishment of complex neural circuitry. One-month-old human brain organoids from 3
120 iPSC lines derived from healthy individuals with different genetic backgrounds, plus a cell line with
121 mutated *MECP2* (MECP2-KO), were loaded into a 9U CubeLab™ hardware (Space Tango) on three
122 independent Commercial Resupply Services (CRS) using SpaceX (SpX) rockets missions (CRS-
123 SpX18, CRS-SpX30; CRS-SpX31), each lasting around 30 days at the ISS (**Fig. 1**), returning with two
124 months old. Space Tango's flight and ground hardware supported 12 wells, each equipped with
125 impellers and automated operations (fluid conveyance, fluid routing, thermal control, environmental
126 monitoring, imaging, and sampling), containing approximately 30 organoids (**Fig. 1** and **Fig. S1A**). The
127 organoids were monitored in real time in each well in both environments, the ground and the ISS units
128 (**Fig. S1A**). CubeLab environmental telemetry (CO_2 levels, culture medium temperature, and radiation)
129 was recorded during operations (**Fig. S1B and E,** and **Table S1**). As they return from the ISS at 2
130 months old, brain organoids are self-organized in a structure containing five major cell types –
131 progenitors, intermediate progenitors, glial cells, glutamatergic neurons, and GABAergic neurons, as
132 previously described (**Fig. S1C**). We also visually tracked the organoids' viability and overall health in
133 both environments, measuring their diameter during the experimental weeks (**Fig. S1D**). ISS and
134 ground samples were run synchronously, and scheduled operations were initiated simultaneously. Upon
135 return to Earth, the samples were processed for proteomic and transcriptomic analyses.

136 **Space-induced neural senescence - SINS**

137 The effects of the space environment on brain organoids revealed significant alterations in both
138 proteomic and transcriptomic profiles. A summary of all experiments performed in this study, including
139 flight missions and details of their statistical analyses, is provided in **Table S2**. In the proteomics
140 analysis, we identified an average of 6000 proteins per run and 4059 differentially expressed proteins
141 between brain organoids on Earth (ground control) and those exposed to the space environment at the
142 ISS ($p \leq 0.01$; fold change 1.2) (**Table S3**). Proteomic analysis of samples at the ISS-exposed to space
143 demonstrated a distinct set of upregulated proteins (**Fig. 2A**). Proteins such as tenascin (TNC);
144 neurofilament light polypeptide (NEFL); mitochondrial import inner membrane translocase (TIMM8A),
145 and subunit of cytochrome c oxidase (HIGD1A), show significant fold changes and p-values, implying
146 alterations on the metabolism of the brain organoids. Reactome pathway analysis identified key affected
147 pathways, including RNA metabolism, intracellular protein transport, and viral infection (**Fig. 2B**).

148 To evaluate the oxidation/phosphorylation (OxPHOS) state of the experiment, we performed an
149 enrichment analysis and observed the downregulation of the mitochondrial-related proteins in the ISS
150 (**Fig. 2C**). We found 629 downregulated proteins are significantly enriched in functions and pathways
151 crucial for cellular energy production (respiration) and the synthesis of mitochondrial proteins,
152 demonstrating that space environment causes a deep alteration in the energetic machinery in the brain
153 organoids. The most significantly affected molecular functions are related to the electron transport chain
154 and oxidoreductase activity. The most enriched biological pathway is associated with the citric acid
155 (TCA) cycle and respiratory electron transport, indicating that multiple aspects of mitochondrial protein
156 synthesis, including translation initiation, elongation, and termination, are significantly downregulated,
157 suggesting reduced capacity for building and repairing mitochondrial components (**Fig. 2C**).

158 We also observed alterations in epigenetic marks. Histones play a crucial role in regulating gene
159 expression by influencing chromatin structure and accessibility. Reduced histone levels can alter
160 chromatin dynamics, making DNA more accessible to transcription factors and enzymes involved in
161 DNA repair and replication [3]. Such alterations might reflect cellular responses to stress conditions and
162 cellular senescence[4]. Histones are globally downregulated in the ISS when compared to ground control
163 brain organoids **(Fig. 2D)**. Specifically, the histone acetyltransferases (HAT1 - histone acetyltransferase
164 type B; KAT8 - histone acetyltransferase KAT8; KAT7 - histone acetyltransferase KAT7), usually linked
165 to open chromatin, were upregulated at the ISS (**Fig. S2A,** upper panel). At the same time, we observed
166 downregulation of deacetylases at the ISS, indicating a withdrawal of acetyl groups (**Fig. S2A,** bottom
167 panel). Together, these observations suggest that cells in brain organoids exposed to the ISS undergo
168 chromatin remodeling, thereby facilitating genomic accessibility and overall transcription.

To further complement our proteomics analysis, we evaluated the secretome panel on a subsequent flight (Spx31), aiming to understand how the space environment altered the pattern of secreted effectors (**Fig. 2E**). The conditioned media of a batch of control brain organoids were analyzed using Olink Reveal® panel technology, a Proximity Extension Assay technology (PEA). The readouts were compared with an aliquot of unconditioned medium (blank) used to grow the organoids in the ISS, and this negative control was compared with each of the tested conditioned media. The data analysis revealed that the secretome of brain organoids exposed to a space environment exhibited a coordinated response of protein effectors in the ISS relative to ground control. The secretome panel highlight: *i*) modulation of neural development activity: the upregulation of secreted Glial Cell Line-Derived Neurotrophic Factor (GDNF) and sustained expression of Fibroblast Growth Factor 19 (FGF19) suggests an intrinsic adaptive mechanism where supportive glial cells respond to the unique demands of the space environment by enhancing trophic support and developmental cues, against space-induced cellular insults [5]; *ii)* alteration of proliferative state, impacting epigenetic regulation: downregulation in the ISS brain organoids of DPY30 (Dpy30 histone methyltransferase complex subunit), SMARCA4 (SWI/SNF related, matrix associated, actin dependent regulator of chromatin, subfamily A, member 4), TOP2B (DNA Topoisomerase II Beta) and MKI67 (marker of proliferation Ki-67) emphasizes changes in chromatin remodeling and gene expression regulation in the space environment, and a coordination of a robust epigenetic response[6]; *iii)* alterations in cytoskeletal dynamics and trafficking: together, the downregulation compared to ground samples of BAIAP2 (brain-specific angiogenesis inhibitor 1-associated protein 2), CAMSAP1 (calmodulin regulated spectrin associated protein 1) and ABL1 (ABL proto-oncogene 1, non-receptor tyrosine kinase) indicates a significant disruption or alteration in actin cytoskeleton organization and dynamics, that could lead to changes in cell shape, migration, and the formation of cellular protrusions essential for neuronal connectivity[7,8].

The bulk transcriptomic data also showed significant differential gene expression between the ground control and organoids at the ISS. We identified 150 differentially expressed genes (DEGs) with a 1.5-fold change and p-values <0.05. (**Table S4**). Most DEGs are involved in viral RNA translation, followed by selenocysteine synthesis and peptide chain elongation (**Fig. 2F**). Consistent with the proteomic pathway analyses, the transcriptional Reactome pathway analyses also uncovered activation of viral response pathways (**Fig. 2G**). Moreover, WikiPathway analyses revealed significant alterations in MECP2-related gene expression under space environment conditions (**Fig. 2H**). To determine whether the viral pathway could also be detected in the blood of astronauts, we compared our DEGs with those from the NASA Twins Project using Ingenuity Pathway Analysis (IPA). As expected, pathways related to the hematopoietic system (e.g., T-cell activation) are present only in the blood astronaut samples (**Fig. S2B**). The top hits across biological and disease pathways include several viral-related pathways, such as viral infection, retrovirus replication, and HIV infection, among others (**Fig. S2B**).

To determine which cell-type-specific responses were affected by the space environment at the ISS, we performed a single-nucleus transcriptomics experiment (snRNA-seq). We identify 10 cell populations in the brain organoids: lower-layer neurons, upper-layer neurons, radial glial cells, intermediate progenitors, glial cells, astrocytes, dividing neural progenitors, early neurons, pan-cortical neurons, and oligodendrocyte progenitor cells (**Fig. 2I** and **Fig. S2C**). Changes in cell populations were observed when we compared ground control and brain organoids exposed to the space environment (**Fig. 2J**). Mainly, we observed a higher number of active astrocytes (glial fibrillary acidic protein (GFAP)-expressing cells and transforming growth factor beta 2 (TGFβ2)-expressing cells) in organoids exposed to the space environment (**Figs. 2K-L**). We generate a heatmap of differentially expressed key marker genes across cell types. We observed distinct expression patterns across cell clusters, with GFAP expression with a higher intensity in astrocytes; forkhead-box G1 (FOXG1), B-cell lymphoma/leukemia 11b (BCL11b) and (glutamic acid decarboxylase) GAD1, with high intensity in upper- and lower-layer neurons and intermediate progenitors **(Fig. S2C)**.

We evaluated human brain organoids from another independent spaceflight (SpX30) to validate our previous findings using bulk transcriptomics. The subsequent spaceflight also revealed similar signaling pathways altered in the ISS, complementing the original observations from the SpX18 flight **(Fig. 2M)**. The analysis of the gene expression differences between brain organoids in the ground experiments

222 *vs*. brain organoids exposed to the ISS revealed: *i)* downregulation of non-coding RNAs: the
223 downregulation of LINC RNAs (Long Interspersed Non-Coding RNAs), such as LINC01873,
224 LINC02654, LINC01911. Interestingly, the primary function of these LINC RNAs is to suppress the
225 activity of retrotransposons, such as L1 elements; *ii)* cellular stress: the decreased expression of
226 CAPN13 (calpain 13), PNPLA1 (patatin-like phospholipase 1), and SLC22A14 (transmembrane solute
227 carrier family 22 member 14) indicates impairment of neurogenesis and reduction in cell proliferation
228 and long-term survival of neurons; suppressed oxidative phosphorylation, specially through
229 mitochondria deficiency in ATP production, leading to impaired in fatty acid beta-oxidation (FAO) and
230 reduction in acyl-carnitines and TCA cycle; *iii)* altered neurodevelopment and impaired plasticity: the
231 coordinated downregulation of key developmental genes – NPPB (natriuretic peptide B), MYO7B
232 (myosin VIIB), and CDH13-AS2 (long non-coding RNA (lncRNA) that plays a role in regulating the
233 expression of the CDH13 gene, also known as T-cadherin) indicates that the space environment may
234 hinder the brain's developmental genesis **(Fig. 2M).**

235 Collectively, all the changes in transcriptomics and proteomics described above represent a novel
236 phenomenon not observed on Earth. Thus, we coined the term "Space-Induced Neural Senescence"
237 (SINS) to distinguish it from the linear aging process observed on the ground. These findings provide
238 insights into the neurological effects of spaceflight, advancing our understanding of the molecular
239 mechanisms underlying the negative impact on the human brain caused by the space environment.

240 **Space environment activates retroelement transcription in mice**

241 To independently validate our main observations in a different model system, we analyzed publicly
242 available RNA-seq data from the retinas of mice exposed to spaceflight[10]. Although there was no overall
243 significant change in global gene expression between the ISS samples and ground controls **(Fig. 3A-**
244 **C)**, gene set enrichment analysis (GSEA) revealed enrichment of genes associated with
245 retrotransposon silencing, transposition, IL6-type cytokine receptor interaction, inflammasome
246 activation, and phagocytosis in the ISS samples. In addition, mitochondrial dysfunction in ISS was
247 suggested by downregulation of the aerobic electron transport chain and mitochondrial biogenesis, and
248 by upregulation of cytochrome c release **(Fig. 3D, bottom panel)**, corroborating our previous
249 mitochondrial findings in the human model. Based on these observations, we inferred that
250 retrotransposons are upregulated in the mouse retina during spaceflight. Supporting this, we found an
251 increased expression of class I retrotransposable elements: LINE, SINE, and LTR **(Fig. S3A)**. Notably,
252 multiple L1 subfamilies were significantly upregulated in the ISS samples **(Fig. S3B)**. Retrotransposable
253 elements are also upregulated following exposure to simulated 5-ion galactic cosmic radiation (GCR),
254 which models the effect of cosmic rays **(Fig. S3C-D)**. Furthermore, both evolutionary young and ancient
255 L1 subfamilies have been previously shown to be upregulated in the mouse lung under combined GCR
256 and microgravity exposure[11]. Together, these findings suggest that environmental factors specific to
257 space, including microgravity and cosmic radiation, can trigger the activation of endogenous L1
258 retroelements in both mouse and human brains.

259 **MECP2-KO brain organoids exacerbate the viral pathway at the ISS**

260 In the absence of external viral infections and based on our previous results, we hypothesized that
261 activation of endogenous L1 retroelements led to the upregulation of the viral pathway observed upon
262 space exposure in human brain organoids. L1s can reverse-transcribe their RNA sequences and
263 accumulate in the cytoplasm of astrocytes, thereby triggering an inflammatory response [12,13]. To test
264 this hypothesis, we used brain organoids lacking functional MeCP2 (MECP2-KO[9]), a known L1
265 repressor[14-16]. Moreover, our transcriptomic results indicate alterations in MECP2-related gene
266 expression under spaceflight conditions (**Fig. 2H**). MECP2-KO and control brain organoids were
267 exposed to the space environment and subjected to bulk proteomics analysis (**Fig. 4A** and **Table S3**).
268 The Reactome analysis showed that the most upregulated proteins are related to cellular stress
269 responses, including viral pathways (**Fig. 4B** and **Fig. S4**). The viral pathway was highly enriched (-
270 $\log_{10}(p)$ = -9.975, ratio = 0.044328553), comprising 34 proteins **(Table S5)**. The viral pathway was
271 further increased in the absence of the MECP2 gene (**Fig. 4B** and **Fig. S4A**), confirming MeCP2's role
272 in silencing this pathway. We evaluate the bulk transcriptome of the same MeCP2-KO model brain

organoids in a subsequent flight (SpX30). The heatmap shows that the genes listed are overall more highly expressed in the MeCP2-KO ISS samples and show significantly lower expression in the healthy brain organoids samples (ISS control) **(Fig. 4C).** A functional analysis of the most highly upregulated genes reveals a pro-inflammatory and immune-active state in the MeCP2-KO ISS samples, corroborating the first spaceflight (SpX18). Genes related to *i)* inflammation: SELE (E-selectin), OSMR (oncostatin M Receptor); *ii)* immune activation: CCR7 (C-C motif chemokine receptor 7); *iii)* tissue stress and remodeling: TGFBI; and *iv)* neurological stress response: NPY (neuropeptide Y) are highlighted in the ISS condition. To reinforce our findings, we also compared, from the same flight, the ground MeCP2-KO brain organoids *vs.* ISS MeCP2-KO brain organoids using a bulk transcriptomics approach **(Fig. S4B)**. In this evaluation, we highlight the following findings: *i)* upregulation of excitatory and inhibitory circuits in the brain: upregulation of NPAS4 (neuronal PAS domain-containing protein 4) in the ISS samples strongly suggests that the combined stress of the MeCP2-deficient background and spaceflight triggers a state of significant neurological distress or aberrant neuronal activity. This highlights the brain's vulnerability in a system where a key epigenetic safeguard (MeCP2) is already absent; *ii)* activation of inflammatory and tissue remodeling: LRRC15 (leucine rich repeat containing 15) is implicated in tissue remodeling and its upregulation is a response to stress or injury and has been described with an essential role in response to viral infections, including as a key determinant of host's susceptibility/resistance to SARS-CoV-2[17], IL36B (interleukin 36 beta): a pro-inflammatory cytokine belonging to the IL-1 family, indicating an active inflammatory response, when compared to the ground samples.

Translating to Earth: accumulated L1 transcripts in astrocytes promote neurotoxicity

To translate the observations in space to Earth, we decided to conduct a series of groundwork studies in a clinically relevant human condition. A lack of functional MECP2 in the nervous system can cause Rett syndrome (RTT) and other neurodevelopmental conditions[19]. Accumulating L1-derived single-stranded DNA (ssDNA) in human astrocytes can trigger a neurotoxic inflammatory response in another neurodevelopmental disorder[12]. Using the MECP2-KO and control lines, we checked for L1 expression and found that endogenous L1 transcripts and L1-derived ssDNA are enriched in iPSC-derived astrocytes lacking MECP2 (**Fig. 5A, B** and **Fig. S5A**). Cytokines are important signaling molecules produced by glial cells and are responsible for cell maturation and inflammation during neurodevelopment[18]. We found several cytokines that were upregulated in astrocytes lacking MECP2 (**Fig. S5B**), including an increase in secreted IL6 (**Fig. 5C** and **Figs. S5C-E**). High levels of secreted astrocytic IL6 have recently been implicated in RTT, affecting synaptogenesis in a mouse model [21]. We validated these observations in our human system, using astrocyte-conditioned media (ACM) and by adding recombinant human IL6 (rhIL-6) to the culture media of iPSC-derived control neurons at the same concentration found in MECP2-KO astrocytes (2 ng/mL) for two weeks (**Fig. 5D** and **Figs. S5F, G**). Moreover, we also found a two-fold increase in the expression of the IL6 family cytokine receptor's signal transducer, gp130 receptor (IL6ST) in postmortem cortical RTT samples compared with age-matched control samples **(Fig. S5E)**. More importantly, postmortem cortical tissues showed a fivefold increase in MECP2-KO IL6 protein levels compared with controls, consistent with the in vitro observat*ions* **(Fig. S5C)**. We observed a significant decrease in levels of synapsin1 puncta in control iPSC-derived neurons exposed to MECP2-KO ACM (**Fig. 5D**). These alterations were associated with functional synaptic defects in neurons exposed to conditioned media from MECP2-KO astrocytes. We also observed a significant reduction in synapsin1 puncta and total dendritic length in neurons when rhIL-6 was added to the medium (**Figs. S5F-G**). Moreover, control neurons treated with rhIL-6 that matured in multi-electrode array (MEA) plates decreased their spontaneous activity (**Fig. S5H**). Finally, we co-cultured independently generated human neurons and astrocytes. MECP2-KO astrocytes negatively affected the dendritic morphology of control neurons, reducing total dendritic length, the number of segments per neuron, and the spine density (**Figs. S5I-L).**

L1 inhibition rescues MECP2-KO astrocytes defects

To confirm that the deleterious effect of MECP2-KO astrocytes is due to the accumulation of L1 elements, we treated our cultures with FDA-approved antiretroviral reverse transcriptase (RTi) drugs Lamivudine (3TC) and Stavudine (d4T), known to inhibit L1 reverse transcription[40]. We additionally used

325 another antiretroviral drug, Nevirapine (NVP), as a negative control since no effect on L1 reverse
326 transcription has been previously shown[40,41]. When MECP2-KO astrocytes were chronically treated with
327 RTi, cytoplasmic L1 copies, and IL6 expression decreased to control levels (**Figs. 5B-C**). Similarly, we
328 observed reductions in other pro-inflammatory cytokines and related factors, including CXCL10
329 (interferon-gamma-induced protein 10), CCL2 (monocyte chemoattractant protein 1), and TMEM173
330 (stimulator of interferon genes) (**Figs. S5M-O**). Previous studies have reported elevated levels of the
331 excitatory neurotransmitter glutamate in the cerebrospinal fluid of patients with MECP2 mutations [22,24].
332 MeCP2 has been shown to modulate glutamate clearance by regulating various astroglial genes[23].
333 Indeed, we found that several genes related to glutamate metabolism were misregulated in MECP2-
334 KO astrocytes (**Fig. S5P**). MECP2-KO astrocytes treated with RTi restored glutamate, reactive oxygen
335 species (ROS), and glutathione levels to control cells (**Figs. 5E-G**).

336 **L1 inhibition rescues MECP2-KO neuronal defects in mixed cultures**

337 We also tested if RTi could restore neuronal function in mixed brain organoid cultures containing
338 MECP2-KO neurons and astrocytes. Treating MECP2-KO-derived cultures with RTi, rescued neuronal
339 cell body area and dendritic complexity (**Figs. 5H-I** and **Figs. S5Q-S**). To determine if the control of L1
340 activity by RTi can ameliorate synapse formation in MECP2-KO neurons, co-localization of SYN1
341 (synapsin I) and PSD95 (postsynaptic density protein 95) on a MAP2 (microtubule-associated protein
342 2) positive neurite was quantified. MECP2-KO neurons in the RTi-treated culture displayed a significant
343 increase in co-localized puncta compared to those without RTi-treatment, which is not seen in the NVP-
344 treated culture (**Fig. 5J**). At the functional level, neuronal network activity measured by the number of
345 bursts and firing rate in MECP2-KO-derived organoids was also rescued in cultures treated with RTi
346 (**Figs. 5K-L**).

347 **L1 reverse transcriptase inhibition rescued survival and behavior in a Mecp2-KO mouse model**

348 Hemizygous Mecp2-KO males have a median lifespan of approximately 10 weeks and exhibit
349 pronounced behavioral and physiological abnormalities [25,29,30,42]. We treated these animals with 3TC or
350 d4T in the drinking water (physiological dose of 2 mg/ml[26] starting at 4 weeks old. Both 3TC and d4T
351 ameliorated the overall aspect of the Mecp2-KO animals and extended their lifespan (**Fig. 6A-B**). Next,
352 we tested whether any behavior would be rescued following the animals' extended lifespan. The open-
353 field test revealed that 3TC treatment improves the mobility of Mecp2-KO mice (**Figs. 6C-D** and **Fig.**
354 **S6A**). Previous studies have demonstrated that this Mecp2-KO mouse model exhibits decreased
355 anxiety behavior [27]. We found no effect of 3TC treatment on the anxiety-related behavior of Mecp2-KO
356 mice (**Fig. 6E** and **Fig. S6B, Supp. Videos 1-3**). There are conflicting results regarding the sociability
357 of these rodent models [31,33]. In our hands, Mecp2-KO mice have impaired social memory, and this
358 phenotype can be rescued with 3TC treatment (**Fig. 6F**). Following behavioral analysis, the animals'
359 brains were fixed and subjected to Golgi staining for morphological analysis. We focus on the prefrontal
360 cortex, as this region is critical for social behavior. We found that the 3TC treatment rescued neuronal
361 soma size and spine density of Mecp2-KO neurons in the cingulate cortex (**Fig. 6G-H** and **Fig. S6C-**
362 **D**).

363 **L1 reverse transcriptase inhibition recovered abnormal gene expression in both astrocytes and**
364 **neurons in the brains of Mecp2-KO mice**

365 Given that behavioral impairments and aberrant neuronal morphologies in Mecp2-KO mice were
366 restored by 3TC treatment, we next examined whether these restorations are also detected at the
367 molecular level. To this end, we conducted spatial transcriptomics analysis (Xenium, 5k) on forebrain
368 sections from 8–9-week-old WT, Mecp2-KO, and Mecp2-KO mice treated with 3TC. We applied
369 unsupervised clustering on the combined dataset of 270,741 cells that passed quality control to define
370 cell clusters. We identified 10 unique clusters and annotated each cluster (excitatory neurons, inhibitory
371 neurons, astrocytes, oligodendrocyte progenitor cells (OPC), oligodendrocytes, microglia, endothelial
372 cells, pericytes, fibroblasts, smooth muscle cells) with the expression profiles of canonical cell type
373 marker genes and spatial information **(Fig. 7A-C).** Since we have demonstrated that astrocytes play
374 critical roles in neuronal morphology and function **(Figs. 5 and S5)**, we focused on astrocytes and

375 reanalyzed the astrocyte cluster using a different clustering method. We found that the cell number and
376 spatial distribution of each astrocyte subcluster in the forebrain were not substantially altered in Mecp2-
377 KO compared to WT **(Figure 7D-E)**. However, a comparison of gene expression across the entire
378 astrocyte cluster between WT and Mecp2-KO identified 173 genes as significantly up-regulated and
379 173 as significantly down-regulated under Mecp2-KO conditions **(Table S6)**. Gene ontology (GO)
380 analysis of the upregulated genes revealed enrichment of terms related to oxidative stress and
381 interleukin signal **(Fig. 7F)**. Intriguingly, significant overlap was observed between the genes
382 upregulated in these Mecp2-KO astrocytes and the 30 genes included in the gene list (5006 genes) in
383 the Xenium panel of 150 genes **(Table S4)** that were upregulated under ISS conditions **(Fig. 7G).**
384 Among the 4 overlapping genes, ALDOA (aldolase A), an enzyme involved in cellular metabolism and
385 previously implicated in inflammation [32] and DNA damage responses [43], was significantly
386 downregulated in Mecp2-KO mouse brains following 3TC treatment. Furthermore, we found that 3TC
387 treatment restored the impaired expression of inflammation-related genes implicated in these GO terms
388 **(Fig. 7H)**. In addition, consistent with these transcriptomic findings, immunostaining results showed that
389 complement component 3 (C3), a key immune marker associated with reactive astrocytes, was
390 upregulated in Mecp2-KO astrocytes and reduced by 3TC treatment **(Fig. 7I-J)**.

391 Based on the recovery of gene expression in astrocytes, we next compared gene expression in clusters
392 of excitatory neurons in WT, Mecp2-KO, and Mecp2-KO mice treated with 3TC and performed GO
393 analysis. We found that downregulated genes in Mecp2-KO relative to WT were enriched for GO terms
394 associated with synaptic signaling **(Fig. S7A)**. In addition, genes upregulated with 3TC treatment in
395 Mecp2-KO mice were enriched in similar GO categories **(Fig. S7B)**. Moreover, when we examined
396 genes in a specific GO term (synaptic signaling), expression of those genes was reduced in Mecp2-KO
397 but recovered with 3TC treatment **(Fig. S7C)**, suggesting that 3TC treatment recovered impaired gene
398 expression not only in astrocytes but also in neurons.

399

400 **DISCUSSION**

401 The modern cell has evolved to coexist with autonomous L1 sequences by activating defense
402 mechanisms within the cell's intrinsic immune system [44]. Moreover, DNA hypermethylation responses
403 were significantly pronounced in evolutionarily younger retrotransposons, suggesting that recent
404 genomic insertions might be particularly sensitive indicators of space exposure[11]. By employing a multi-
405 omics approach that integrates proteomics, bulk transcriptomics, and single-nucleus transcriptomics,
406 we provided a comprehensive view of the molecular alterations that affect human brain cells across
407 space. This led us to reveal a complex interplay between viral pathways, astrocyte reactivity, and
408 inflammatory responses, a novel phenomenon that we call Space-Induced Neural Senescence (SINS).

409 Multiple studies on neurological and psychiatric disorders have revealed increased L1 expression in
410 the brain [39]. We previously reported that the accumulation of L1-derived ssDNA in human iPSC-derived
411 astrocytes triggered pathological inflammation in a severe progeroid neurological condition, Aicardi-
412 Goutieres Syndrome (AGS) [12]. There is substantial evidence that transposable elements, particularly
413 L1 retrotransposons, are aberrantly reactivated in the aging brain and across various
414 neurodegenerative diseases, including Amyotrophic Lateral Sclerosis (ALS), Alzheimer's Disease (AD),
415 Parkinson's Disease (PD), and Huntington's Disease[45-49]. Our findings demonstrated that the histone
416 proteins and deacetylation processes are altered by the space environment, likely contributing to an
417 "epigenetic rewiring" and the activation of viral pathways in space. Histone downregulation is frequently
418 observed under conditions of cellular stress or in disease states, indicating alterations in chromatin
419 dynamics that affect the accessibility and stability of genomic DNA [50]. Reduced histone expression
420 impairs nucleosome assembly, leading to chromatin relaxation and aberrant activation of otherwise
421 silenced genomic regions, such as transposable elements[51]. This chromatin disruption often results in
422 compromised epigenetic regulation, enabling the transcriptional activation of repetitive sequences,
423 including L1s. Histone depletion thus facilitates L1 mobilization, reflecting a critical link between

chromatin remodeling and potential genome instability[52]. The activation of L1s following histone downregulation has profound biological implications, particularly in the context of aging and neurodegeneration. Aberrant L1 activation is closely associated with age-related neurodegenerative diseases such as Alzheimer's disease, where increased retrotransposition events correlate with neuronal loss and cognitive decline[53]. It is interesting to note that our re-analyses of the blood transcriptomic data from the NASA Twins Project [54] have also revealed an increase in viral molecular pathways, suggesting that the reactivation of endogenous retroviruses is likely not specific to brain tissue. However, due to the brain's limited regenerative capacity, the impact of this phenomenon is expected to be more pronounced. Our findings are in agreement with the space medicine literature[7,55-57] that dysregulation in OxPHOS proteins corroborates the idea that mitochondrial impairment is a shared pathological mechanism underlying diverse neurodegenerative processes, including Parkinson's disease (PD), Huntington's, and Alzheimer's diseases[58,59]. Also, corroborated with the genomic findings from the Inspiration4 mission, which also evaluated the OxPHOS genomic framework, revealing a sustained downregulation of PD-associated OxPHOS genes in astronauts' peripheral blood mononuclear cells (PBMCs)[60,61].

We and others have previously revealed that brain tissue isolated from RTT patients is more susceptible to L1 expression[14,16]. Here, we found that the accumulation of L1 transcripts in the absence of MeCP2 induces IL6 release by astrocytes. Several groups have previously reported interleukin abnormalities and cytokine release in RTT [18,21,62,63]. However, in the absence of a stimulating agent, this observation was not linked to a potential disease contribution. Activation of transposable elements exacerbates aging and neurodegeneration [45,64,65], promoting genomic instability, neuroinflammation, and aberrant immune signaling, as observed in our experiments in LEO. Moreover, recent studies have revealed a significant upregulation of transposable elements, including L1s, in excitatory neurons and astrocytes in AD brains[66,67], demonstrating that an increase in TE expression in AD is related to immune activation, synaptic dysfunction, and cellular senescence, similar to the findings associated to the SINS phenomenon, described in this study.

Thus, we hypothesized that the cytokine abnormalities in RTT are not a direct consequence of MECP2 mutations, but rather a pathological condition exacerbated by the accumulation of cytoplasmic L1 copies in astrocytes, which triggers the IL6-mediated neurotoxic response. Our findings linked L1 expression in RTT astrocytes to disease phenotypes, thereby enabling us to test whether L1 inhibition by RTi could reduce inflammation and mitigate neurotoxicity. The analyses from independent spaceflights corroborate that, in LEO, brain organoids activate sterile-mediated cellular responses, resulting in the activation of an immune response and epigenetic derangement that can activate viral pathways, inducing SINS, and immune dysfunction, offering a new framework for understanding how "dormant" genomic elements become pathogenic under certain conditions. Notably, increased levels of IL6 are also associated with neuropsychiatric conditions such as depression, Alzheimer's Disease, and aging [68,69]. Thus, we compared *in vitro* and *in vivo* non-treated and RTi-treated models in MECP2-KO brain organoids and Mecp2-KO mice, respectively. Our findings are summarized in **Fig. 8**. *In vitro*, the loss of MeCP2 results in increased transcription of L1 elements, leading to elevated inflammation, characterized by increased levels of IL6, ROS, glutamate, and inflammatory markers such as CXCL10, CCL2, and TMEM173. The molecular findings in the secretome panel and mitochondrial framework analysis indicate that these signatures are consistent with known space-environment stressors, including activation of the viral pathway, leading to oxidative stress and impairment of mitochondrial homeostasis. Importantly, they also align with recent literature describing spaceflight-induced activation of retrotransposons in mice [10] and the cellular senescence pathway in hematopoietic stem cells [70-72]. These findings collectively suggest a potentially space-environment-sensitive state, characterized by shifts in differentiation toward an inflammatory and viral-responsive pattern of transcription and translation.

MECP2-KO brain organoids treated with RTi restore neuronal function, promoting astrocytic homeostasis and indicating a significant recovery in cellular and synaptic function. *In vivo*, untreated

474 Mecp2-KO mice exhibited severe neurological deficits, including reduced survival, sociability, mobility,
475 and speed. When Mecp2-KO mice were subjected to RTi treatment, we observed improved
476 neurological symptoms and increased survival, as well as increased sociability, mobility, and speed,
477 compared with untreated controls. Furthermore, we confirmed these therapeutic effects also at the
478 molecular level. We demonstrated that RTi treatment suppresses cytokine responses and reduces
479 inflammatory markers typically associated with senescent cells and aged mice. These effects
480 underscore a causal link between retroelement activation and space-related inflammation, as observed
481 in our experiments on the ISS during independent spaceflights.

482 Radiation and microgravity stressors do not act in isolation but rather appear to have additive or even
483 synergistic effects on brain function. Since we cannot isolate the various factors acting at the ISS, we
484 refer to the combined effects of cosmic radiation, microgravity, and other unmeasured factors as the
485 "space environment". Due to its nature, space radiation - especially GCR (galactic cosmic radiation) -
486 plays a crucial role in biological systems. Rodents subjected to a complex 33-beam GCR simulation
487 exhibited deficits in attentional processing, along with disrupted dopaminergic neurotransmission in the
488 prefrontal cortex, despite maintaining reward-related behaviors [73], illustrating that cosmic radiation
489 inflicts structural and functional damage on neural circuits. In this study, the radiation measured in all
490 experiments at ISS, specifically the GCR dose recorded, averaged 0.119 mGy/day (absorbed dose)
491 and 0.126 mGy/day (dose equivalent). In contrast, the South Atlantic Anomaly (SAA) doses were about
492 0.084 mGy/day (absorbed dose) and 0.086 mGy/day (dose equivalent). Given these values, the
493 recorded doses from our spaceflights fall within the lower end of the expected radiation exposure range
494 for ISS missions. For shorter missions, such as typical CRS resupply flights, the biological impact is
495 likely negligible, as the total absorbed dose remains low and below critical thresholds that can trigger
496 acute health effects. Moreover, we have previously investigated the role of radiation in brain organoids
497 submitted to proton radiation (0.5 and 2 Gy)[74]. We found dose- and time-dependent increases in DNA
498 damage, oxidative stress, and activation of DNA damage checkpoint genes, particularly at 48 hours
499 post-irradiation. Other significant findings included declines in mitochondrial function and neural identity,
500 corroborating the results of this study; however, we acknowledge the limitations of attributing the
501 phenotypic findings solely to this stressor.

502 The collective findings on the secretome panel suggest that the space environment may be triggering
503 a "recalibration" of the brain organoids' developmental program, causing these models to strengthen
504 their cellular defenses to address the unique challenges of space. This may serve as a mechanism to
505 achieve a more resilient, faster-differentiated state, leading to a SINS state. The combined findings of
506 the three spaceflights validate the results described in this study, demonstrating that the space
507 environment leads to biological alterations in the brain organoids model, resulting in a phenotype that
508 displays profound cellular stress, impaired genome regulation, and inflammation, potentially mediated
509 by cGAS/STING pathway, a mechanism previously described by our group[12], and which is activated by
510 presence of viral DNA[75] and retroelements[75,76], especially in neurodegenerative diseases[77,78]. It is well
511 established in the literature that transposable element activation is not merely a bystander effect in
512 aging and senescence but a potentially causal mechanism in disease progression, contributing to cell-
513 to-cell variability and neuronal vulnerability [79,80].

514 The successful preclinical data highlight RTi's immediate utility in therapeutic regimens for RTT and
515 other neuroinflammatory disorders, revealing a potential novel neuroprotective treatment for astronauts
516 on long spaceflight missions as a translational venue. The proven safety and tolerability profile of 3TC
517 makes it an attractive candidate for drug repurposing strategies aimed at preventive treatment in
518 astronauts, particularly given the altered immune function and potential viral reactivation that can occur
519 during extended space missions [81,82]. Prophylactic and therapeutic administration of 3TC drugs could
520 theoretically mitigate latent retroviral or endogenous retroviral elements whose activation may be
521 potentiated by the stress-induced immunosuppression associated with spaceflight[83], and its known
522 efficacy against viral replication during spaceflight has already been documented in the literature[84]. The
523 broad anti-inflammatory and immunomodulatory effects of RTis, particularly their capacity to mitigate

inflammation driven by endogenous retroviruses, offer a novel and powerful mechanism to counter the pervasive immune dysregulation observed in microgravity.

Our study's findings align with recent astronaut [60,85] and mouse [20] data on the space environment, underscoring the critical need for a comprehensive approach to protecting astronaut health during long-duration space missions. This could include implementing antiviral and anti-inflammatory strategies to ensure the well-being of future generations of explorers.

LIMITATIONS OF THE STUDY

Limitations of the study are attributable to inherent difficulties in the space environment and in LEO. The experiments are extremely precious and constrained by the payload capacity of each spaceflight, making it difficult and costly to send multiple biological replicates on a single flight.

RESOURCE AVAILABILITY

Lead Contact

Requests for further information and resources should be directed to and will be fulfilled by the lead contact, Dr. Alysson R. Muotri (muotri@ucsd.edu).

Materials Availability

This study did not generate new unique reagents or materials

Data and code availability

- The mass spectrometry proteomics data have been deposited to the ProteomeXchange Consortium via the PRIDE (https://www.ebi.ac.uk/pride/) partner repository with the dataset identifier PXD055001 and also in the NASA GeneLab repository, https://osdr.nasa.gov/bio/submission/rdsa/RDSA-939 and are publicly available as of the date of publication.

- The transcriptomics data is deposit in the NASA GeneLab repository under the study number OSD-765 and also in the Zendo (10.5281/zenodo.16388786 and 10.5281/zenodo.16389553) and are publicly available as of the date of publication.

- This paper does not report original code.

- Any additional information required to reanalyze the data reported in this paper is available from the lead contact upon request.

ACKNOWLEDGMENTS

We would like to thank the invaluable efforts of the ISSCOR team: Natalia Chermont, Isabelle Luz, Paulo Carvalho, Juliana Fisher, and Blake Tsu. Roberto Herai, Luiz Pedro Petroski, and Adriano Ferrasa for all the insights on RNAseq data. We acknowledge the invaluable efforts of Space Tango, our implementation partner, in providing telemetric data from all missions. We acknowledge the Space

Radiation Analysis Group (SRAG) for providing the radiation data used in this work. We acknowledge Daniel McClatchy and Claire Delahunty from Yates's lab for their experimental advice, Richard Waite, Narayanaganesh "Ganesh" Balasubramanian, Leslie Sandoval, Michael Krawitzky, and Matt Willetts from Bruker for their support in this work. This work was supported by grants from the NSF/CASIS grant (CBET 2126309) and NASA (80JSC018M0005) to A.R.M.; AMED (JP20gm1310008, JP24wm0625306), JSPS KAKENHI (JP23H00391) and an Intramural Research Grant (3-9) for Neurological and Psychiatric Disorders of NCNP Grant to K.N.; JSPS KAKENHI (JP22K15201, JP23H04170, JP25H01866) and AMED (23gm1310008) to H.N. This research was also supported by NPO the Rett Syndrome Support Organization to H.N. (2019-2-10) and an NIH grant (#S10 OD026929) from Dr. K. Jepsen at the UCSD Institute of Genomic Medicine. A.R.M., H.N., and K.N. are inventors on a pending U.S. patent application for the use of reverse transcriptase inhibitors for Rett syndrome (U.S. Application No. US18/569,721).

AUTHOR CONTRIBUTIONS

Conceptualization, A.M., H.N., A.M., P.M., E.V., K.N., A.R.M.; Methodology, A.M., K.N., J.Y., A.M., P.M., A.R.M.; Investigation, A.M., H.N., A.M., T.U., S.M., P.M., L.L., L.C., E.V., N.S., A.S., A.S., B.F., A.L., D.A., M.I., J.Y.,T.O., M.H., K.N., A.R.M. Visualization, A.M., P.M., L.L., L.C., A.S., K.N., A.R.M. Funding acquisition, K.M., H.N., A.R.M.; Project administration, K.N., A.R.M.; Supervision, K.N., A.R.M. Writing – original draft, A.R.M.; Writing – review & editing, A.M., H.N., A.M., T.U., P.M., L.L., L.C., E.V., N.S., A.S., A.S., B.F., A.L., D.A., M.I., J.Y., K.N., A.R.M.

DECLARATION OF INTERESTS

The authors declare no competing interests.

SUPPLEMENTAL INFORMATION

Figures S1-S7, Tables S1-6, Supplementary Videos 1-3.

588 **FIGURE AND LEGENDS**

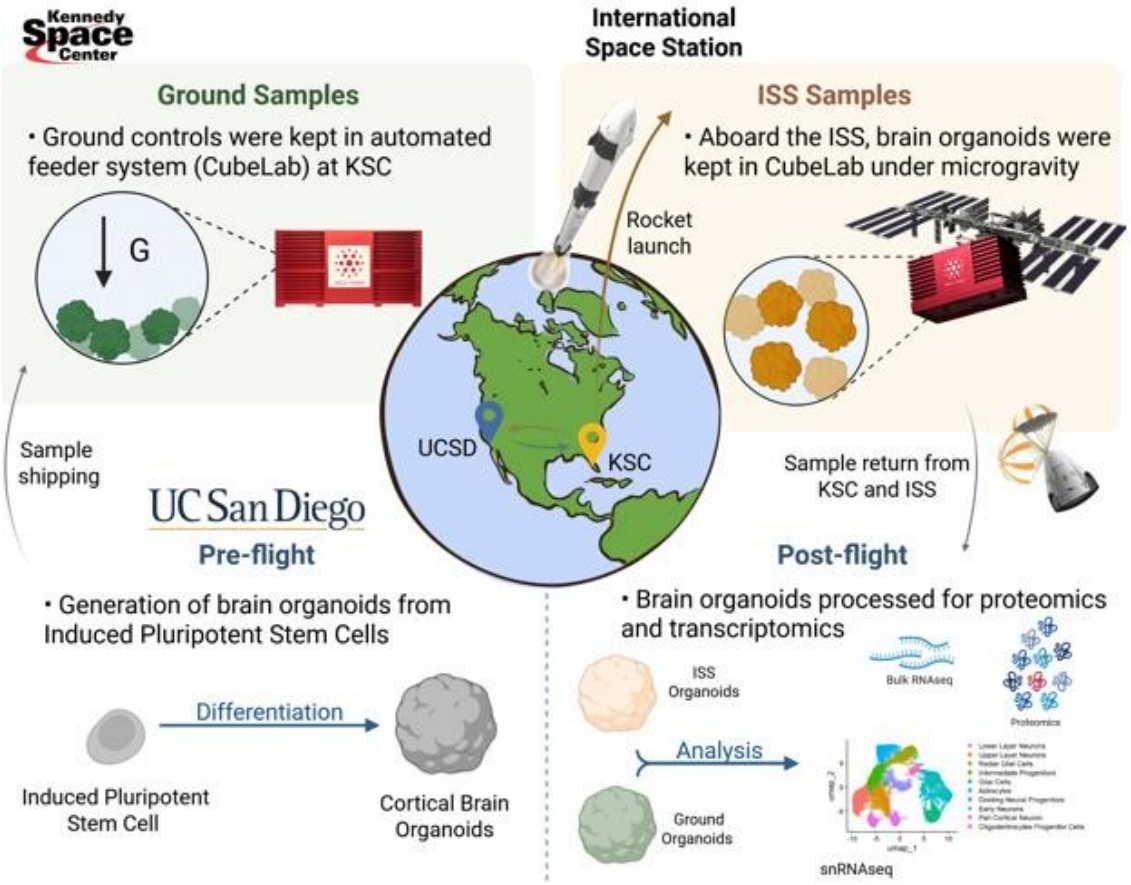

589
590 **Fig. 1. Schematic brain organoids experiments sent to the International Space Station (ISS).** This
591 schematic depicts the process and experimental setup for studying brain organoids under space
592 environment conditions aboard the International Space Station (ISS). Induced pluripotent stem cells
593 were differentiated into brain organoids. These brain organoids were launched on SpaceX CRS-SpX18,
594 CRS-SpX30; CRS-SpX31 missions (on average 30 days) and maintained aboard the ISS in an
595 automated system (CubeLab), exposed to the space environment. A synchronous ground control group
596 of brain organoids was maintained in parallel under identical conditions in another CubeLab to enable
597 comparative studies. Following their return from ISS, comprehensive molecular analyses, including
598 proteomic and transcriptomics assessments, were conducted on both ISS and Earth-bound brain
599 organoids to evaluate the impact of space environment conditions on molecular and cellular processes
600 and development.
601

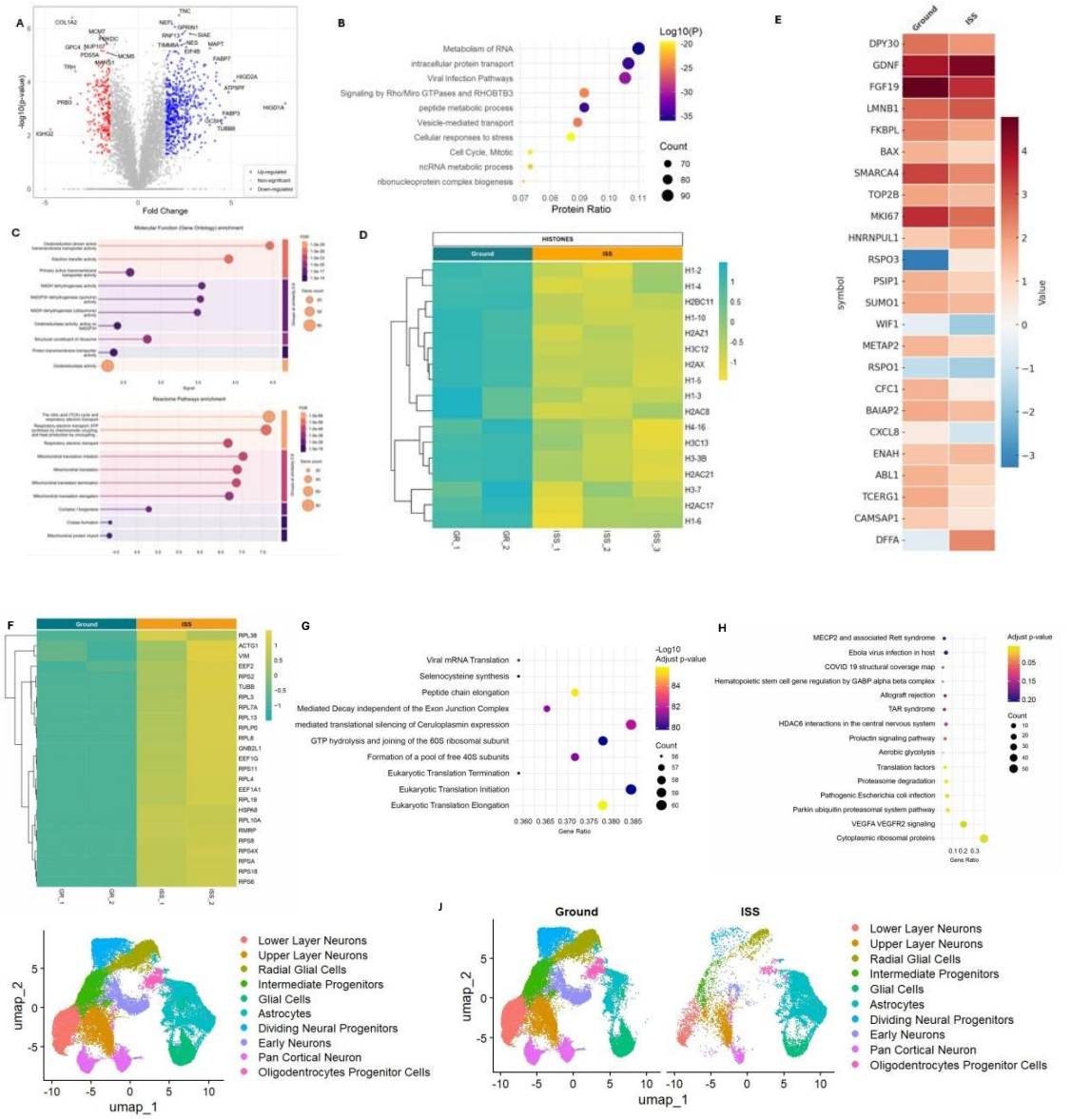
A
Fold Change
-log10(p-value)
B
Metabolism of RNA
intracellular protein transport
Viral Infection Pathways
Signaling by Rho/Miro GTPases and RHOBTB3
peptide metabolic process
Vesicle-mediated transport
Cellular responses to stress
Cell Cycle, Mitotic
ncRNA metabolic process
ribonucleoprotein complex biogenesis
Protein Ratio
Log10(P)
Count
C
D
HISTONES
Ground
ISS
E
Ground
ISS
symbol
Value
F
Ground
ISS
G
Viral mRNA Translation
Selenocysteine synthesis
Peptide chain elongation
Mediated Decay independent of the Exon Junction Complex
mediated translational silencing of Ceruloplasmin expression
GTP hydrolysis and joining of the 60S ribosomal subunit
Formation of a pool of free 40S subunits
Eukaryotic Translation Termination
Eukaryotic Translation Initiation
Eukaryotic Translation Elongation
-Log10 Adjust p-value
Count
Gene Ratio
H
MECP2 and associated Rett syndrome
Ebola virus infection in host
COVID 19 structural coverage map
Hematopoietic stem cell gene regulation by GABP alpha beta complex
Allograft rejection
TAR syndrome
HDAC6 interactions in the central nervous system
Prolactin signaling pathway
Aerobic glycolysis
Translation factors
Proteasome degradation
Pathogenic Escherichia coli infection
Parkin ubiquitin proteasomal system pathway
VEGFA VEGFR2 signaling
Cytoplasmic ribosomal proteins
Adjust p-value
Count
Gene Ratio
Lower Layer Neurons
Upper Layer Neurons
Radial Glial Cells
Intermediate Progenitors
Glial Cells
Astrocytes
Dividing Neural Progenitors
Early Neurons
Pan Cortical Neuron
Oligodentrocytes Progenitor Cells
umap_1
umap_2
J
Ground
ISS
K
Proportions by Condition
Oligodentrocytes Progenitor Cells
Early Neurons
Dividing Neural Progenitors
Intermediate Progenitors
Radial Glial Cells
Pan Cortical Neuron
Lower Layer Neurons
Glial Cells
Upper Layer Neurons
Astrocytes
Ground
ISS
Proportion
L
GFAP
TGFB2
Expression Level
Ground
ISS
M
condition
GROUND
ISS

Fig. 2. Proteomics and transcriptomics analysis data from healthy brain organoids at the International Space Station (ISS). (A) Volcano plot of proteomics data showing proteins upregulated (in blue) and downregulated (in red) in brain organoids at ISS, when compared to ground control. **(B)** Reactome pathway analysis of the proteins upregulated in the proteomics experiment. **(C)** Gene Ontology (GO) analysis for the mitochondria framework. 629 downregulated proteins are significantly enriched in functions and pathways crucial for cellular energy production (respiration) and the synthesis of mitochondrial proteins. **(D)** Heatmap of a framework of general downregulation in histone showing global chromatin remodeling. **(E)** Secretome panel on a subsequent flight (Spx31). The media of a batch of healthy brain organoids with 2 months at arrival were evaluated using Olink Reveal® panel technology (Thermo Fisher Scientific). Sample controls were used to determine precision within and between plates, triplicate negative controls samples set the limit of detection (LOD) and triplicate samples were used to standardize protein levels within a plate. Secretome sample run 1:1. Counts of known sequences were translated into Normalized Protein eXpression (NPX) values as their log-2 scaled quantification. **(F)** Heatmap of the top 25 Differentially Expressed Genes (DEGs) in ISS *vs.* ground conditions. The colors represent fold changes, with red indicating genes that are downregulated and blue indicating genes that are upregulated. **(G** Reactome pathway analysis of the upregulated genes from the transcriptomics experiment (Panel D). **(H)** WikiPathway enrichment analysis of the transcriptomic data (Panel D). **(I)** The UMAP plot shows the distribution of various neural cell types identified across both ground and ISS conditions. Each cluster is color-coded to represent a specific cell population: lower layer neurons (red), upper layer neurons (orange), radial glial cells (yellow-green), intermediate progenitors (green), glial cells (teal), astrocytes (cyan), dividing neural progenitors (light blue), early neurons (purple), pan cortical neuron (pink), and oligodendrocytes progenitor cells (magenta). The plot highlights the spatial organization of cell clusters, emphasizing the diversity of cell types within the dataset. **(J)** UMAP analysis comparing brain organoids samples from ground and ISS. **(K)** Stacked bar plots representing the relative proportions of different cell types in the ground and ISS. Each bar represents a specific cell type, with the dashed line indicating equal proportion mark. **(L)** *GFAP* and *TGFB2* expression in cells across ground and ISS conditions. Violin plots show the distribution of gene expression levels for GFAP and TGFB2 in cells from the ground and ISS environments. Each violin represents the kernel density estimation of log expression values, indicating higher levels of expression in the ISS condition compared to the ground condition. **(M)** Heatmap of healthy brain organoids, using bulk transcriptomics analysis, in a subsequent flight (SpX30). For proteomics analysis: $p \leq 0.01$; $fc \geq 1.2$. Test T Student for comparisons. For transcriptomics bulk analysis: $p \leq 0.05$; $fc \geq 1.2$. For pathway analysis: *Homo sapiens* as the reference organism, minimum overlap of 3 genes, enrichment factor > 1.5, and $p < 0.01$.

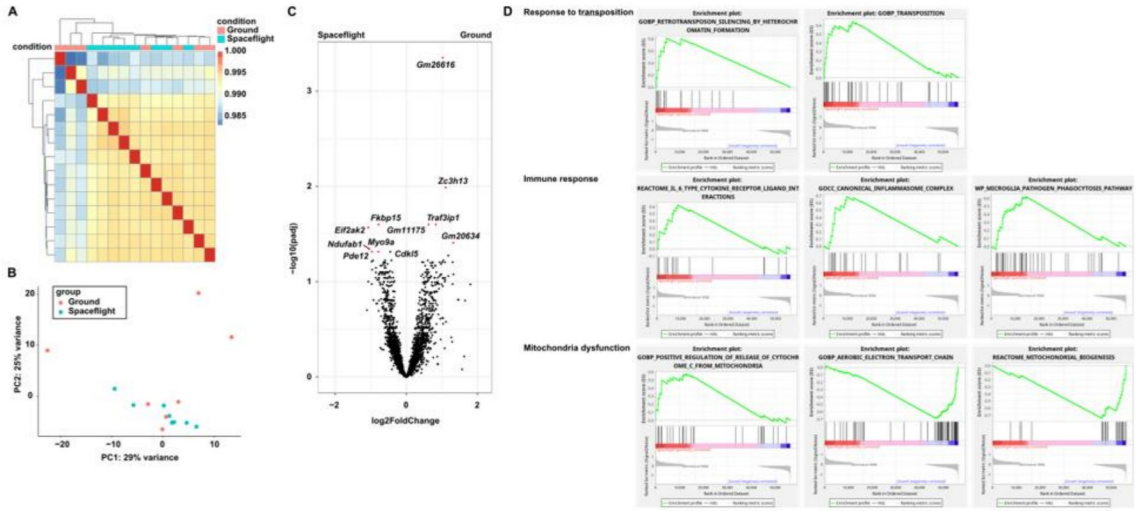

Fig. 3. Reanalysis of publicly available RNAseq data from ISS and ground control mouse retinas. (A) Heatmap of ISS and ground control retinas. **(B)** Principal coordinates analysis (PCoA) of ISS and ground control retinas**. (C)** Volcano plot of differentially expressed genes. **(D)** GSEA analysis of spaceflight and ground control retinas.

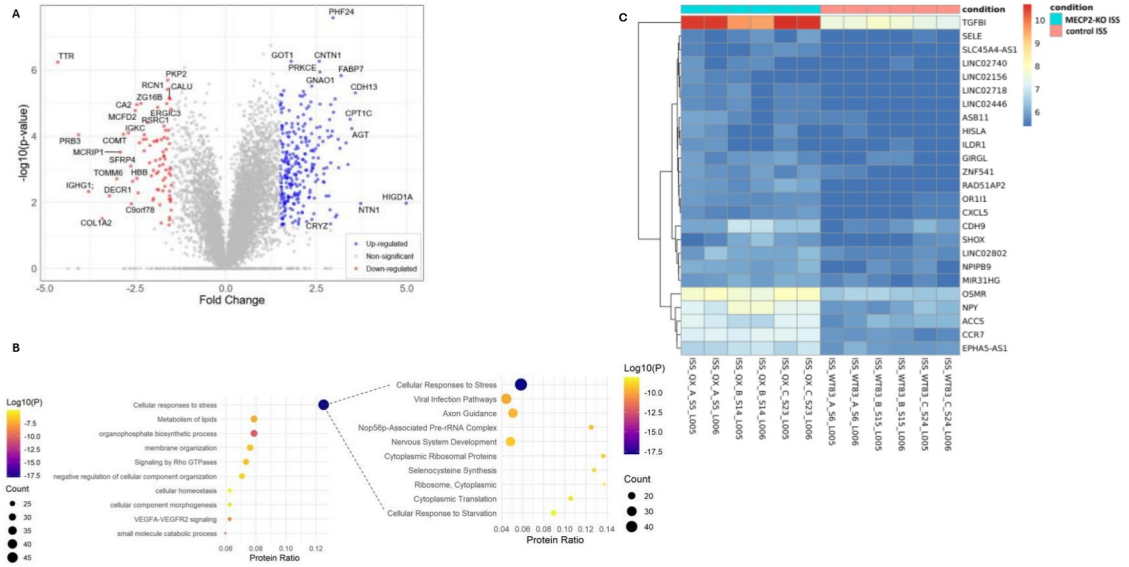

Fig. 4. Proteomics and transcriptomics analysis overview of MECP2-KO brain organoids at the International Space Station (ISS). (A) Volcano plot displaying proteins upregulated in MECP2-KO cortical brain organoids (in blue) and downregulated (in red), when compare to control brain organoids, both at ISS. **(B)** Reactome pathway analysis from proteins upregulated in MECP2-KO brain organoids at ISS. This panel includes an overall pathway visualization followed by a focusing on the "cellular response to stress" pathway, highlighting the viral pathway. **(C)** Heatmap from a subsequent spaceflight (SpX30) demonstrating a robust and consistent difference between the MECP2-KO brain organoids *vs.* healthy brain (control) organoids, both submitted to the space environment, at ISS. The hierarchical clustering indicates a distinct gene expression signature associated with the MeCP2-KO condition at ISS. Each experiment was done in biological duplicates. For proteomics bulk analysis: p≤0.01; fc≥1.2. Test T Student for comparisons. For pathway analysis: *Homo sapiens* as the reference organism, minimum overlap of 3 genes, enrichment factor > 1.5, and p < 0.01.

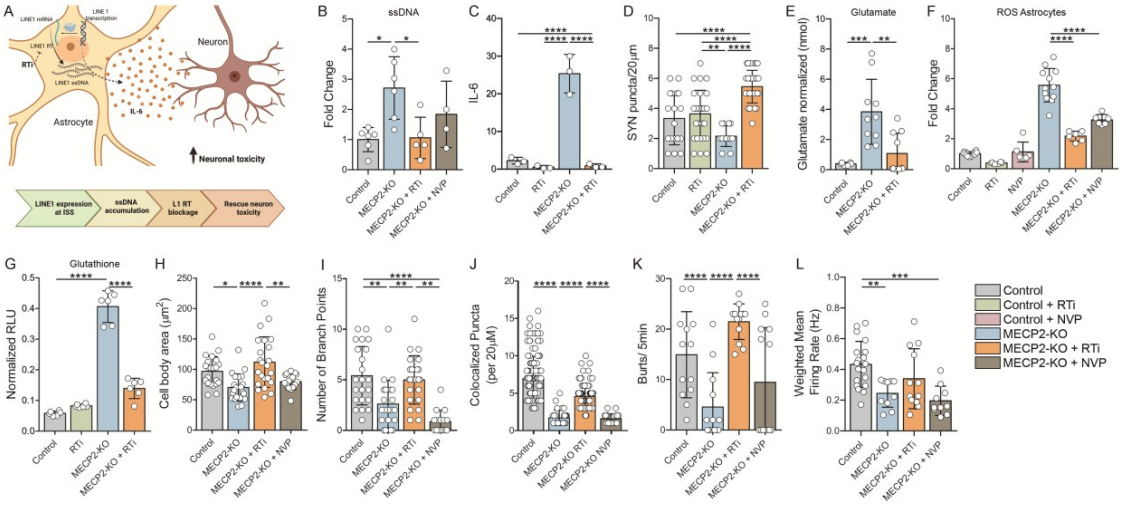

Fig. 5. L1 expression in MECP2-KO astrocytes causes neurotoxicity that can be rescued with reverse transcriptase inhibitors (RTi), but not nevirapine (NVP). (A) Schematic figure on how ssDNA accumulates in the astrocytes, leading to increased neurotoxicity in neurons. **(B)** Quantification of extrachromosomal L1-derived single-stranded DNA (ssDNA) on MECP2-KO astrocytes. **(C)** Quantification of released IL-6 from astrocytes by enzyme-linked immunosorbent assay (ELISA). **(D)** Quantification of synaptic puncta per 20 µm on control and MECP2-KO neurons treated with astrocyte conditioned media (ACM). **(E)** Quantification of glutamate buffering in MECP2-KO astrocytes. Data are represented as mean ±SEM. Levels are normalized to control equaling one. **(F)** Quantification of reactive oxygen species (ROS) levels in MECP2-KO astrocytes. Data are represented as mean ±SEM. Levels are normalized to control without treatment equaling one. **(G)** Quantification of intracellular glutathione in MECP2-KO astrocytes. Data are represented as mean ±SEM. Levels are normalized to control without treatment equaling one. **(H)** Quantification of neuronal cell body area. **(I)** Quantification of neuronal dendritic complexity by number of branch points. **(J)** Quantification of co-localized synaptic puncta (defined by SYN1+/PSD95+ on MAP2+ dendrite) per 20 µm on neurons from each condition. **(K)** Quantification of the total number of spikes of control neurons matured on MEA plates. **(L)** Quantification of weighted mean firing rate from organoids in each condition. Reverse-transcriptase inhibitor (RTi) or nevirapine (NVP) treatment is indicated. Each color represents one condition: control (black), MECP2-KO (blue), MECP2-KO+RTi (orange), and MECP2-KO+NVP (green). Each experiment was done in biological triplicates. The number of measurements (*n*) for these experiments is indicated directly by the symbols (o) on each bar graph. Data are represented as mean ±SEM. $p<0.5$ (*), $p<0.01$ (**), $p<0.001$ (***) and $p<0.0001$ (****); ordinary one-way ANOVA.

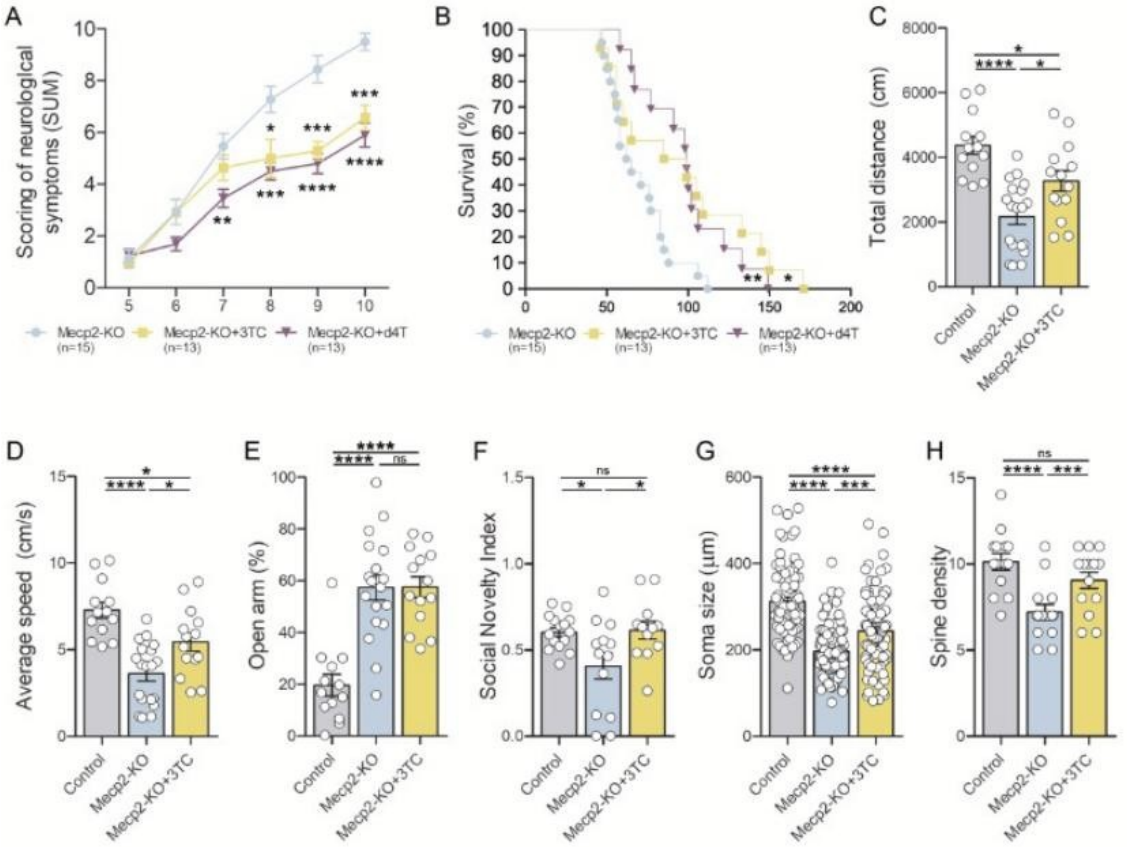

Fig. 6. Treatment of Mecp2-KO with reverse transcriptase inhibitors (RTis) in a mouse model. (A) Time plot of scores from a neurological symptoms assessment of Mecp2-KO mice with and without treatment of RTis lamivudine (3TC) and stavudine (d4T) at 2 mg/mL. The time plot of neurological symptoms scores depicts 5 weeks after RTi treatment was introduced in drinking water (weeks 5-10). **(B)** Time plot of percent survival depicts mice's lifespan in a number of days. **(C)** Quantification of total distance traveled and average speed of WT, Mecp2-KO, and 3TC-treated Mecp2-KO mice in the open-field test. **(D)** Quantification of average speed (cm/seconds) by WT, Mecp2-KO, and 3TC-treated Mecp2-KO mice in an open arm chamber during the elevated plus maze test. **(E)** Quantification of time spent (in percentage of total time) by WT, Mecp2-KO, and 3TC-treated Mecp2-KO mice in an open arm chamber during the elevated plus maze test. **(F)** Quantification of social novelty index of WT, Mecp2-KO, and 3TC-treated Mecp2-KO mice in a three-chamber test. Social novelty index is measured as time spent in the chamber with an intruder divided by the total time spent in both chambers. **(G)** Quantification of soma size and spine density. **(H)** Quantification of neurons from the cingulate cortex in brains fixed from WT, Mecp2-KO, and 3TC-treated Mecp2-KO mice. Spine density is measured by number of spines per 10 µm of dendrite. The number of measurements (*n*) for these experiments is indicated directly by the symbols (o) on each bar graph. Data are represented as mean ±SEM. $p<0.5$ (*), $p<0.01$ (**), $p<0.001$ (***) and $p<0.0001$ (****); ordinary one-way ANOVA.

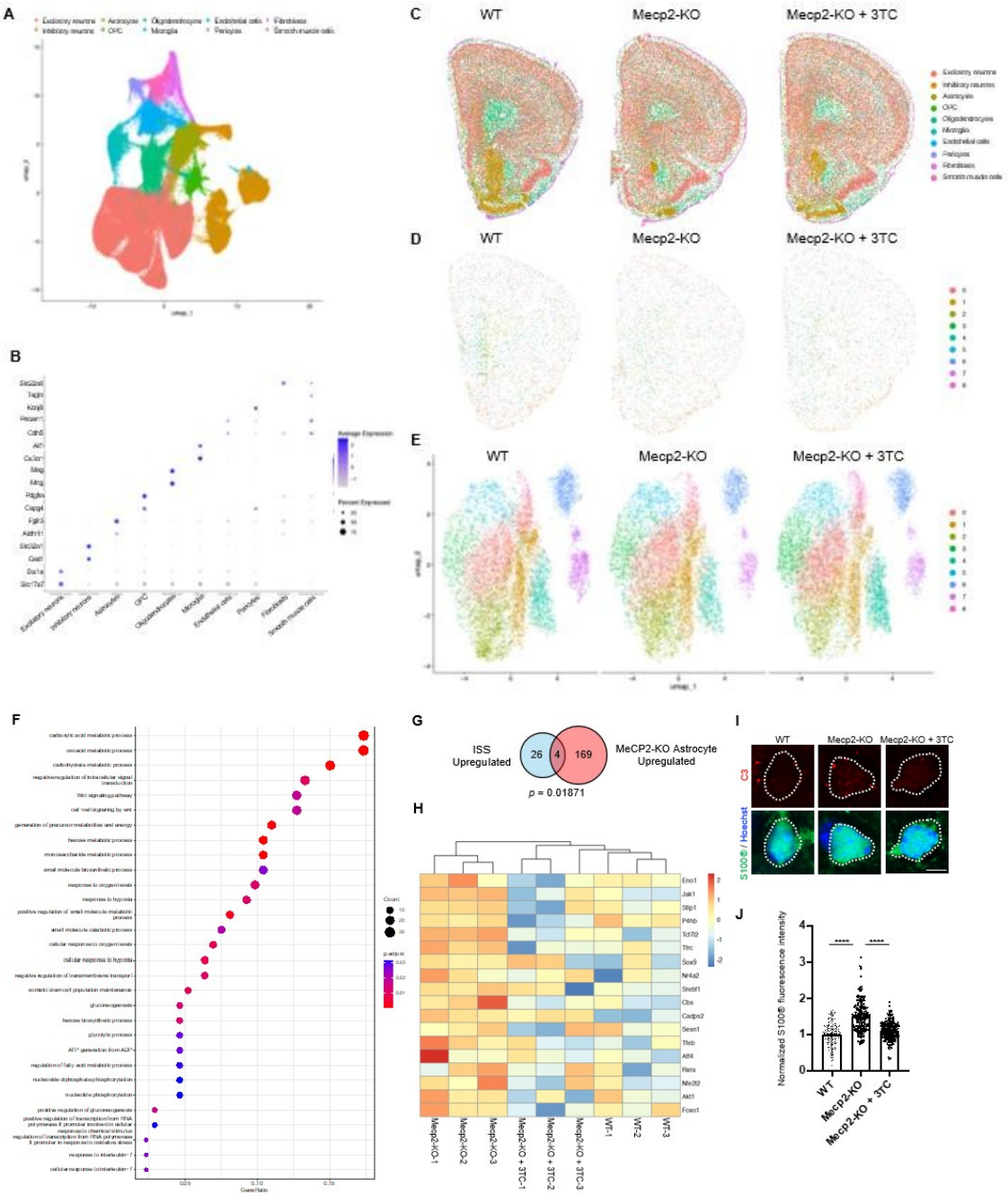

Fig. 7. Spatial transcriptomics analysis of WT, Mecp2-KO and 3TC-treated Mecp2-KO astrocytes. **(A)** UMAP plot showing 270741 cells annotated into 10 clusters from the brains, including PFC region, of WT (n=3), Mecp2-KO (n=3) and 3TC-treated Mecp2-KO (n=3) mice. **(B)** Scaled dot plot of canonical cell type marker genes used to define each cluster. **(C)** Spatial representative image plots of cell types in (A) across coronal hemisection of the WT, Mecp2-KO and 3TC-treated Mecp2-KO mice forebrains. **(D)** Spatial representative image plots of astrocyte subtypes in coronal hemisections of WT, Mecp2-KO and 3TC-treated Mecp2-KO mouse forebrains. **(E)** UMAP analysis comparing astrocyte subtypes across WT, Mecp2-KO and 3TC-treated Mecp2-KO mouse forebrains. **(F)** GO analysis of upregulated genes in Mecp2-KO astrocytes compared to WT astrocytes. (G) Overlap between ISS upregulated genes and Mecp2-KO astrocyte upregulated genes. **(H)** Heatmap of differentially expressed response to interleukin-7 (GO:0098760) and cellular response to external stimulus (GO:0071496) genes that were upregulated in Mecp2-ko astrocytes compared to WT astrocytes and downregulated in 3TC-

treated Mecp2-KO astrocytes. *(I)* Immunofluorescence staining for C3 (red) and S100β (green) in the PFC regions of 8-week-old WT, Mecp2-KO and 3TC-treated Mecp2-KO mouse brains. Nuclei are counterstained with Hoechst (blue). Scale bar, 5 µm. **(J)** Quantification of C3 signal intensity within the soma of S100β+ astrocytes. The number of individual measurements (n) for each experimental group is indicated by the symbols (o) on the bar graph. Data are presented as mean ± SEM. ****p<0.001 by ordinary one-way ANOVA.

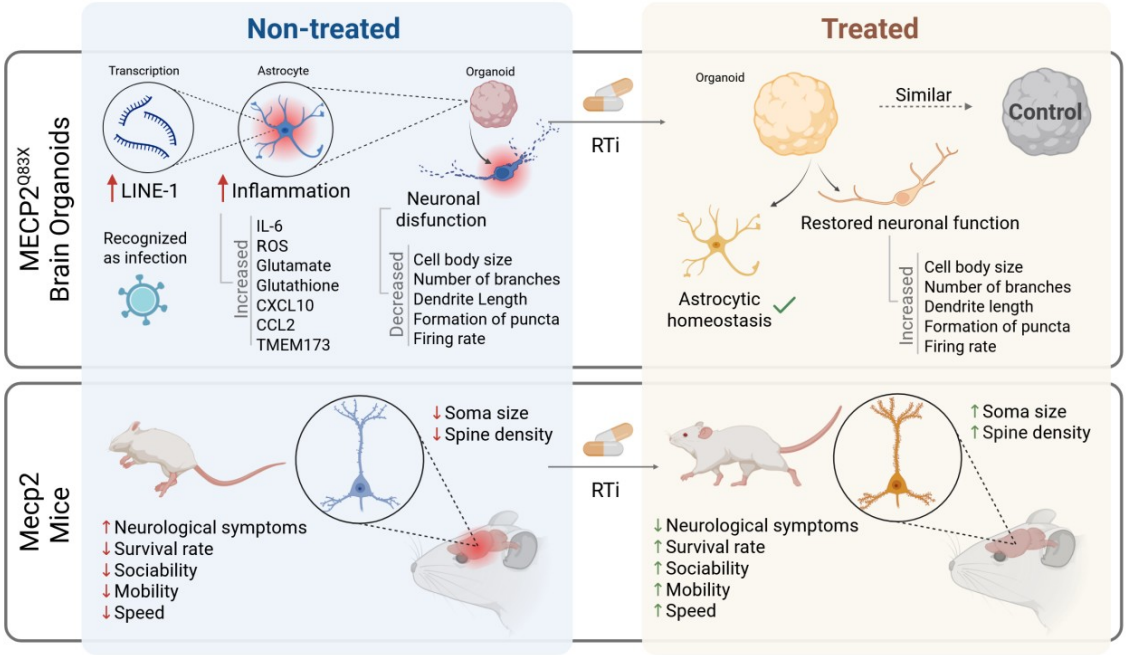

Fig. 8. Summary comparing non-treated and RTi-treated models in MECP2-KO brain organoids and Mecp2 mice. Top Panel: Brain Organoids (MeCP2-KO). The left side depicts non-treated MeCP2-KO brain organoids, where the loss of MeCP2 results in increased transcription of LINE-1 elements, which are recognized as infection triggers. This leads to elevated inflammation, characterized by increased levels of IL-6, ROS, glutamate, and inflammatory markers such as CXCL10, CCL2, and TMEM173. In parallel, neuronal dysfunction is observed, including reductions in cell body size, dendritic branching, dendrite length, the formation of synaptic puncta, and firing rates. The right side represents organoids treated with RTi (reverse transcriptase inhibitor). Treatment restores neuronal function and promotes astrocytic homeostasis. Neuronal characteristics, such as cell body size, number of dendritic branches, dendrite length, synaptic puncta formation, and firing rates, are restored to levels comparable to the control condition, indicating a significant recovery in cellular and synaptic function. **Bottom Panel: Mecp2-KO Mice.** The left side shows non-treated Mecp2 mice, where a decrease in soma size and spine density is observed, accompanied by severe neurological symptoms, including reduced survival rate, sociability, mobility, and speed. The right side illustrates the effects of RTi treatment in Mecp2 mice. Treatment leads to increased soma size and spine density, accompanied by improvements in neurological symptoms. Treated mice show enhanced survival rate, sociability, mobility, and speed compared to non-treated controls.

SUPPLEMENTAL FIGURE LEGENDS

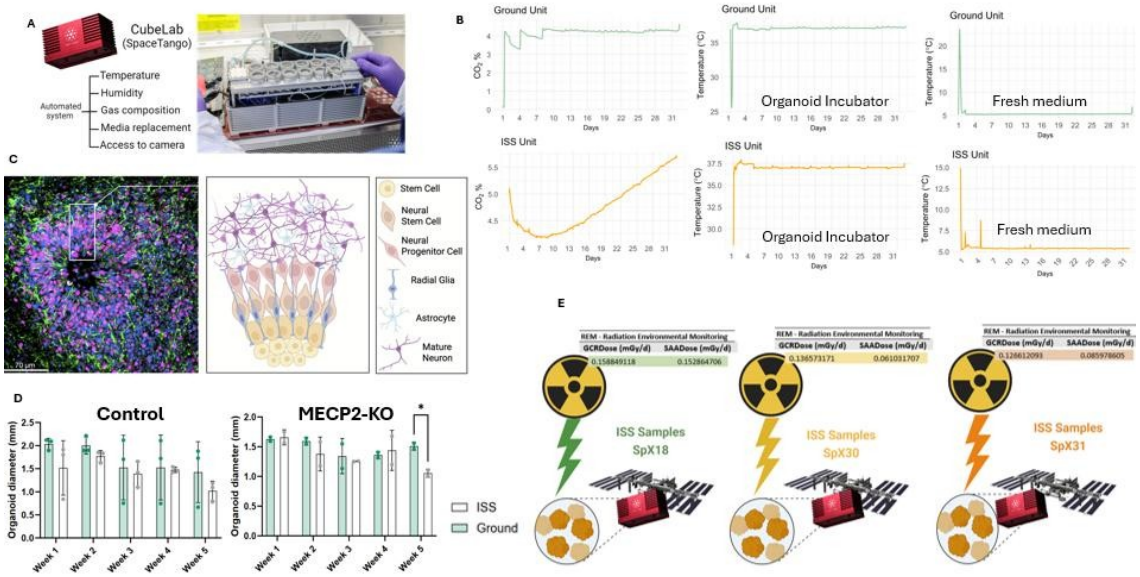

Fig. S1. CubeLab and environmental conditions and functionality. (A) Illustration representation of the CubeLab capabilities monitored during the space environment experiment on the International Space Station (ISS). The outer view and internal setup of the CubeLab, which houses the wells containing the organoids, are depicted, as well the organoids inside the well in the ISS. The CubeLab is designed to control temperature, humidity, and gas composition, automatically exchanging the cell medium. Additionally, the CubeLab is equipped with cameras that allow real-time observation of the organoids from Earth during spaceflight. **(B)** Environmental parameters monitored during the space environment experiment on the International Space Station (ISS) compared to ground control. The X-axis represents the days of the mission, while the Y-axis shows values for CO_2 concentration, organoid incubator temperature and fresh culture medium temperature, in both environments. The CO_2 concentration was maintained at around 5%; the organoid incubator temperature was kept around 37°C; and the fresh culture medium temperature at 4°C until it was used to feed the organoids every two days. Duplicate measurements were taken for each temperature to ensure accurate readings. **(C)** Schematic view of the brain organoid used in this work. On the left, a confocal image of a human cortical organoid stained for stem cell marker SOX2 and neural progenitor marker nestin. Cells are organized in radial units that resemble early cortical plate layering. Neural stem and progenitor cells (magenta nuclei) densely populate the rosette region. Neural progenitors (green) extend long basal processes outward, guiding the migration of newly generated neurons. DAPI (blue) marks all nuclei. Scale bar = 70 µm. On the right, a schematic representation of the cellular architecture observed in the organoid, depicting the spatial arrangement and lineage progression from undifferentiated stem cells to mature neurons and astrocytes. **(D)** Comparison of average organoid diameter over five weeks between the Ground and ISS units. The graphs show the diameters of organoids in control and MECP2-KO groups. **(E)** REM – Radiation environmental monitoring readings for the three spaceflights used in this work. Each point represents the mean diameter of multiple organoids within a single well ± standard error of the mean (SEM) for organoids cultured under each condition (ISS and Ground). A significant difference in organoid diameter is observed in the MECP2-KO group at week 5 between the microgravity (ISS) and Earth gravity (Ground) conditions, suggesting an impact of microgravity on MECP2-KO organoid growth. *$p \leq 0.05$.

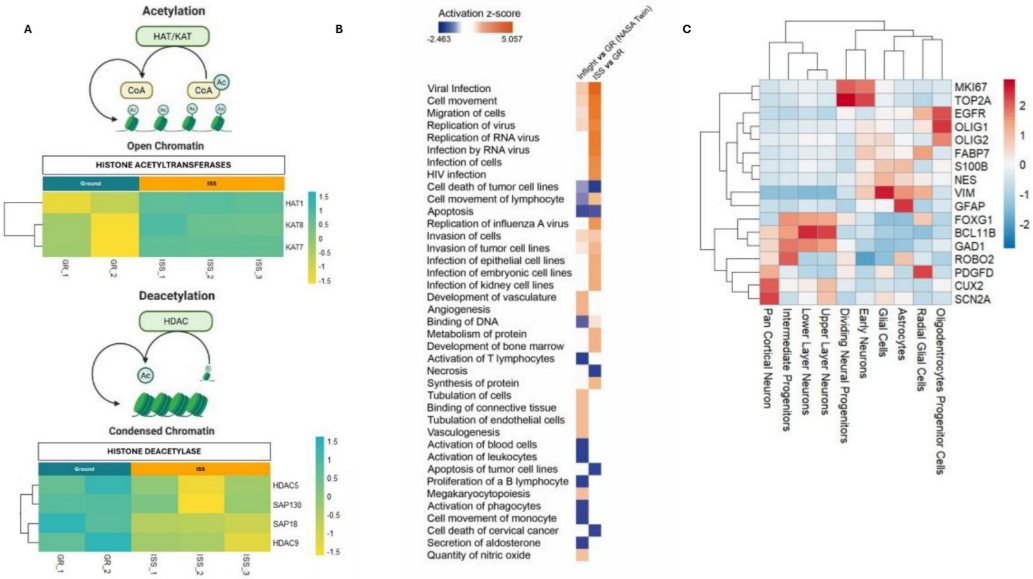

Fig. S2. Proteomics and transcriptomics approach for viral pathway evaluation. (A) Heatmap of a framework of histone proteins showing upregulation of acetyltransferases and downregulation of deacetylases at ISS. **(B)** Differentially expressed genes (DEG) comparison between this study and NASA Twin study using Ingenuity Pathway Analysis (IPA), showing canonical pathways (on the left) and diseases and biological pathways (on the right). The colors correspond to activation z-score (negative score in blue, positive in orange). For pathway analysis: *Homo sapiens* as the reference organism, minimum overlap of 3 genes, enrichment factor > 1.5, and $p < 0.01$.
(C) Heatmap of differentially expressed genes across cell types. The heatmap shows the normalized expression levels of key marker genes across different neural cell populations. Warmer colors (red) indicate higher expression levels, while cooler colors (blue) represent lower expression. Key genes exhibit distinct expression patterns across cell clusters.

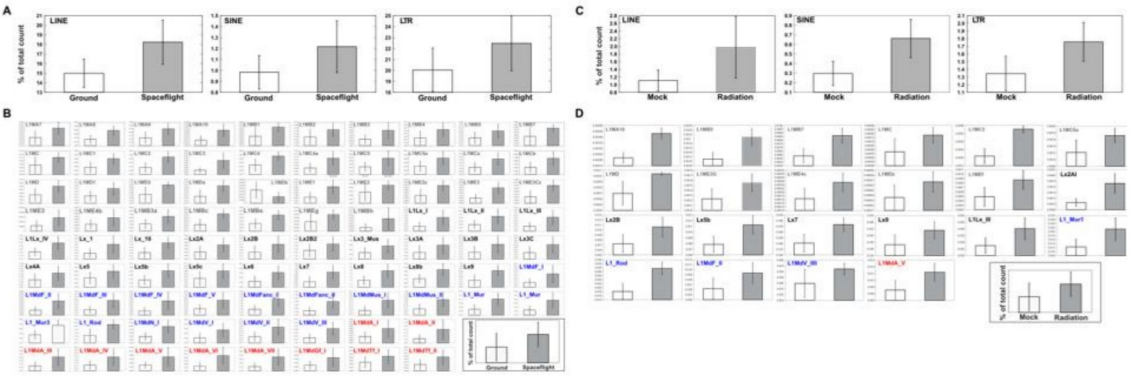

Fig. S3. Retroelement expression analysis using publicly available RNA-seq data. (A) Expression levels of transposable elements in the retina of mice exposed to space flight (GSE159771). **(B)** Subfamily-level expression of L1 elements in the spaceflight retina**. (C)** Expression of transposable elements in mouse lung following simulated five-ion galactic cosmic radiation (GSE199680) **(D)** L1 subfamily expression profiles in mouse lung under five-ion radiation condition. (**B, D**) The color of L1 subfamily members represents evolutionary age: ancient members in gray, old members in black, middle members in blue, and young members in red.

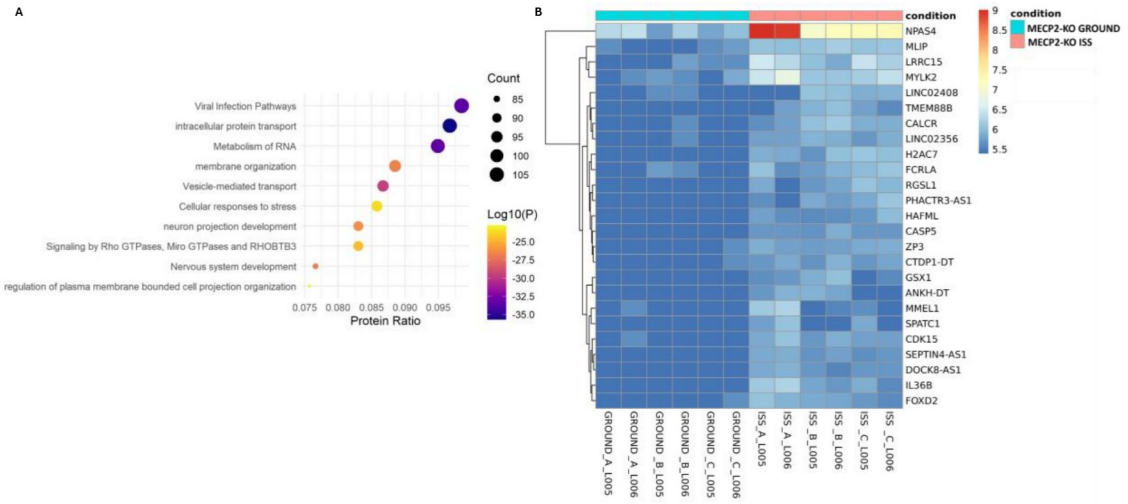

Fig. S4. Proteomics and transcriptomics analysis of MECP2-KO brain organoids experiments. (A) Reactome from the proteomic analysis comparing control cells to MECP2-KO cells in ground conditions, emphasizing that MeCP2-KO cells demonstrate upregulation of the viral pathway. This analysis highlights the intrinsic alterations in MECP2-KO cells that predispose them to enhanced viral pathway activity and nervous system development even without the influence of the space environment. **(B)** Heatmap of bulk transcriptomics comparing ground MECP2-KO brain organoids vs. ground MECP2-KO brain organoids. For proteomics bulk analysis: p≤0.01; fc≥1.2. Test T Student for comparisons. For pathway analysis: *Homo sapiens* as the reference organism, minimum overlap of 3 genes, enrichment factor > 1.5, and p < 0.01.

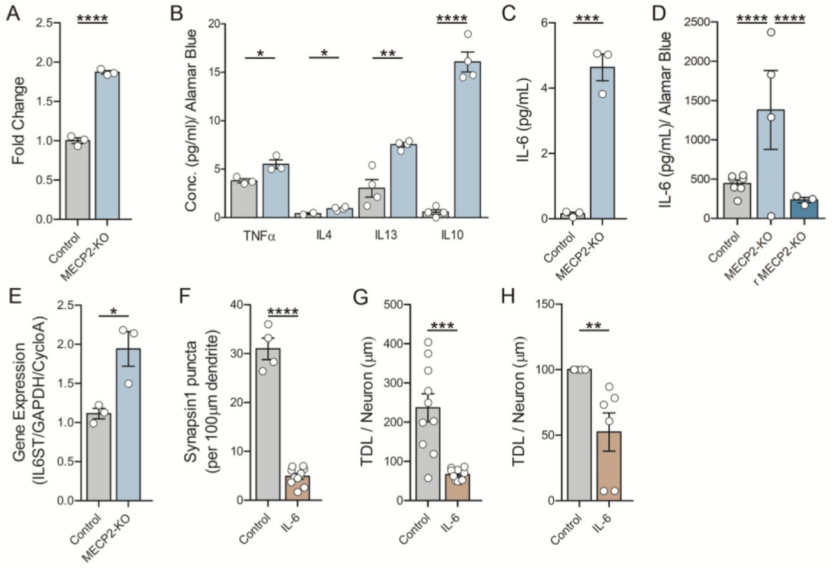

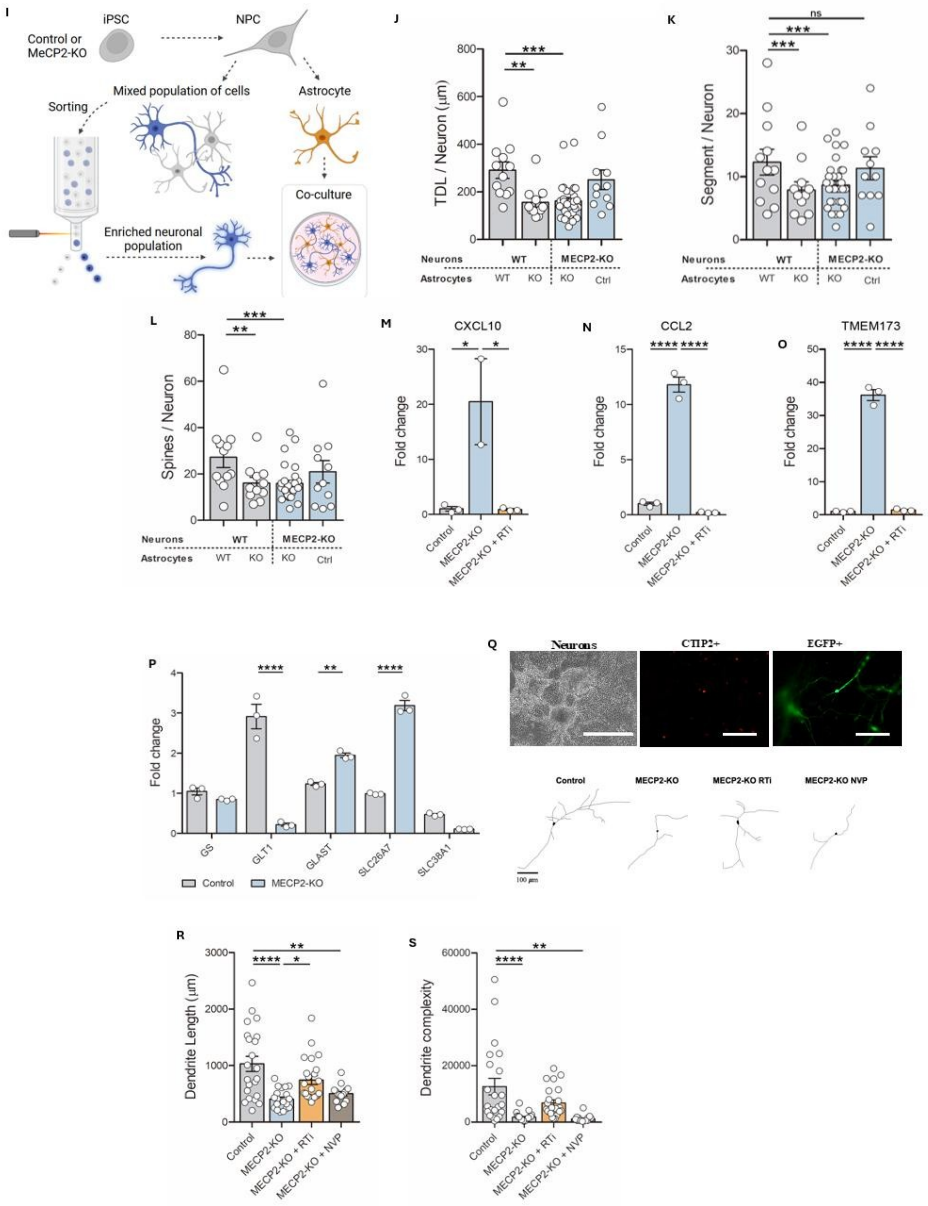

Fig. S5. MECP2-KO astrocytes phenotypes and interplay with neurons. (A) Increase L1 endogenous retroelement expression in MECP2-KO astrocytes measured by qPCR. **(B)** Quantification of TNFα, IL-4, IL-13, and IL-10 released in the media from control and MECP2-KO astrocytes by enzyme-linked immunosorbent assay (ELISA). **(C)** IL-6 protein level in post-mortem RTT brain sample compared to an age-matched control sample by ELISA. **(D)** Increased IL-6 released from RTT-derived astrocytes was rescued when MECP2 was re-expressed in the cells. The dotted red line indicates the background buffer signal for the ELISA assay. **(E)** Expression levels of the IL-6 family cytokine receptor's signal transducer, gp130 receptor (IL6ST in post-mortem RTT brain samples compared to an age-matched control sample by qPCR. **(F)** Reduction of synapsin1 puncta in control neurons upon IL-6 treatment. **(G)** Reduction of Total Dendritic Length (TDL) in control neurons upon IL-6 treatment. **(H)** Reduction of neuronal activity measured by the number of control neurons upon IL-6 treatment, measured through MEA over a 260-second time course. **(I)** Schematic diagram of the experimental design. iPSC-derived NPCs were used to produced enriched populations of neurons and astrocytes for co-cultured experiments. **(J)** Co-culture experiments of neurons and astrocytes from the two genetic backgrounds (control and MECP2-KO) showing the negative impact of MECP2-KO astrocytes in neurons regarding total dendritic length (TDL), number of segments **(K)**, and number of spines **(L)**. **(M)** Quantification of CXCL10, CCL2 **(N)**, and TMEM173 **(O)** expression in

MECP2-KO astrocytes treated with RTis by enzyme-linked immunosorbent assay (ELISA). **(P)** Quantification of GS, GLT1, GLAST, and SLC26A7 gene expression in control and MECP2-KO astrocytes compare to control. **(Q) Top:** Representative image of neurons. SYN::EGFP positive cells co-stained with a cortical marker CTIP2 and EGFP to be further traced. Scale bar, 1000 µm for neurons; Scale bar, 100 µm for CTIP+ and EGFP+ neurons. **Bottom:** Representative images of tracings from control, MECP2-KO, RTi-treated MECP2-KO, and NVP-treated MECP2-KO neurons. **(R)** Quantification of dendritic length and complexity **(S)** in mixed cultures of neurons and astrocytes. Reverse-transcriptase inhibitor (RTi) or nevirapine (NVP)-treatment is indicated. Each color represents one condition: control (black), MECP2-KO (blue), MECP2-KO+RTi (orange), and MECP2-KO+NVP (green). Each experiment was done in biological triplicates. The number of measurements (*n*) for these experiments is indicated directly by the symbols (o) on each bar graph. Data are represented as mean ±SEM; $p<0.5$ (*), $p<0.01$ (**), $p<0.001$ (***) and $p<0.0001$ (****).

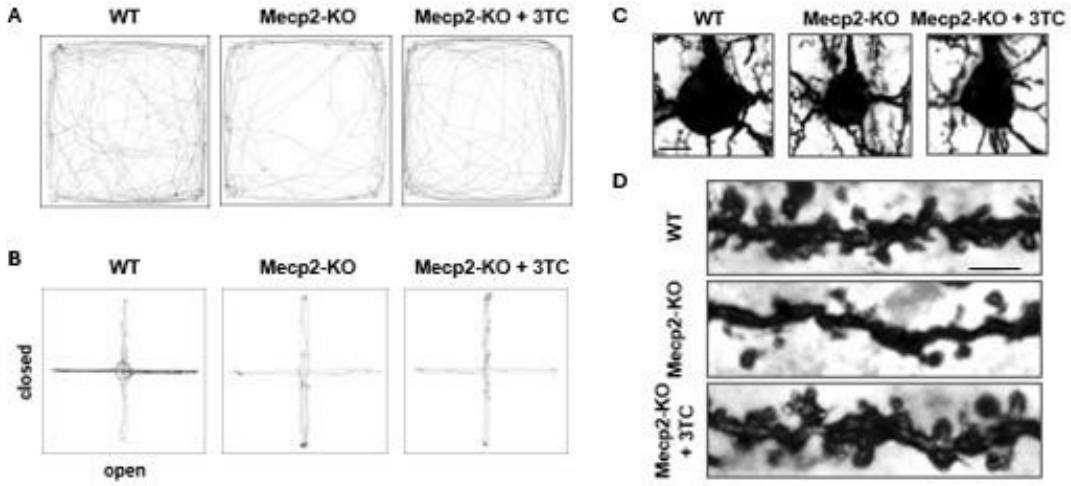

Fig. S6. RTT-like phenotypic analysis of reverse transcriptase inhibitor-treated Mecp2-KO mice. **(A)** Digital tracking of WT, Mecp2-ko and 3TC-treated Mecp2-KO mice exposed to the open-field test. Representative traces of mice activity obtained from video tracking. **(B)** Digital tracking of WT, Mecp2-ko and 3TC-treated Mecp2-KO mice exposed to the elevated plus maze test. Representative traces of mice activity obtained from video tracking. **(C)** Representative images of somata of Golgi-stained layer 2/3 pyramidal neurons in PFC of WT, Mecp2-ko and 3TC-treated Mecp2-KO mice. Scale bar, 10 µm. **(D)** Representative images of dendrites of Golgi-stained layer 2/3 pyramidal neurons in PFC of WT, Mecp2-ko and 3TC-treated Mecp2-KO mice. Scale bar, 5 µm.

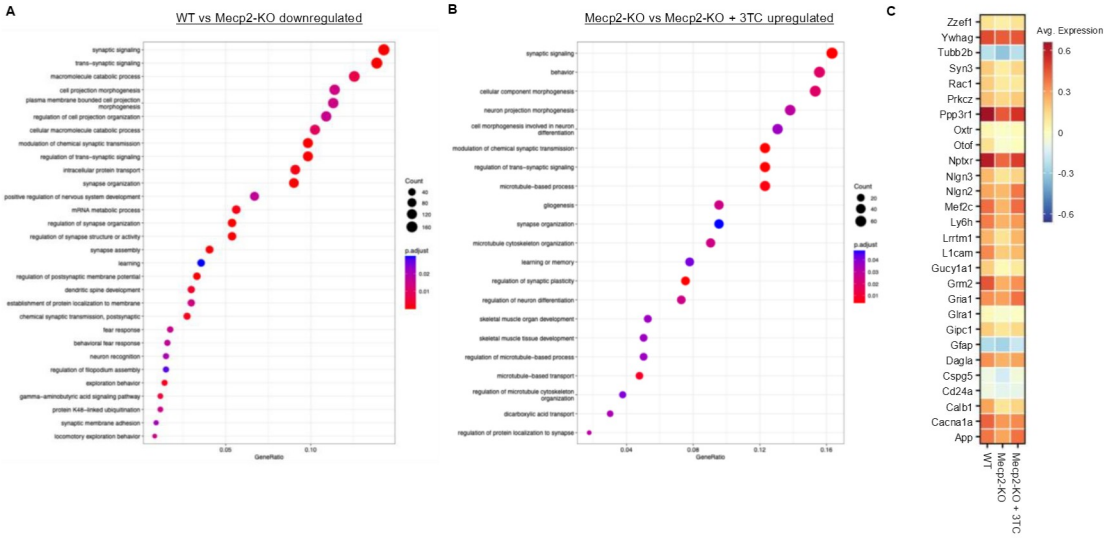

Fig. S7. Spatial transcriptomics analysis of WT, Mecp2-KO and 3TC-treated Mecp2-KO excitatory neurons. (A) GO analysis of downregulated genes in Mecp2-KO excitatory neurons compared to WT excitatory neurons. **(B)** GO analysis of upregulated genes in 3TC-treated Mecp2-KO excitatory neurons compared to Mecp2-KO excitatory neurons. **(C)** Gene expression profiles of synaptic signaling (GO:0099536) genes that were significantly downregulated in Mecp2-KO excitatory neurons compared to WT excitatory neurons and whose expression was significantly improved by 3TC treatment.

Supplementary Video 1. Representative video of WT mice performing the open field test.

Supplementary Video 2. Representative video of Mecp2-KO mice performing the open field test.

Supplementary Video 3. Representative video of Mecp2-KO+3TC mice performing the open field test.

879 **MATERIAL AND METHODS**

880 **IPSC tissue culture**

881 All iPSCs were previously characterized[86]. In addition, we also used MECP2 isogenic cell lines using
882 CRISPR/Cas9 genome editing (RTT/C9)[86]. Two isolated clones for each cell line were selected and
883 expanded for further differentiation and experimentation. Mycoplasma and CNV analyses were
884 performed regularly in all cultured cells. For consistency, "Control" or "MECP2-KO" were used in the
885 manuscript. All iPSCs were cultured and manually passaged onto Matrigel-coated (Corning) and fed
886 daily with mTESR1 (StemCell Technologies). iPSCs were differentiated into NPCs as described[87].
887 NPCs were cultured on the plate coated with 10 µg/mL of poly-L-ornithine (Sigma-Aldrich) and 2.5
888 µg/mL laminin (Life Technologies). Media was changed every other day with NG medium (DMEM/F12
889 50/50 1X (Corning Cellgro), 1% HEPES (VWR International), 0.5% Penicillin Streptomycin (Pen-Strep)
890 (Life Technologies), 1X GlutaMAX (Life Technologies), 0.5% N2 NeuroPlex (Gemini Bio-Products) and
891 1% Gem21 NeuroPlex (Gemini Bio-Products) was supplemented with 20 ng/mL basic human fibroblast
892 growth factor (bFGF) (R&D Systems, 414-TE).

893 **Neural differentiation**

894 For neural differentiation, bFGF was withdrawn from the NPCs containing NG media, and Rock inhibitor
895 (Y27632) was added at a concentration of 10ng/mL for 48 hours. Cells matured for 5 to 8 weeks,
896 replacing the media every 3 to 4 days. IPSC-derived cortical organoids were differentiated following[1].
897 Briefly, iPSCs were cultured, dissociated using a 1:1 Dulbecco's phosphate-buffered saline (DPBS,
898 Fisher Scientific) and StemPro Accutase solution, transferred to 6-well plates, and kept in suspension.
899 Neural induction media consisted of DMEM/F12, 1% Glutamax, 1% N2 Neuroplex, 1% non-essential
900 amino acids (Gibco), 1% Pen-Strep, 1µM of Dorsomorphin (R&D Systems), and 10µM SB431542 (SB,
901 Stemgent). Neural proliferation media consisted of Neurobasal media (Life Technologies), 2% Gem21
902 Neuroplex, 1% non-essential amino acids, 1% Glutamax, 20 ng/mL epidermal growth factor (EGF,
903 Peprotech), and 20 ng/mL bFGF. For neuronal maturation, the cells were kept in the same media, but
904 the growth factors were withdrawn. Organoid results are combined from four separate batches of
905 differentiation.

906 Astrocytes were differentiated as described[88]. Briefly, monolayer NPCs are dissociated into single-cell
907 suspension using StemPro Accutase. To form astrospheres, cells were seeded at a density of 4-5
908 million cells per well in a 6-well plate (Genesee, 25-105) shaking at 95 r.p.m. at 37˚C in NSCR EL
909 medium containing DMEM/F12 (Gibco) with 1% N2 supplement (Gibco) and 0.1% SM1 supplement,
910 1% nonessential amino acids (Gibco), 1% penicillin/streptomycin (Gibco), 1% GlutaMAX solution
911 (Gibco), supplemented with 20 ng/ml epidermal growth factor 1 (EGF-1, Peprotech) and 20 ng/mL
912 leukemia inhibitory factor (LIF, Peprotech). Following 2-4 weeks in the NSCR EL media, the
913 astrospheres were expanded in NSCR media now supplemented with 20 ng/mL EGF and 20 ng/mL
914 FGF (NSCR EF) for 2-4 weeks. Following this expansion phase, astrospheres were plated on 20 µg/mL
915 poly-L-ornithine and 5 µg/mL laminin and remained in NSCR EF media, allowing astrocyte progenitor
916 cells (APCs) to migrate outward until 70% confluency. For astrocyte assays, progenitors were expanded
917 and seeded at 50,000 cells/well in a 96-well plate. These progenitor cells can be expanded and frozen
918 in cryovials for later use. For differentiation into mature astrocytes, media was changed to contain half
919 of the NSCR basal media and half Astromed CNTF media. Astromed media contained Neurobasal
920 media (Gibco) with 0.2% SM1, 1% NEAA, 1% penicillin/streptomycin, 1% Glutamax and 10ng/mL of
921 ciliary neurotrophic factor (CNTF, Peprotech). After 48 hours, cells were transitioned into full Astromed
922 CNTF media for 14 days.

923 **CubeLab operations (flight and ground)**

Space Tango's flight and ground hardware support 12 wells containing impellers and automated operations (fluid conveyance, fluid routing, thermal control, environmental monitoring, imaging, and sampling) within each 9U CubeLab™. All wetted materials selected within the CubeLab were certified biocompatible and sterilizable. Wetted materials that come in contact with fluids or cells were sterilized, assembled, maintained sterile, tested, and confirmed to be free of microbial contamination prior to loading experimental fluids and biology. Science and the Flight system CubeLab were prepared at the Kennedy Space Center (KSC) Space Station Processing Facility (SSPF) in Brevard County, FL. Scheduled operations began shortly after science loading, continuing through launch, ascent, and on-orbit, and ended upon fixation and transfer to cold stowage. Space Tango's Powered Ascent Utility Locker (PAUL) allows CubeLabs to be fully powered while installed in the SpaceX Cargo Dragon vehicle. The PAUL provides the optimal culture environment and capabilities for the entire time the science remains within the CubeLab, including while on the launch pad. Flight and Ground systems were run synchronously. The Ground system scheduled operations were initiated 9 days after the Flight system.

The Flight system CubeLab culture environment was maintained at 37°C and 5–7% CO_2, and culture media was held at 2–8°C, providing optimal culture conditions. Media exchanges were performed every 3 – 4 days using microfluidic routing and pumping. Organoids were exposed to the CubeLab environmental gases through a 10:1 (base:curing agent) polydimethylsiloxane (Sylgard 184, Dow) interface within each well cap. Impeller-driven agitation was required for the Flight system on Earth, through ascent and installation, and during media exchanges. During all other times, no agitation was performed. Imaging of wells was performed twice per week for 30 days, beginning after installation and ending prior to cold stowage transfer. SpaceX mission CRS-25 was 30 days. On the 30th day of on-orbit operations, 4% paraformaldehyde fixation of 6 wells and RNALater fixation of the remaining 6 wells was performed. The Flight system was stored at approximately 4°C for 6 days until science removal at the SSPF. Additionally, Space Tango's cryovial flight hardware contains 6 stainless steel boxes, each supporting up to 98 1 mL cryovials (Nunc, 374088) for up to 588 1 mL cryovials per 9U CubeLab™. The Flight system CubeLab culture environment was maintained at 37°C and 5% CO_2, providing optimal environmental culture conditions. SpaceX CRS-25 mission was 30 days. Ground control samples were loaded into 1x stainless steel cryovial box and maintained within a humidified incubator set to 37°C and 5% CO_2, located at the SSPF, until the flight samples returned to Earth. Flight and ground samples were run synchronously, and scheduled operations were initiated at the exact same time.

The Ground system experiment was performed at the Space Tango Headquarters in Lexington, KY. The CubeLab culture environment was maintained at 37°C, and 5–7% CO_2, and culture media was held at 2–8°C, providing optimal culture conditions. Media exchanges were performed every 3–4 days using microfluidic routing and pumping. Impeller-driven agitation was required for the Ground system throughout the entire experiment on Earth. Imaging of wells was performed during media exchanges only due to impeller movement. On the 30th day of matched on-orbit operations, 4% paraformaldehyde fixation of 6 wells and RNALater fixation of 6 wells was performed. The Ground system was stored at approximately 4°C for 17 days until scientific removal. CubeLab environmental telemetry (culture environment temperature, temperature of culture media, CubeLab CO_2, CubeLab humidity) was recorded during powered operations. Telemetry data was available in near real-time through Space Tango's customer dashboard.

Imaging operations and post-processing (flight and ground)

During the ascent phase, agitation was enabled continuously on all wells. 13-second videos were recorded once per hour for each well during this time. Once installed into the ISS, the constant agitation period was discontinued. This was changed to record videos during the agitation event during the media exchanges, which occurred every 3.5 days. To get more insight into how well the organoids were

growing, a health check was added after the first 2 media exchanges. The health check involved capturing a photo of each well once per hour for the remainder of the mission. Post-processing included adding a scale bar onto each image that represents the size of 1mm in the image. Images were uploaded to Space Tango's data portal. The ground study payload had constant agitation enabled from the experiment start until fixation. During this time, 13-second videos were recorded once per hour for each well. Additionally, health check images were added before and after each media exchange at an interval of 3.5 days. Post-processing included adding a scale bar onto each image that represents the size of 1mm in the image. Images were uploaded Space Tango's data portal.

Mass spectrometry bulk analysis

A total of 500 ng of each sample was randomized loaded onto individual Evotips trap columns following manufacture's protocol. The peptides were separated using an Evosep One LC system (Evosep, Denmark) in 44 min gradient (30 samples per day predefined Evosep proprietary method) on a PepSep 8 (8 cm × 150 µm X 1.5 µm C18 column, Bruker Daltonics) at 50°C. The mobile phases were 0.1% FA in LC-MS grade water (buffer A) and 0.1% FA in 99.9% ACN (buffer B). The LC system was coupled with timsTOF Pro 2, a hybrid trap ion mobility spectrometer and quadrupole time-of-flight instrument (Bruker Daltonics) operated in positive mode previously calibrated for mass (m/z) and ion mobility dimension (1/K0), using three ions of Agilent ESI-Low Tuning Mix (m/z 622.0289; 922.0097 and 1221.9906). The nano-electrospray source (CaptiveSpray source, Bruker Daltonics) was operated at 1600 V of Capillary voltage, 3.0 L/min of dry gas, and 180 °C of dry temperature. Data was acquired in dia-PASEF acquisition mode with a cycle time estimate of 1.8 s46. To cover the mass range of 400 to 1200 m/z, 32 isolation windows of 25 m/z width were used. Ramp Time and accumulation time were set to 100 ms, and collision energy ramped linearly as a function of the mobility from 59 eV at 1/K0 = 1.6 Vs. cm−2 to 20 eV at 1/K0 = 0.6 Vs. cm−2.

Data processing for mass spectrometry-based bulk proteomics

All diaPASEF data was imported in Spectronaut (v.19, Biognosys) and processed using directDIA workflow which does not require spectral library from DDA runs. In brief, Spectronaut Pulsar search engine firstly generates DDA-like pseudospectra from the fasta database and then performs searches. The human protein reference database (UP000005640 reviewed canonical proteins) was used with Pulsar and the following settings: Trypsin/P as specific enzyme; peptide length from 7 to 52; max missed cleavages 2; toggle N-terminal M turned on; Carbamidomethyl on C as fixed modification; Oxidation on M and Acetyl at protein N-terminus as variable modifications; FDR at PSM, peptide and protein group level set to 0.01; minimum fragment relative intensity 1%; 3–6 fragments kept for each precursor; the extraction of the ion chromatograms and ion mobility window was set as "dynamic" with correction factor 1.

Functional analysis for mass spectrometry-based bulk proteomics

The interpretation of systems-level studies was done on Metascape, an online platform that provides a comprehensive resource for annotating and analyzing gene/protein lists[53]. In this study, we used enrichment analysis to compare thousands of protein sets defined by their involvement in specific biological processes, protein localization, enzymatic function, pathway membership, and protein network analysis and interactions. All data was post-processed to generate Kappa similarities, and all pairs of enriched terms were computed into clusters of comparable terms[54].

The proteins quantified in at least 70% of the samples within each group were subjected to statistical and graphical analyses using the R programming environment. Abundance values were log10-transformed prior to analysis. Boxplots were generated using the ggplot2, dplyr, and tidyr packages[89]. Heatmaps were constructed using the heatmap REF package, based on ANOVA p-values to highlight differential expression patterns. Volcano plots were created using the ggplot2 and ggrepel REF

packages. Gene Ontology (GO) enrichment analyses were performed using Cytoscape[90] and STRING[91].

Protein identifiers and associated statistics ($\log_2$ fold change and adjusted p-values) were submitted to Metascape (www.metascape.org) for pathway enrichment analysis. Parameters were set to default values: *Homo sapiens* as the reference organism, minimum overlap of 3 genes, enrichment factor > 1.5, and $p < 0.01$. The resulting output was used for downstream processing, focusing on the table containing pathway description, enrichment ratio, $-\log_{10}$(p-value), and the number of proteins contributing to each term. Data visualization was performed in R (version 4.3.2) using the readxl, ggplot2, and viridis packages. The enriched pathways were ordered according to their enrichment ratio, and a dot plot was generated to display the top biological processes. In the plot, the x-axis represents the enrichment ratio (GeneRatio), the y-axis lists pathway descriptions, dot size corresponds to the number of input proteins (Count), and dot color encodes statistical significance based on $-\log_{10}$(p-value).

Secretome panel evaluation by Proximity Extension Assay (PEA) Olink® Reveal (Thermo Fisher Scientific)

The Olink Reveal technology uses Proximity Extension Assay (PEA)[92], where a matched pair of antibodies labelled with unique complementary oligonucleotides (proximity probes) bind to the respective target protein in a sample. As a result, the probes come into close proximity and hybridize to each one, enabling DNA amplification of the protein signal, which is quantified on a next generation sequencing read-out which has been described in detail previously. Antibodies targeting 1034 unique proteins are distributed across 384-plex panel. Assays are run in a 96-well format. Each plate consisted of 32 secretome samples (in triplicates) from brain organoids that belong to the ground experiment and the ISS experiment, using 20 µL of media sample. In brief, pairs of oligonucleotide-labeled antibody probes designed for each protein bind to their target, bringing the complementary oligonucleotides in close proximity and allowing for their hybridization. The addition of a DNA polymerase leads to the extension of the hybridized oligonucleotides, generating a unique protein identification "barcode". Next, library preparation adds sample identification indexes and the required nucleotides for Illumina sequencing. Prior to sequencing using the Illumina® NovaSeq™ 6000/NextSeq™ 550/NextSeq™ 2000, libraries go through a bead-based purification step and the quality is assessed using the Agilent 2100 Bioanalyzer (Agilent Technologies, Palo Alto, CA). The raw output data is quality controlled, normalized and converted into NPX®, values as their log-2 scaled quantification unit of relative abundance. Data normalization is performed using an internal extension control and an external plate control to adjust for intra- and inter-run variation. All assay validation data (detection limits, intra- and inter-assay precision data, predefined values, etc.) are available on manufacturer's website (www.olink.com). Data was processed by Olink's MyData Cloud Software.

RNA sequencing and transcriptomic analysis

For transcriptomic analyses, we combined brain organoids from the three healthy donors for ground processing for RNA sequencing. Ribodepletion RNA sequencing was performed at the UC San Diego IGM core facility. Data was analyzed by ROSALIND® (https://rosalind.bio/), with a HyperScale architecture developed by ROSALIND, Inc. (San Diego, CA). Briefly, reads were trimmed using cutadapt. Quality scores were assessed using FastQC. Reads were aligned to the Homo sapiens genome build hg19 using STAR. Individual sample reads were quantified using HTseq and normalized via Relative Log Expression (RLE) using DESeq2 R library. Read Distribution percentages, violin plots, identity heatmaps, and sample MDS plots were generated as part of the QC step using RSeQC. DEseq2 was also used to calculate fold changes and p-values and perform optional covariate correction. The clustering of genes for the final heatmap of differentially expressed genes was done using the PAM (Partitioning Around Medoids) method using the fpc R library. Hypergeometric distribution was used to analyze the enrichment of pathways, gene ontology, domain structure, and

other ontologies. The topGO R library was used to determine local similarities and dependencies between GO terms to perform Elim pruning correction. Several databases were referenced for enrichment analysis, including Interpro, NCBI, MSigDB, REACTOME, WikiPathways. Enrichment was calculated relative to a set of background genes relevant to the experiment. Functional enrichment analysis of pathways, gene ontology, domain structure, and other ontologies was performed using HOMER.

In our study, we employed the DESeq2 package in R for differential expression analysis, utilizing a significance threshold of $p < 0.05$. Raw count data, obtained from experimental samples representing ground and ISS conditions, were processed and normalized. Subsequently, differential expression analysis was performed, allowing for the identification of genes significantly altered between the two conditions, with a fold change threshold of 1.5. Additionally, to gain insights into the biological pathways underlying these expression changes, Reactome pathway analysis was conducted on the differentially expressed genes, with a significance threshold of $p < 0.05$. Furthermore, we performed additional pathway analysis using Wiki Pathways library, employing a false discovery rate (FDR) adjusted p-value cutoff of 0.1, to further elucidate the enriched biological processes associated with the observed gene expression alterations.

Xenium experiment

Mice were anesthetized and perfused trans-cardiac with PBS followed by 4% buffered paraformaldehyde (PFA). Brains were removed and fixed with 4% PFA overnight at 4°C. The fixed tissue was cryoprotected with 30% sucrose and frozen in optimal cutting temperature medium (OCT). Coronal sections were obtained by sectioning the tissue at 10 µm using Leica CM3050S cryostat. Sections were washed with PBS and placed onto Xenium slides.

The Xenium 5K Mouse Pan-Tissue and Pathways Panel (10x Genomics) was used for transcriptomic profiling. Probe hybridization, RNase treatment, ligation, amplification, and cell staining were performed according to the manufacturer's protocol. Data acquisition and on-board analysis were conducted using the Xenium Analyzer (v3.3).

Xenium data processing

Regions of interest (ROIs) in the WT, Mecp2-KO, and 3TC-treated Mecp2-KO brains were manually selected using Xenium Explorer 3 (v3.1.1). Only cells within ROIs with more than 250 detected genes and more than 350 transcripts were included in downstream analysis. Data normalization, principal component analysis (PCA), UMAP-based dimensionality reduction, and cell clustering were performed using the Seurat package (v5.0.1). Cell type annotations were manually assigned based on the expression of established marker genes. Differential gene expression analysis was performed using the FindAllMarkers function in Seurat. Over-representation analysis of genes included in the predefined gene list of the Xenium panel in the transcriptome data of brain organoid samples returned from the ISS was performed using Fisher's Exact Test. Gene Ontology (GO) analysis of Biological Processes was conducted using the clusterProfiler package (v4.4.4).

Reverse Transcriptase inhibitors

The reverse-transcriptase inhibitors for cultured cells were prepared as follows: Lamivudine (3TC, Sigma-Aldrich) was prepared in dimethyl sulfoxide (DMSO, Sigma-Aldrich), and 10 µM of 3TC was used in the media. Stavudine (d4T, Sigma-Aldrich) was re-suspended in water, and 1µM of d4T was used in the media in combination with 3TC. Nevirapine (Sigma Aldrich, SML0097) was re-suspended in DMSO and 400 nM nevirapine was used in media. Control cells contained 10 µM of DMSO as a vehicular control.

1109 **Immunofluorescence**

1110 Cells cultured in monolayer were washed with DPBS, fixed in 4% paraformaldehyde (PFA, Core Bio)
1111 for 20 minutes at room temperature, and permeabilized with a solution of DPBS and 0.1% Triton X-100
1112 (Promega) for 10 minutes at room temperature. Cells were incubated at room temperature with blocking
1113 solution for 30 minutes (DPBS, 10% donkey or goat serum (Fisher Scientific), and 0.005% Triton X-
1114 100). Primary and secondary antibodies were diluted in a solution containing DPBS, 1% donkey or goat
1115 serum, and 0.005% Triton X-100. Cells were incubated with the primary antibody overnight at 4˚C. The
1116 next day, cells were washed with DPBS three times for 5 minutes and incubated with secondary
1117 antibodies for 30 minutes at room temperature. Cells were washed twice with DPBS, and nuclei were
1118 stained using DAPI (VWR International) for 10 minutes at room temperature. Finally, cells were washed
1119 once with DPBS for 5 minutes, and the coverslips were mounted using Prolong Gold antifade mounting
1120 (Life Technologies) onto glass slides (Fisher Scientific).

1121 For cortical brain organoids, cells were washed with DPBS and placed in a 1.5 mL microcentrifuge tube
1122 with 4% PFA overnight at 4˚C. Cortical organoids were washed with DPBS and incubated in 30%
1123 sucrose (Sigma-Aldrich) for 48 hours at 4˚C. The tissue was removed from the sucrose solution, placed
1124 with optimal cutting temperature compound (OCT, VWR) within an embedding mold (Fisher Scientific),
1125 and incubated at -80˚C overnight. Using a cryostat (Leica), the molds containing the organoids were
1126 sliced at 10.0 µm and placed onto a glass slide which was left to dry at room temperature for at least 4
1127 hours. The slides were lined with a hydrophobic barrier pen (Vector Laboratories). Organoid slides were
1128 permeabilized, stained, and mounted as explained above.

1129 **Immunohistochemistry**

1130 Mice were anesthetized and perfused trans-cardiac with PBS followed by 4% buffered
1131 paraformaldehyde (PFA). Brains were removed and fixed with 4% PFA overnight at 4°C. The fixed
1132 tissue was cryoprotected with 30% sucrose and frozen in optimal cutting temperature medium (OCT).
1133 Coronal sections were obtained by sectioning the tissue at 40 µm using Leica CM3050S cryostat.
1134 Sections were washed with PBS to remove the OCT, permeabilized and blocked with blocking buffer
1135 at RT for 1 h, and then incubated with primary antibody diluted in blocking buffer overnight at 4°C. After
1136 three washes with PBS, the sections were incubated with corresponding secondary antibodies at RT
1137 for 2 h. The following primary and secondary antibodies were used in this experiment: rabbit anti-hC3D
1138 (1:500; DAKO, Cat.# A0063), mouse anti-S100β (1:500; Sigma, Cat.#S2532); CF488 donkey anti-
1139 mouse IgG (H+L), highly cross-adsorbed (1:500; Biotium), CF555 donkey anti-rabbit IgG (H+L), highly
1140 cross-adsorbed (1:500; Biotium). Hoechst 33258 (1:500) was used for nuclear staining. After three
1141 washes with PBS, the sections were mounted on glass slides. Fluorescence images of astrocyte were
1142 acquired using Zeiss LSM 800 confocal microscope.

1143 **Magnetic cell sorting**

1144 Briefly, iPSC-derived cells were dissociated using the neurosphere dissociation kit (MACS), incubated
1145 with the CD44-PE and CD184-PE (both antibodies were from BD Biosciences) for 15 minutes in the
1146 dark at 4°C and washed twice with dPBS to remove unbound antibodies before sorting. Next, the cells
1147 were incubated with PE antibodies and conjugated with magnetic beads (MACS). Following the
1148 antibody incubation, cells are loaded into a magnetic column, and the cells that are CD44 and CD184
1149 positive are retained in the column. The remaining enriched neuronal population is obtained and
1150 counted for viability and seeding.

1151 **Astrocyte calcium wave propagation**

1152 Calcium waves were induced by focal mechanical stimulation of single astrocytes in the center of the
1153 field of view. A 175 W Xenon lamp and a wavelength switcher (Lambda DG-4, Sutter Instrument)

1154 provided 485 nm fluorescence excitation. The emission from Fluo-4 loaded cells is detected at a
1155 wavelength of 520 nm using a F-Fluar 40X/1.3 NA oil immersion objective and an attached 12-bit CCD
1156 camera. Changes in Fluo-4 fluorescence intensities emitted at 520 nm were acquired at 0.67 Hz. The
1157 calcium imaging data were visualized and analyzed offline using MetaMorph software (Universal
1158 Imaging Corporation). The fluorescent intensity of Fluo-4 was determined in individual cells in every
1159 astrocyte soma in the field of view. The distance that calcium waves propagated within a certain time
1160 was determined by measuring the distance from the stimulating point to the farthest responding cell in
1161 the field of view.

1162 **Morphological analysis of iPSC-derived neurons**

1163 Cultured NPCs were transduced with a lentivirus backbone containing Synapsin 1 (SYN) promoter
1164 upstream of an EGFP reporter[93]. The transduction multiplicity of infection (M.O.I.) was equal to 2. Cells
1165 transduced with a SYN::GFP lentivirus were differentiated into neurons for 5-6 weeks, fixed, and stained
1166 with GFP and CTIP2 antibodies. Differentiated neurons were traced using Neurolucida v.2017 (MBF
1167 Bioscience, Williston, VT) connected to a Zeiss Axio Imager 2 microscope at a 40X oil objective. Only
1168 neurons that were both GFP- and CTIP2-positive were included in this analysis. The morphology of the
1169 neurons was quantified using Neurolucida Explorer v.11 (MBF Bioscience, Williston, VT), and the
1170 results reflect the summed length of all neurites and dendrites per traced neuron. Sholl analysis was
1171 performed using Neurolucida Explorer's Sholl analysis. This analysis specified a center point within the
1172 soma and created a grid of concentric rings around it with radii increasing in 10 µm increments.
1173 Neuronal complexity was determined by recording the number of intersections within each ring.

1174 **Synaptic puncta quantification**

1175 5-6-week-old neurons were fixed and stained for the following markers: SYN1, postsynaptic density
1176 protein 95 (PSD-95), and MAP2 (refer to **Immunocytochemistry** for protocol). Using a fluorescence
1177 microscope (Z1 Axio Observer Apotome Zeiss), the slides were imaged by compiling Z stack images
1178 taken from incremental focus distances. Co-localized SYN1 (presynaptic) and PSD-95 (postsynaptic)
1179 were quantified using the compiled Z stack image. Only co-localized puncta that were in proximity of a
1180 MAP2-positive neurite were included in this analysis.

1181 **Measurement of cortical organoid diameter**

1182 Cortical organoids were imaged on an Evos FL Imagine System (Thermo Fisher Scientific) using a 4X
1183 magnification. The images were uploaded to Image J, and the diameter of each organoid was
1184 determined by the program's length measurement.

1185 **RNA extraction and qPCR**

1186 RNA was extracted using the RNAse Plus Mini Kit (Qiagen). Briefly, adherent cells were washed with
1187 DPBS and further lysed using RLT buffer with B-mercaptoethanol (Thermo Fisher Scientific) and
1188 dissociated using a 1mL syringe (Fisher Scientific, 1482330) and a needle (VWR, BD- 305196). RNA
1189 from lysates was extracted following the manufacturer's instructions. cDNA was generated using the
1190 Qiagen Quantitect Reverse Transcription Kit. Protocol was followed on 1 µg of the RNA samples. qPCR
1191 was performed using selected primers and SYBR Green master mix (BioRad). Diluted cDNA was used
1192 in a 96-well or 384-well plates (BioRad) and ran on a BioRad CFX machine. PCR conditions were as
1193 follows: initial cycle of 95ºC for 32 min, followed by 40 cycles of 15s at 95ºC, 30s at 58ºC, 30s at 72ºC,
1194 with a final step of 5s at 57ºC and 5s at 95ºC for the melting curve. 3 plates were run to obtain triplicates
1195 per condition. The L1 primers used were: ORF1:
1196 ATGGGGAAAAAACAGAACAGAAAAACTGGAAACTCTAAAACGCAGAGCGCCTCTCCTCCTCCAA
1197 AGGAACGCAGTTCCTC; ORF2:
1198 GCTCATGGGTAGGAAGAATCAATATCGTGAAAATGGCCATACTGCCCAAGGTAATTTACAGATTC

1199 AATGCCATCCCCATC; ORF2-3′UTR:
1200 TGGAAACCATCATTCTCAGTAAACTATCGCAAGAACAAAAAACCAAACACCGCATATTCTCACTCA
1201 TAGGTGGGAATTGA

1202 **PCR array**

1203 A PCR array was performed using RT^2 Profiler PCR Array 384 format (Qiagen), following the
1204 manufacturer's instructions. Briefly, 400 ng of total RNA was used for reverse transcription using the
1205 RT^2 First Strand Kit (Qiagen). Genomic DNA was eliminated prior to reverse transcription. Real-time
1206 PCR was performed using RT^2 SYBR Green Mastermix and cDNA mix, divided into 384 wells. Plates
1207 were sealed with Optical Adhesive Film and ran into a CFX384 (BioRad). Run conditions: 1 cycle of 10
1208 min at 95ºC, followed by 40 cycles of 15s at 95ºC and 1 minute at 60ºC, where data collection was
1209 performed. For data analysis, GeneGlobe Data Analysis Center was used. Reference genes used:
1210 peptidyl-prolyl cis-trans isomerase H (PPIH), glyceraldehyde-3-phosphate dehydrogenase (GAPDH),
1211 Non-POU Domain Containing Octamer Binding (NONO), Lactate dehydrogenase A (LDHA), Actin Beta
1212 (ACTB). Significant changes in gene expression were set to a min of 2fold differences.

1213 **Multi-electrode array (MEA)**

1214 12-well MEA plates (Axion Biosystems) were coated with 100 µg/mL of poly-L-ornithine (Sigma-Aldrich)
1215 and 5 µg/mL laminin (Life Technologies). Cultures were placed in the center of the MEA well to fully
1216 cover the electrodes. Media was changed twice a week, and recordings were measured one day after
1217 the media was changed. Recordings were performed once a week using a Maestro MEA System and
1218 AxIS Software (Axion Biosystems). A band-pass filter with 10 Hz and 2.5 kHz cutoff frequencies was
1219 used, and a spike detector threshold was set at 5.5 times the standard deviation. For each recording,
1220 the plate was left untouched in the Maestro for 3 minutes prior to recording, then 3 minutes of data were
1221 recorded. Analysis was performed using Axion Biosystems Neural Metrics Tool. The criteria to detect
1222 an active electrode was set to 5 spikes per minute, and the criteria to detect a burst electrode was set
1223 to 5 bursts per minute.

1224 **TUNEL assay**

1225 Cells were cultured with the different treatments on 96-well plates, and once confluent, the cells were
1226 fixed with 4% PFA and permeabilized with 0.1% Triton X-100 for 15 minutes. Cells were blocked with
1227 3% bovine serum album (Gemini) for 1 hour. Cells were incubated with primary antibodies of Nestin
1228 and TUNEL (Click-iT TUNEL assay kit, Life Technologies) overnight at 4˚C. The following day, cells
1229 were incubated with secondary antibodies for 30 minutes at room temperature and with DAPI for 5
1230 minutes at room temperature. Cells were mounted using Prolong Gold Antifade mounting, and images
1231 were taken and manually quantified.

1232 **IL6 Elisa**

1233 Astrocyte progenitor cellss were dissociated using 1:1 Accutase:PBS for three minutes and seeded at
1234 50.000 cells/well in a 96-well plate. Following 14 days of differentiation with CNTF, astrocyte media was
1235 conditioned for 48 hours and tested for the presence of IL6 without exogenous stimulation (R&D
1236 Systems). All samples were assayed in triplicate following the manufacturer's instructions for cell culture
1237 supernatant. To confirm the functionality of the iPSCs-derived astrocytes, selected wells were
1238 stimulated with 10ng/ml interleukin-1-β (IL-β) during 48 hours prior to IL-6 analysis. Optical density was
1239 measured at 450 nm with wavelength correction set to 540 nm using the Tecan Infinite Pro 200 plate
1240 reader. Standards were assayed in duplicates, and samples were assayed in triplicates. The
1241 corresponding plate was fixed and stained for normalization. Images were taken using Z1 Axio
1242 Observer Apotome Zeiss, and 8-10 pictures were taken per condition. GFAP-positive cells were

1243 manually counted, and DAPI was quantified using Fiji-ImageJ imaging. Recombinant human IL6 was
1244 added as a positive control.

1245 **ROS Assay**

1246 Astrocyte progenitors were plated at a density of 50,000 cells/well in a white-walled, clear bottomed 96
1247 well plate (Corning) and differentiated for 14 days with CNTF. ROS-Glo H2O2 (Promega) Homogenous
1248 (Lytic) protocol was followed according to the manufacturer's instructions. Astrocytes and RTI
1249 treatments were conditioned in the Astromed media for 48 hours. The H_2O_2 substrate solution was
1250 added to the plate and treated for 4 hours before ROS Glo detection solution was added. The relative
1251 luminescence was recorded using a Tecan Infinite Pro 200 plate reader. Six replicates were run per
1252 condition.

1253 **Glutathione Assay**

1254 GSH-GLO Glutathione Assay (Promega V6911) protocol for adherent mammalian cells was followed
1255 according to the manufacturer's instructions to measure glutathione levels present in astrocytes. Cells
1256 were seeded at 50,000 cells/well on a white-walled 96 well plate. The medium was removed, 1X GSH-
1257 Glo reagent was added to the cells and incubated for 30 minutes at room temperature. Following the
1258 addition of Luciferin Detection reagent, relative luminescence was recorded using Tecan Infinite Pro
1259 200 luminometer. Values were normalized to GFAP+ expressing cells.

1260 **Glutamate Assay**

1261 The glutamate assay (ab83389) was used to detect extracellular glutamate levels. Astrocytes
1262 differentiated with CNTF for 14 days were plated in 96-well plates to confluency. The media was
1263 conditioned for 48 hours.

1264 **Ca^{2+} Flux Assay**

1265 Rhod-4 No Wash Calcium Assay Kit was performed following the manufacturer's instructions. iPSCs-
1266 derived neurons were grown in a 96-well plate and cultured in NG media. Media was changed 48 hours
1267 prior to the experiment.100ul of Rhod-4 Dye-Loading Solution was added per well and incubated at
1268 room temperature for 1 hour. Calcium flux assay was run by monitoring the fluorescence intensity at
1269 Ex/Em = 540/590 nm. Images were acquired for 20 seconds (approximately 600 frames) per field. For
1270 analysis, calcium fluorescence traces were retrieved using customized software, Netcal (Orlandi et al.,
1271 2017) based on MatLab software®. First, a manual selection of Regions of Interest (ROIs) was carried
1272 out to track the activity of all the cells in the culture, both neurons and astrocytes. After analyzing the
1273 recording, further post-processing allows the division of the traces into 2 groups with different firing
1274 behavior: neurons that display a sharp and fast increase of fluorescence followed by a rapid decline in
1275 the wave function. These astrocytes have a slow progression in the fluorescence intensity and a similar
1276 slow decrease in intensity. The classification of the traces was done by training the Netcal program with
1277 the same parameters for each experiment. The analysis of each group highlights specific characteristics
1278 that all the traces in the group share together: Average fluorescence trace, Average number of bursts,
1279 Burst intensity, and Duration of bursts.

1280 **Animals**

1281 Mecp2-KO mice[25] (C57BL/6 background) were obtained from Mutant Mouse Resource and Research
1282 Centers (MMRRC). They were maintained on a 12-hour light/dark cycle with free access to food and
1283 water. All aspects of animal care and treatment were carried out according to the guidelines of the
1284 Experimental Animal Care Committee of Kyushu University.

1285 **3TC and d4T *in vivo* treatments**

1286 Mecp2-KO mice were administered 2 mg/mL 3TC (QA-4615, Combi-Blocks) or d4T (D3580, TCI) in
1287 drinking water starting at 4 weeks. All mice were observed daily and weighed once per week.

1288 **Scoring of symptoms**

1289 Neurological symptoms of mice were scored as previously described[94]. In brief, mice were scored blind
1290 to genotype and treatment status, focusing on mobility, gait, hindlimb clasping, tremor, breathing, and
1291 general condition. Each of the 6 symptoms was scored from 0 to 2; 0 corresponds to the symptom being
1292 absent or the same as in the WT, 1 to the symptom being present, and 2 to the symptom being severe.

1293 **Open-field test**

1294 The open-field test was performed with 8-week-old WT, Mecp2-KO, and 3TC-treated Mecp2-KO male
1295 mice. Each mouse was placed in the corner of the open-field apparatus (50 cm × 50 cm × 30 cm), which
1296 was illuminated at 100 lux. Total distance traveled (cm) and average speed (cm/s) were calculated
1297 using the automated video tracking software TimeOFCR2 (O'Hara & Co., Tokyo, Japan). Data were
1298 collected for 10 min.

1299 **Elevated plus maze test**

1300 The elevated plus maze consisted of two opposite open arms (25 cm × 5 cm × 0.25 cm) and two
1301 enclosed arms (25 cm × 5 cm × 15 cm), illuminated at 30 lux and placed 50 cm above the floor. Each
1302 mouse was placed in the central square of the maze (5 × 5 cm), facing one of the closed arms. Mouse
1303 behavior was recorded for 10 min, and the time spent on open arm was analyzed using the automated
1304 video tracking software TimeEP1 (O'Hara & Co., Tokyo, Japan). The percentages of time spent in open
1305 arm over total time were calculated.

1306 **Three-chambers social interaction**

1307 The three-chambers apparatus is a rectangular non-transparent gray Plexiglas box (60 × 40 × 22 cm),
1308 partitioned into three equal-sized (20 × 40 × 22 cm) chambers by transparent Plexiglas plates with small
1309 openings (5 × 3 cm) allowing access into each chamber. One quarter-cylinder cage made of wire was
1310 placed in the corner of each of the side chambers. The box was illuminated at 20 lux. The subject
1311 mouse was placed into the central chamber and allowed to freely explore the three chambers for 5
1312 minutes. In the first testing section, an age-matched stranger mouse (S1) of the same strain was placed
1313 in one of the cages, and the subject mouse was allowed to explore the three chambers without
1314 restrictions for 10 min. In the second section of preference for social novelty, a second stranger mouse
1315 (S2) was placed in the opposite cage, and the subject mouse was allowed to explore again for 10
1316 minutes. All tests were video-recorded, and the time spent in the quadrant around the cage was
1317 analyzed using the automated video tracking software TimeCSI (O'Hara & Co., Tokyo, Japan). The
1318 social novelty index was calculated by the following formula: [Time spent interacting with stranger 2 in
1319 the second section] / [Time spent interacting with stranger 1+stranger 2 in the second section].

1320 **Golgi staining**

1321 Golgi staining was carried out using the FD Rapid GolgiStain Kit (FD NeuroTechnologies, Cat.# PK401)
1322 according to the manufacturer's instructions. Briefly, mice at 8-9 weeks of age were euthanized, and
1323 brains were quickly removed and rinsed in double distilled water to remove blood from the surface.
1324 Brains were immersed in impregnation solution prepared by mixing equal volumes of Solutions A and
1325 B, and stored at RT for 2 weeks in the dark. They were then transferred into Solution C and stored at
1326 RT for 1 week in the dark, subsequently embedded in TFM tissue freezing medium (General Data

1327 Healthcare, Cat.# 15-183-1) and frozen at -80°C. Brains were sectioned serially at a thickness of
1328 100 µm using a Cryostat (Leica, Cat.# CM1950). The sections were mounted on gelatin-coated glass
1329 slides and dried naturally overnight at RT. The dry-mounted sections were rinsed with double distilled
1330 water twice for 4 min. They were placed in the staining solution consisting of one part Solution D, one
1331 part Solution E, and 2 parts double distilled water for 10 min in the dark. They were further rinsed in
1332 double distilled water two times for 4 min and dehydrated in sequential rinses of 50, 75, and 95% ethanol
1333 for 4min each rinse. After further dehydration by 100% ethanol, the sections were cleaned in xylene
1334 three times for 4 min and finally coverslipped with Permount. Brightfield images of Golgi-stained
1335 neurons were acquired using a KEYENCE BZ-X700 fluorescence microscope.

1336 **Measurement of dendritic soma size *in vivo***

1337 Three mice of each group (WT, Mecp2-KO, and 3TC-treated Mecp2-KO) were examined. For images
1338 of Golgi-stained neurons, Z-series brightfield images of layer 2/3 pyramidal neurons in PFC were
1339 acquired at 20X objective using a KEYENCE BZ-X700 fluorescence microscope. To profile entire cell
1340 morphology in the Z direction, Z-series images were acquired every 1 µm. Sequential images of each
1341 field were reconstructed using the maximum intensity projection method. Soma size was quantified by
1342 tracing the outline of the cell body using ImageJ.

1343 **Measurement of dendritic spine density *in vivo***

1344 Three mice of each group (WT, Mecp2-KO, and 3TC-treated Mecp2-KO were examined. Z-series
1345 brightfield images of layer 2/3 pyramidal neurons in PFC were acquired every 0.2 µm at 100X -oil
1346 objective using KEYENCE BZ-X700 fluorescence microscope. Sequential images of each field were
1347 reconstructed using the maximum intensity projection method. The number of spines of secondary
1348 apical dendrites was manually counted, and then spine density per 10 µm was calculated.

1349 **Quantification and Statistical analysis**

1350 Error bars for figures are standard error of the mean (S.E.M.) using GraphPad Prism v6 (GraphPad
1351 Software Inc). Technical replicates were used to determine the standard error.

1352 **Publicly available RNA-seq data analysis**

1353 Publicly available RNA-seq data were obtained from the Gene Expression Omnibus (GSE159771 for
1354 spaceflight mouse retina; GSE199680 for mouse lung exposed to simulated GCR). The GCR exposure
1355 included five ion species: 1 GeV 1H (34.8%), 600 MeV/U 28Si (1.1%), 250 MeV/U 4He (18.0%), 350
1356 MeV/U 16O (5.8%), 600 MeV/U 56Fe (1.0%), and 250 MeV 1H (39.2%). Raw FASTQ files were
1357 retrieved using SRA Toolkit. Adapter trimming and quality filtering were performed using Trimmomatic
1358 and Cutadapt. Reads were aligned to the mouse T2T genome (mhaESC) using STAR-2.7.11b, and
1359 transposable elements expression was quantified using TEtranscripts, with annotations from
1360 RepeatMasker. Differential expression analysis was conducted using DESeq2, and gene set
1361 enrichment analysis was performed with GSEA (gene set database:
1362 msigdb.v2023.2.Mm.symbols.gmt).

1363 **References**

1364 1 Trujillo, C. A. *et al.* Complex Oscillatory Waves Emerging from Cortical Organoids
1365 Model Early Human Brain Network Development. *Cell stem cell* (2019).
1366 https://doi.org/10.1016/j.stem.2019.08.002
1367 2 Fitzgerald, M. Q. *et al.* Generation of 'semi-guided' cortical organoids with complex
1368 neural oscillations. *Nature protocols* **19**, 2712–2738 (2024).
1369 https://doi.org/10.1038/s41596-024-00994-0
1370 3 Corujo, D. & Buschbeck, M. Post-Translational Modifications of H2A Histone Variants
1371 and Their Role in Cancer. *Cancers (Basel)* **10** (2018).
1372 https://doi.org/10.3390/cancers10030059
1373 4 Hauer, M. H. & Gasser, S. M. Chromatin and nucleosome dynamics in DNA damage
1374 and repair. *Genes Dev* **31**, 2204–2221 (2017).
1375 https://doi.org/10.1101/gad.307702.117
1376 5 Azevedo, M. D. *et al.* Oxidative stress induced by sustained supraphysiological
1377 intrastriatal GDNF delivery is prevented by dose regulation. *Mol Ther Methods Clin*
1378 *Dev* **31**, 101106 (2023). https://doi.org/10.1016/j.omtm.2023.09.002
1379 6 Morrison, A. J. Chromatin-remodeling links metabolic signaling to gene expression.
1380 *Mol Metab* **38**, 100973 (2020). https://doi.org/10.1016/j.molmet.2020.100973
1381 7 Gross, S. R. & Kinzy, T. G. Improper organization of the actin cytoskeleton affects
1382 protein synthesis at initiation. *Mol Cell Biol* **27**, 1974–1989 (2007).
1383 https://doi.org/10.1128/MCB.00832-06
1384 8 Lai, W. F. & Wong, W. T. Roles of the actin cytoskeleton in aging and age-associated
1385 diseases. *Ageing Res Rev* **58**, 101021 (2020).
1386 https://doi.org/10.1016/j.arr.2020.101021
1387 9 Trujillo, C. A. *et al.* Pharmacological reversal of synaptic and network pathology in
1388 human MECP2-KO neurons and cortical organoids. *EMBO Mol Med* **13**, e12523
1389 (2021). https://doi.org/10.15252/emmm.202012523
1390 10 Chen, Z. *et al.* Spaceflight decelerates the epigenetic clock orchestrated with a global
1391 alteration in DNA methylome and transcriptome in the mouse retina. *Precis Clin Med*
1392 **4**, 93–108 (2021). https://doi.org/10.1093/pcmedi/pbab012
1393 11 Clement, K. *et al.* Long-term effects of combined exposures to simulated
1394 microgravity and galactic cosmic radiation on the mouse lung: sex-specific epigenetic
1395 reprogramming. *Radiat Environ Biophys* **64**, 17–27 (2025).
1396 https://doi.org/10.1007/s00411-025-01108-4
1397 12 Thomas, C. A. *et al.* Modeling of TREX1-Dependent Autoimmune Disease using
1398 Human Stem Cells Highlights L1 Accumulation as a Source of Neuroinflammation.
1399 *Cell stem cell* **21**, 319–331 e318 (2017). https://doi.org/10.1016/j.stem.2017.07.009
1400 13 Crow, M. K. Long interspersed nuclear elements (LINE-1): potential triggers of
1401 systemic autoimmune disease. *Autoimmunity* **43**, 7–16 (2010).
1402 https://doi.org/10.3109/08916930903374865
1403 14 Muotri, A. R. *et al.* L1 retrotransposition in neurons is modulated by MeCP2. *Nature*
1404 **468**, 443–446 (2010). https://doi.org/10.1038/nature09544
1405 15 Yu, F., Zingler, N., Schumann, G. & Stratling, W. H. Methyl-CpG-binding protein 2
1406 represses LINE-1 expression and retrotransposition but not Alu transcription. *Nucleic*
1407 *Acids Res* **29**, 4493–4501 (2001). https://doi.org/10.1093/nar/29.21.4493

1408 16 Zhao, B. *et al.* Somatic LINE-1 retrotransposition in cortical neurons and non-brain
1409 tissues of Rett patients and healthy individuals. *PLoS genetics* **15**, e1008043 (2019).
1410 https://doi.org/10.1371/journal.pgen.1008043
1411 17 Loo, L. *et al.* Fibroblast-expressed LRRC15 is a receptor for SARS-CoV-2 spike and
1412 controls antiviral and antifibrotic transcriptional programs. *PLoS Biol* **21**, e3001967
1413 (2023). https://doi.org/10.1371/journal.pbio.3001967
1414 18 Deverman, B. E. & Patterson, P. H. Cytokines and CNS development. *Neuron* **64**, 61–
1415 78 (2009). https://doi.org/10.1016/j.neuron.2009.09.002
1416 19 Moretti, P. & Zoghbi, H. Y. MeCP2 dysfunction in Rett syndrome and related
1417 disorders. *Curr Opin Genet Dev* **16**, 276–281 (2006).
1418 https://doi.org/10.1016/j.gde.2006.04.009
1419 20 Masarapu, Y. *et al.* Spatially resolved multiomics on the neuronal effects induced by
1420 spaceflight in mice. *Nat Commun* **15**, 4778 (2024). https://doi.org/10.1038/s41467-
1421 024-48916-8
1422 21 Albizzati, E. *et al.* Mecp2 knock-out astrocytes affect synaptogenesis by interleukin 6
1423 dependent mechanisms. *iScience* **27**, 109296 (2024).
1424 https://doi.org/10.1016/j.isci.2024.109296
1425 22 Lappalainen, R. & Riikonen, R. S. High levels of cerebrospinal fluid glutamate in Rett
1426 syndrome. *Pediatr Neurol* **15**, 213–216 (1996). https://doi.org/10.1016/s0887-
1427 8994(96)00218-4
1428 23 Okabe, Y. *et al.* Alterations of gene expression and glutamate clearance in astrocytes
1429 derived from an MeCP2-null mouse model of Rett syndrome. *PLoS One* **7**, e35354
1430 (2012). https://doi.org/10.1371/journal.pone.0035354
1431 24 Pan, J. W., Lane, J. B., Hetherington, H. & Percy, A. K. Rett syndrome: 1H
1432 spectroscopic imaging at 4.1 Tesla. *J Child Neurol* **14**, 524–528 (1999).
1433 https://doi.org/10.1177/088307389901400808
1434 25 Chen, R. Z., Akbarian, S., Tudor, M. & Jaenisch, R. Deficiency of methyl-CpG binding
1435 protein-2 in CNS neurons results in a Rett-like phenotype in mice. *Nat Genet* **27**,
1436 327–331 (2001). https://doi.org/10.1038/85906
1437 26 De Cecco, M. *et al.* L1 drives IFN in senescent cells and promotes age-associated
1438 inflammation. *Nature* **566**, 73–78 (2019). https://doi.org/10.1038/s41586-018-0784-
1439 9
1440 27 Pelka, G. J. *et al.* Mecp2 deficiency is associated with learning and cognitive deficits
1441 and altered gene activity in the hippocampal region of mice. *Brain* **129**, 887–898
1442 (2006). https://doi.org/10.1093/brain/awl022
1443 28 Pitcher, M. R. *et al.* Insulinotropic treatments exacerbate metabolic syndrome in
1444 mice lacking MeCP2 function. *Human Molecular Genetics* **22**, 2626–2633 (2013).
1445 https://doi.org/10.1093/hmg/ddt111
1446 29 Samaco, R. C. *et al.* Female Mecp2(+/-) mice display robust behavioral deficits on
1447 two different genetic backgrounds providing a framework for pre-clinical studies.
1448 *Hum Mol Genet* **22**, 96–109 (2013). https://doi.org/10.1093/hmg/dds406
1449 30 Ward, C. S. *et al.* MeCP2 Is Critical within HoxB1-Derived Tissues of Mice for Normal
1450 Lifespan. *Journal of Neuroscience* **31**, 10359–10370 (2011).
1451 https://doi.org/10.1523/jneurosci.0057-11.2011
1452 31 Wu, Y. *et al.* Characterization of Rett Syndrome-like phenotypes in Mecp2-knockout
1453 rats. *J Neurodev Disord* **8**, 23 (2016). https://doi.org/10.1186/s11689-016-9156-7

1454 32 Bai, D. *et al.* ALDOA maintains NLRP3 inflammasome activation by controlling AMPK
1455 activation. *Autophagy* **18**, 1673–1693 (2022).
1456 https://doi.org/10.1080/15548627.2021.1997051
1457 33 Castro, J. *et al.* Functional recovery with recombinant human IGF1 treatment in a
1458 mouse model of Rett Syndrome. *Proc Natl Acad Sci U S A* **111**, 9941–9946 (2014).
1459 https://doi.org/10.1073/pnas.1311685111
1460 34 Lilley, C. E., Chaurushiya, M. S. & Weitzman, M. D. Chromatin at the intersection of
1461 viral infection and DNA damage. *Biochimica et Biophysica Acta (BBA) - Gene*
1462 *Regulatory Mechanisms* **1799**, 319–327 (2010).
1463 https://doi.org/10.1016/j.bbagrm.2009.06.007
1464 35 Nehme, Z., Pasquereau, S. & Herbein, G. in *Histone Modifications in Therapy* Vol. 20
1465 (eds Pedro Castelo-Branco & Carmen Jeronimo) 255–292 (Academic Press, 2020).
1466 36 Vuu, Y. M., Roberts, C.-T. & Rastegar, M. MeCP2 Is an Epigenetic Factor That Links
1467 DNA Methylation with Brain Metabolism. *International Journal of Molecular Sciences*
1468 **24**, 4218 (2023). https://doi.org/10.3390/ijms24044218
1469 37 You, E. *et al.* LINE-1 ORF1p Mimics Viral Innate Immune Evasion Mechanisms in
1470 Pancreatic Ductal Adenocarcinoma. *Cancer Discovery* **15**, 1063–1082 (2025).
1471 https://doi.org/10.1158/2159-8290.cd-24-1317
1472 38 Zhang, X., Zhang, R. & Yu, J. New Understanding of the Relevant Role of LINE-1
1473 Retrotransposition in Human Disease and Immune Modulation. *Front Cell Dev Biol* **8**
1474 (2020). https://doi.org/10.3389/fcell.2020.00657
1475 39 Evans, T. A. & Erwin, J. A. Retroelement-derived RNA and its role in the brain. *Semin*
1476 *Cell Dev Biol* **114**, 68–80 (2021). https://doi.org/10.1016/j.semcdb.2020.11.001
1477 40 Jones, R. B. *et al.* Nucleoside analogue reverse transcriptase inhibitors differentially
1478 inhibit human LINE-1 retrotransposition. *PLoS One* **3**, e1547 (2008).
1479 https://doi.org/10.1371/journal.pone.0001547
1480 41 Dai, L., Huang, Q. & Boeke, J. D. Effect of reverse transcriptase inhibitors on LINE-1
1481 and Ty1 reverse transcriptase activities and on LINE-1 retrotransposition. *BMC*
1482 *Biochem* **12**, 18 (2011). https://doi.org/10.1186/1471-2091-12-18
1483 42 Pitcher, M. R. *et al.* Insulinotropic treatments exacerbate metabolic syndrome in
1484 mice lacking MeCP2 function. *Hum Mol Genet* **22**, 2626–2633 (2013).
1485 https://doi.org/10.1093/hmg/ddt111
1486 43 Sobanski, T. *et al.* The fructose-bisphosphate, Aldolase A (ALDOA), facilitates DNA-
1487 PKcs and ATM kinase activity to regulate DNA double-strand break repair. *Sci Rep* **13**,
1488 15171 (2023). https://doi.org/10.1038/s41598-023-41133-1
1489 44 Bogerd, H. P. *et al.* Cellular inhibitors of long interspersed element 1 and Alu
1490 retrotransposition. *Proc Natl Acad Sci U S A* **103**, 8780–8785 (2006).
1491 https://doi.org/10.1073/pnas.0603313103
1492 45 Tam, O. H., Ostrow, L. W. & Gale Hammell, M. Diseases of the nERVous system:
1493 retrotransposon activity in neurodegenerative disease. *Mob DNA* **10**, 32 (2019).
1494 https://doi.org/10.1186/s13100-019-0176-1
1495 46 Roy, N. *et al.* Elevated expression of the retrotransposon LINE-1 drives Alzheimer's
1496 disease-associated microglial dysfunction. *Acta Neuropathol* **148**, 75 (2024).
1497 https://doi.org/10.1007/s00401-024-02835-6
1498 47 Zhang, W. *et al.* Retrotransposon: an insight into neurological disorders from
1499 perspectives of neurodevelopment and aging. *Transl Neurodegener* **14**, 14 (2025).
1500 https://doi.org/10.1186/s40035-025-00471-y

1501 48 Peze-Heidsieck, E. *et al.* Retrotransposons as a Source of DNA Damage in
1502 Neurodegeneration. *Front Aging Neurosci* **13**, 786897 (2021).
1503 https://doi.org/10.3389/fnagi.2021.786897
1504 49 Ravel-Godreuil, C., Znaidi, R., Bonnifet, T., Joshi, R. L. & Fuchs, J. Transposable
1505 elements as new players in neurodegenerative diseases. *FEBS Lett* **595**, 2733–2755
1506 (2021). https://doi.org/10.1002/1873-3468.14205
1507 50 Reid, M. A., Dai, Z. & Locasale, J. W. The impact of cellular metabolism on chromatin
1508 dynamics and epigenetics. *Nat Cell Biol* **19**, 1298–1306 (2017).
1509 https://doi.org/10.1038/ncb3629
1510 51 Xu, Q. *et al.* SETD2 regulates the maternal epigenome, genomic imprinting and
1511 embryonic development. *Nat Genet* **51**, 844–856 (2019).
1512 https://doi.org/10.1038/s41588-019-0398-7
1513 52 Jachowicz, J. W. *et al.* LINE-1 activation after fertilization regulates global chromatin
1514 accessibility in the early mouse embryo. *Nat Genet* **49**, 1502–1510 (2017).
1515 https://doi.org/10.1038/ng.3945
1516 53 Terry, D. M. & Devine, S. E. Aberrantly High Levels of Somatic LINE-1 Expression and
1517 Retrotransposition in Human Neurological Disorders. *Front Genet* **10**, 1244 (2019).
1518 https://doi.org/10.3389/fgene.2019.01244
1519 54 Garrett-Bakelman, F. E. *et al.* The NASA Twins Study: A multidimensional analysis of a
1520 year-long human spaceflight. *Science* **364** (2019).
1521 https://doi.org/10.1126/science.aau8650
1522 55 Indo, H. P. *et al.* Changes in mitochondrial homeostasis and redox status in
1523 astronauts following long stays in space. *Sci Rep* **6**, 39015 (2016).
1524 https://doi.org/10.1038/srep39015
1525 56 Waisberg, E. *et al.* Mitochondrial dysfunction in Spaceflight Associated Neuro-Ocular
1526 Syndrome (SANS): a molecular hypothesis in pathogenesis. *Eye (Lond)* **38**, 1409–1411
1527 (2024). https://doi.org/10.1038/s41433-024-02951-3
1528 57 da Silveira, W. A. *et al.* Comprehensive Multi-omics Analysis Reveals Mitochondrial
1529 Stress as a Central Biological Hub for Spaceflight Impact. *Cell* **183**, 1185–1201 e1120
1530 (2020). https://doi.org/10.1016/j.cell.2020.11.002
1531 58 Hroudova, J., Singh, N. & Fisar, Z. Mitochondrial dysfunctions in neurodegenerative
1532 diseases: relevance to Alzheimer's disease. *Biomed Res Int* **2014**, 175062 (2014).
1533 https://doi.org/10.1155/2014/175062
1534 59 Area-Gomez, E., Guardia-Laguarta, C., Schon, E. A. & Przedborski, S. Mitochondria,
1535 OxPhos, and neurodegeneration: cells are not just running out of gas. *J Clin Invest*
1536 **129**, 34–45 (2019). https://doi.org/10.1172/JCI120848
1537 60 Jones, C. W. *et al.* Molecular and physiological changes in the SpaceX Inspiration4
1538 civilian crew. *Nature* **632**, 1155–1164 (2024). https://doi.org/10.1038/s41586-024-
1539 07648-x
1540 61 Ali, N., Beheshti, A. & Hampikian, G. Space exploration and risk of Parkinson's
1541 disease: a perspective review. *NPJ Microgravity* **11**, 1 (2025).
1542 https://doi.org/10.1038/s41526-024-00457-6
1543 62 Pecorelli, A., Cervellati, C., Cordone, V., Hayek, J. & Valacchi, G. Compromised
1544 immune/inflammatory responses in Rett syndrome. *Free Radic Biol Med* **152**, 100–
1545 106 (2020). https://doi.org/10.1016/j.freeradbiomed.2020.02.023

1546 63 Pecorelli, A. *et al.* Altered inflammasome machinery as a key player in the
1547 perpetuation of Rett syndrome oxinflammation. *Redox Biol* **28**, 101334 (2020).
1548 https://doi.org/10.1016/j.redox.2019.101334
1549 64 Frost, B. & Dubnau, J. The Role of Retrotransposons and Endogenous Retroviruses in
1550 Age-Dependent Neurodegenerative Disorders. *Annu Rev Neurosci* **47**, 123–143
1551 (2024). https://doi.org/10.1146/annurev-neuro-082823-020615
1552 65 Mangoni, D. *et al.* From the genome's perspective: Bearing somatic
1553 retrotransposition to leverage the regulatory potential of L1 RNAs. *Bioessays* **47**,
1554 e2400125 (2025). https://doi.org/10.1002/bies.202400125
1555 66 McEntee, C. M. & LaRocca, T. J. Single-Cell Transcriptome Patterns of Transposable
1556 Elements in Alzheimer's Disease. *Mol Neurobiol* (2025).
1557 https://doi.org/10.1007/s12035-025-05140-9
1558 67 LaRocca, T. J., Cavalier, A. N. & Wahl, D. Repetitive elements as a transcriptomic
1559 marker of aging: Evidence in multiple datasets and models. *Aging Cell* **19**, e13167
1560 (2020). https://doi.org/10.1111/acel.13167
1561 68 Baune, B. T. *et al.* Interleukin-6 gene (IL-6): a possible role in brain morphology in the
1562 healthy adult brain. *J Neuroinflammation* **9**, 125 (2012).
1563 https://doi.org/10.1186/1742-2094-9-125
1564 69 Zhao, Z. *et al.* Plasma IL-6 levels and their association with brain health and dementia
1565 risk: A population-based cohort study. *Brain Behav Immun* **120**, 430–438 (2024).
1566 https://doi.org/10.1016/j.bbi.2024.06.014
1567 70 Camera, A. *et al.* Aging and putative frailty biomarkers are altered by spaceflight. *Sci*
1568 *Rep* **14**, 13098 (2024). https://doi.org/10.1038/s41598-024-57948-5
1569 71 Mao, W. *et al.* Microgravity Inhibits Cell Proliferation and Promotes Senescence and
1570 Apoptosis in Embryonic Stem Cells. *Space: Science & Technology* **4** (2024).
1571 https://doi.org/10.34133/space.0104
1572 72 Pham, T. P., Kremer, V. & Boon, R. A. RNA-based therapeutics in cardiovascular
1573 disease. *Curr Opin Cardiol* **35**, 191–198 (2020).
1574 https://doi.org/10.1097/HCO.0000000000000724
1575 73 Desai, R. I. *et al.* Complex 33-beam simulated galactic cosmic radiation exposure
1576 impacts cognitive function and prefrontal cortex neurotransmitter networks in male
1577 mice. *Nat Commun* **14**, 7779 (2023). https://doi.org/10.1038/s41467-023-42173-x
1578 74 Oyefeso, F. A. *et al.* Effects of acute low-moderate dose ionizing radiation to human
1579 brain organoids. *PLoS One* **18**, e0282958 (2023).
1580 https://doi.org/10.1371/journal.pone.0282958
1581 75 Chen, Q., Sun, L. & Chen, Z. J. Regulation and function of the cGAS–STING pathway of
1582 cytosolic DNA sensing. *Nature Immunology* **17**, 1142–1149 (2016).
1583 https://doi.org/10.1038/ni.3558
1584 76 Zhen, Z. *et al.* Nuclear cGAS restricts L1 retrotransposition by promoting TRIM41-
1585 mediated ORF2p ubiquitination and degradation. *Nature Communications* **14** (2023).
1586 https://doi.org/10.1038/s41467-023-43001-y
1587 77 Gulen, M. F. *et al.* cGAS–STING drives ageing-related inflammation and
1588 neurodegeneration. *Nature* **620**, 374–380 (2023). https://doi.org/10.1038/s41586-
1589 023-06373-1
1590 78 Dvorkin, S., Cambier, S., Volkman, H. E. & Stetson, D. B. New frontiers in the cGAS-
1591 STING intracellular DNA-sensing pathway. *Immunity* **57**, 718–730 (2024).
1592 https://doi.org/10.1016/j.immuni.2024.02.019

1593 79 Colombo, A. R., Elias, H. K. & Ramsingh, G. Senescence induction universally activates
1594 transposable element expression. *Cell cycle (Georgetown, Tex* **17**, 1846–1857 (2018).
1595 https://doi.org/10.1080/15384101.2018.1502576
1596 80 Merenciano, M., Larue, A., Garambois, C., Nunes, W. V. B. & Vieira, C. Exploring the
1597 Relationship of Transposable Elements and Ageing: Causes and Consequences.
1598 *Genome Biol Evol* **17** (2025). https://doi.org/10.1093/gbe/evaf088
1599 81 Crucian, B. E. *et al.* Countermeasures-based Improvements in Stress, Immune System
1600 Dysregulation and Latent Herpesvirus Reactivation onboard the International Space
1601 Station - Relevance for Deep Space Missions and Terrestrial Medicine. *Neurosci*
1602 *Biobehav Rev* **115**, 68–76 (2020). https://doi.org/10.1016/j.neubiorev.2020.05.007
1603 82 Crucian, B. *et al.* Terrestrial stress analogs for spaceflight associated immune system
1604 dysregulation. *Brain Behav Immun* **39**, 23–32 (2014).
1605 https://doi.org/10.1016/j.bbi.2014.01.011
1606 83 Stowe, R. P., Sams, C. F. & Pierson, D. L. Adrenocortical and immune responses
1607 following short- and long-duration spaceflight. *Aviat Space Environ Med* **82**, 627–634
1608 (2011). https://doi.org/10.3357/asem.2980.2011
1609 84 Mehta, S. K. *et al.* Latent virus reactivation in astronauts on the international space
1610 station. *NPJ Microgravity* **3**, 11 (2017). https://doi.org/10.1038/s41526-017-0015-y
1611 85 McGregor, H. R. *et al.* Impacts of spaceflight experience on human brain structure.
1612 *Sci Rep* **13**, 7878 (2023). https://doi.org/10.1038/s41598-023-33331-8
1613 86 Zhang, Z. N. *et al.* Layered hydrogels accelerate iPSC-derived neuronal maturation
1614 and reveal migration defects caused by MeCP2 dysfunction. *Proc Natl Acad Sci U S A*
1615 **113**, 3185–3190 (2016). https://doi.org/10.1073/pnas.1521255113
1616 87 Marchetto, M. C. *et al.* A model for neural development and treatment of Rett
1617 syndrome using human induced pluripotent stem cells. *Cell* **143**, 527–539 (2010).
1618 https://doi.org/10.1016/j.cell.2010.10.016
1619 88 Serio, A. *et al.* Astrocyte pathology and the absence of non-cell autonomy in an
1620 induced pluripotent stem cell model of TDP-43 proteinopathy. *Proc Natl Acad Sci U S*
1621 *A* **110**, 4697–4702 (2013). https://doi.org/10.1073/pnas.1300398110
1622 89 Wickham, H. *Ggplot2 : elegant graphics for data analysis*. (Springer, 2009).
1623 90 Shannon, P. *et al.* Cytoscape: a software environment for integrated models of
1624 biomolecular interaction networks. *Genome Res* **13**, 2498–2504 (2003).
1625 https://doi.org/10.1101/gr.1239303
1626 91 Szklarczyk, D. *et al.* The STRING database in 2023: protein-protein association
1627 networks and functional enrichment analyses for any sequenced genome of interest.
1628 *Nucleic Acids Res* **51**, D638–D646 (2023). https://doi.org/10.1093/nar/gkac1000
1629 92 Assarsson, E. *et al.* Homogenous 96-plex PEA immunoassay exhibiting high
1630 sensitivity, specificity, and excellent scalability. *PLoS One* **9**, e95192 (2014).
1631 https://doi.org/10.1371/journal.pone.0095192
1632 93 Nageshappa, S. *et al.* Altered neuronal network and rescue in a human MECP2
1633 duplication model. *Mol Psychiatry* **21**, 178–188 (2016).
1634 https://doi.org/10.1038/mp.2015.128
1635 94 Guy, J., Hendrich, B., Holmes, M., Martin, J. E. & Bird, A. A mouse Mecp2-null
1636 mutation causes neurological symptoms that mimic Rett syndrome. *Nat Genet* **27**,
1637 322–326 (2001). https://doi.org/10.1038/85899
1638

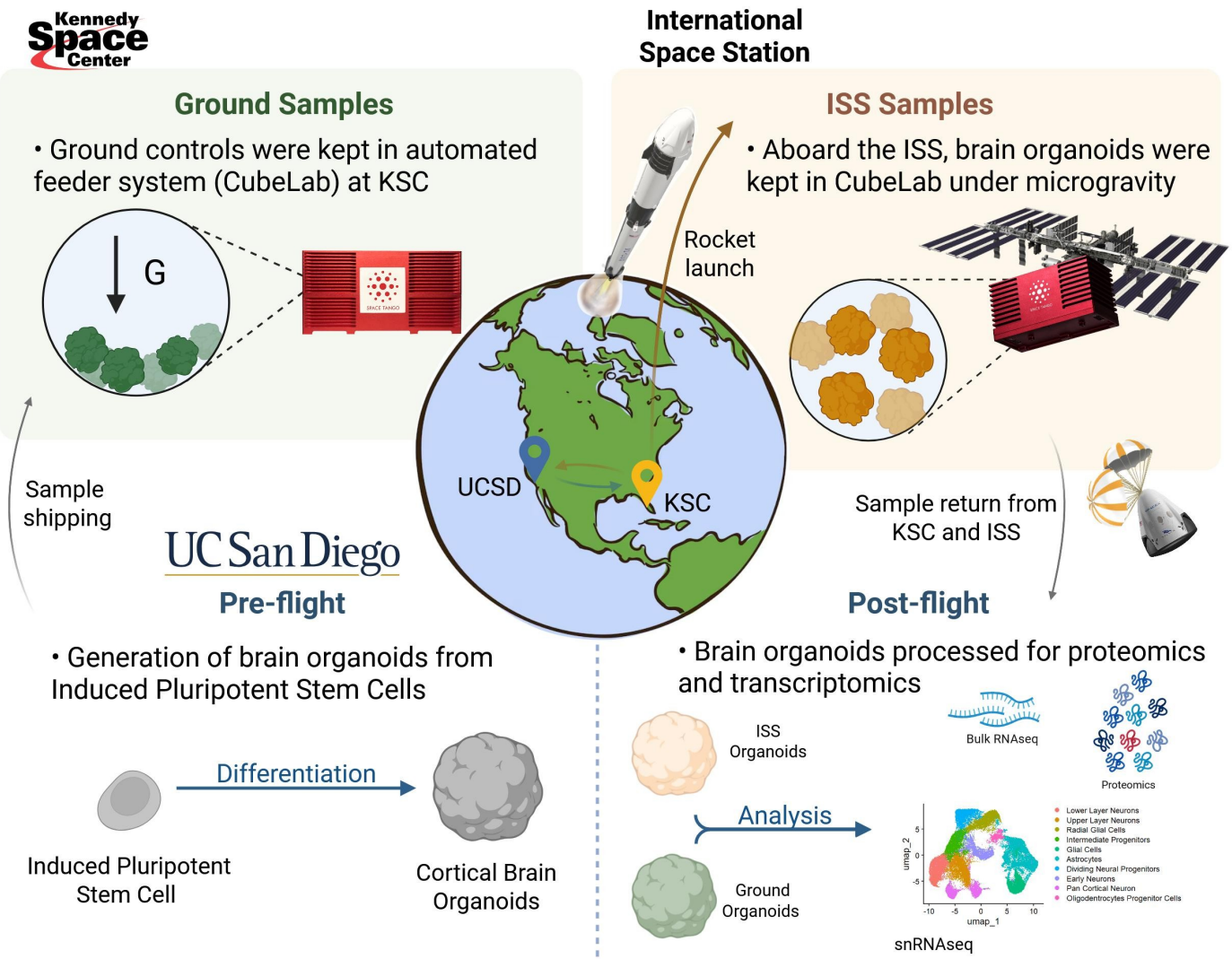
Kennedy Space Center
International Space Station
Ground Samples
• Ground controls were kept in automated feeder system (CubeLab) at KSC
G
ISS Samples
• Aboard the ISS, brain organoids were kept in CubeLab under microgravity
Rocket launch
UCSD
KSC
Sample shipping
Sample return from KSC and ISS
UC San Diego
Pre-flight
Post-flight
• Generation of brain organoids from Induced Pluripotent Stem Cells
• Brain organoids processed for proteomics and transcriptomics
Differentiation
Induced Pluripotent Stem Cell
Cortical Brain Organoids
ISS Organoids
Bulk RNAseq
Proteomics
Analysis
Ground Organoids
snRNAseq
Lower Layer Neurons
Upper Layer Neurons
Radial Glial Cells
Intermediate Progenitors
Glial Cells
Astrocytes
Dividing Neural Progenitors
Early Neurons
Pan Cortical Neuron
Oligodentrocytes Progenitor Cells
umap_1
umap_2

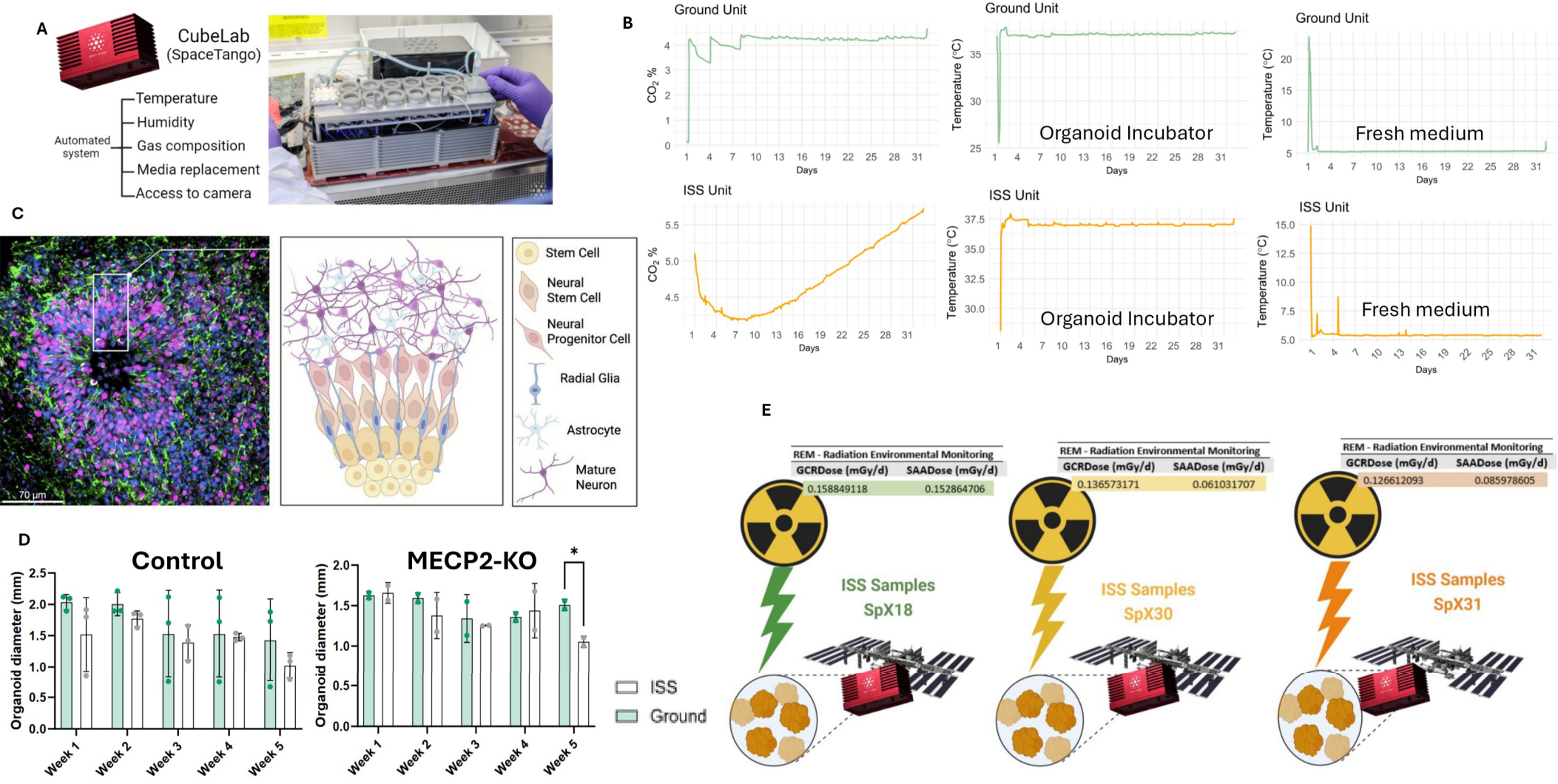
A
CubeLab
(SpaceTango)
Automated system
Temperature
Humidity
Gas composition
Media replacement
Access to camera
B
Ground Unit
ISS Unit
CO_2 %
Temperature (°C)
Days
Organoid Incubator
Fresh medium
C
70 µm
Stem Cell
Neural Stem Cell
Neural Progenitor Cell
Radial Glia
Astrocyte
Mature Neuron
D
Control
MECP2-KO
Organoid diameter (mm)
Week 1
Week 2
Week 3
Week 4
Week 5
ISS
Ground
E
REM - Radiation Environmental Monitoring
GCRDose (mGy/d)
SAADose (mGy/d)
0.158849118
0.152864706
0.136573171
0.061031707
0.126612093
0.085978605
ISS Samples SpX18
ISS Samples SpX30
ISS Samples SpX31

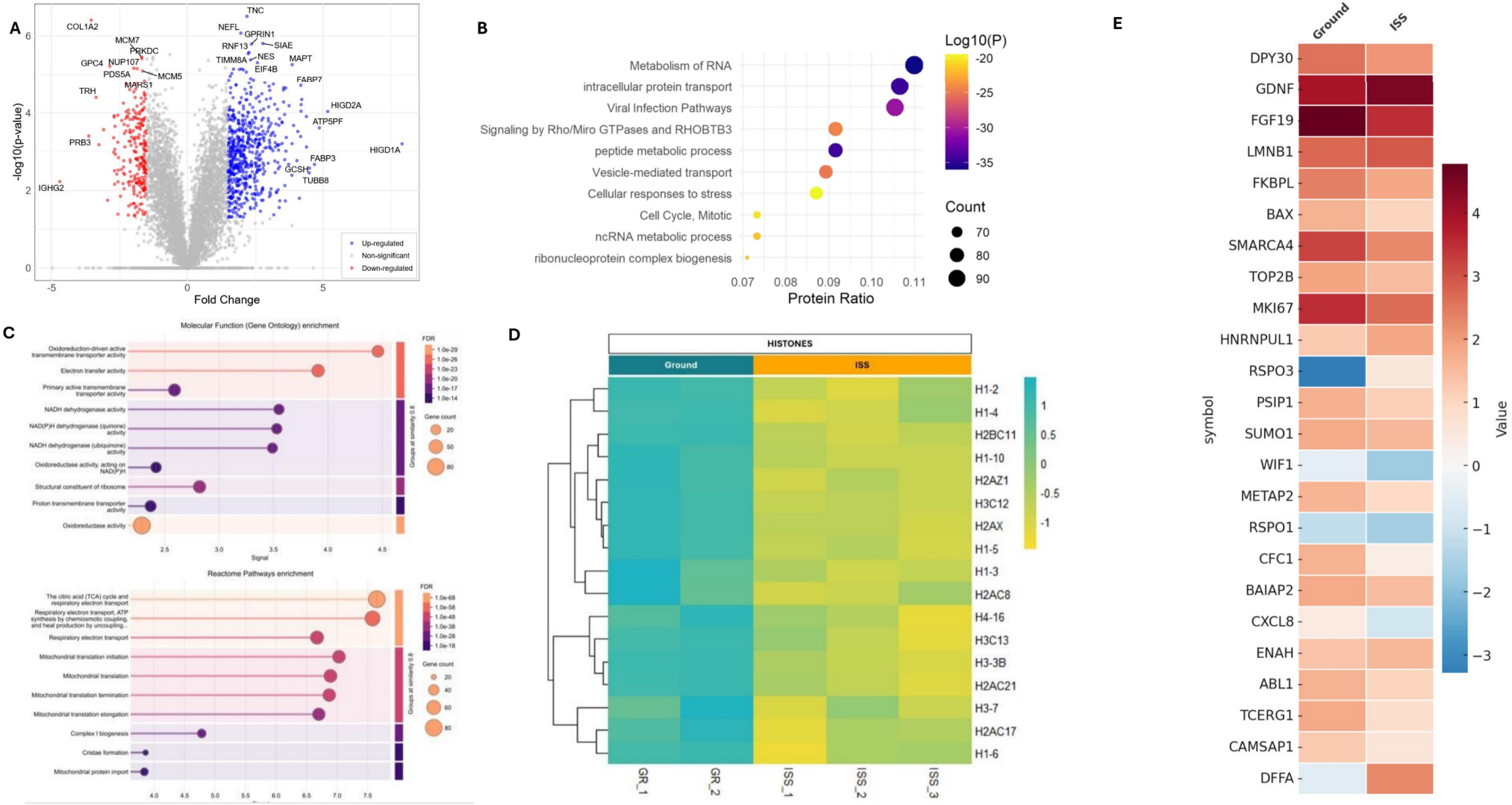
A
-log10(p-value)
Fold Change
TNC
COL1A2
NEFL
GPRIN1
MCM7
PRKDC
RNF13
SIAE
GPC4
NUP107
NES
TIMM8A
MAPT
PDS5A
MCM5
EIF4B
MARS1
FABP7
TRH
HIGD2A
ATP5PF
PRB3
HIGD1A
FABP3
GCSH
TUBB8
IGHG2
Up-regulated
Non-significant
Down-regulated
B
Log10(P)
Metabolism of RNA
intracellular protein transport
Viral Infection Pathways
Signaling by Rho/Miro GTPases and RHOBTB3
peptide metabolic process
Vesicle-mediated transport
Cellular responses to stress
Cell Cycle, Mitotic
ncRNA metabolic process
ribonucleoprotein complex biogenesis
Count
Protein Ratio
C
Molecular Function (Gene Ontology) enrichment
Oxidoreduction-driven active transmembrane transporter activity
Electron transfer activity
Primary active transmembrane transporter activity
NADH dehydrogenase activity
NAD(P)H dehydrogenase (quinone) activity
NADH dehydrogenase (ubiquinone) activity
Oxidoreductase activity, acting on NAD(P)H
Structural constituent of ribosome
Proton transmembrane transporter activity
Oxidoreductase activity
FDR
Gene count
Signal
Reactome Pathways enrichment
The citric acid (TCA) cycle and respiratory electron transport
Respiratory electron transport, ATP synthesis by chemiosmotic coupling, and heat production by uncoupling...
Respiratory electron transport
Mitochondrial translation initiation
Mitochondrial translation
Mitochondrial translation termination
Mitochondrial translation elongation
Complex I biogenesis
Cristae formation
Mitochondrial protein import
D
HISTONES
Ground
ISS
H1-2
H1-4
H2BC11
H1-10
H2AZ1
H3C12
H2AX
H1-5
H1-3
H2AC8
H4-16
H3C13
H3-3B
H2AC21
H3-7
H2AC17
H1-6
GR_1
GR_2
ISS_1
ISS_2
ISS_3
E
Ground
ISS
DPY30
GDNF
FGF19
LMNB1
FKBPL
BAX
SMARCA4
TOP2B
MKI67
HNRNPUL1
RSPO3
PSIP1
SUMO1
WIF1
METAP2
RSPO1
CFC1
BAIAP2
CXCL8
ENAH
ABL1
TCERG1
CAMSAP1
DFFA
symbol
Value

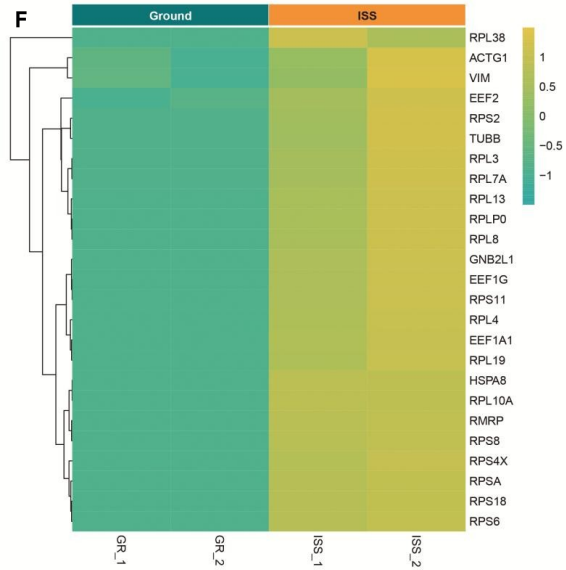
F
Ground
ISS
RPL38
ACTG1
VIM
EEF2
RPS2
TUBB
RPL3
RPL7A
RPL13
RPLP0
RPL8
GNB2L1
EEF1G
RPS11
RPL4
EEF1A1
RPL19
HSPA8
RPL10A
RMRP
RPS8
RPS4X
RPSA
RPS18
RPS6
GR_1
GR_2
ISS_1
ISS_2
1
0.5
0
−0.5
−1

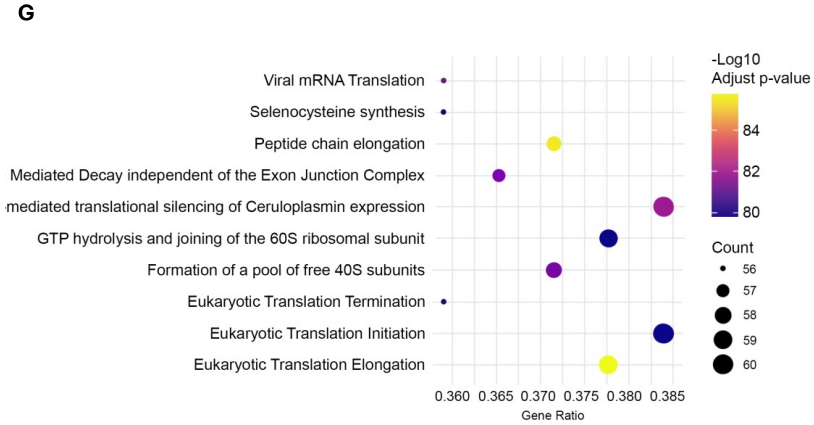
G
Viral mRNA Translation
Selenocysteine synthesis
Peptide chain elongation
Mediated Decay independent of the Exon Junction Complex
mediated translational silencing of Ceruloplasmin expression
GTP hydrolysis and joining of the 60S ribosomal subunit
Formation of a pool of free 40S subunits
Eukaryotic Translation Termination
Eukaryotic Translation Initiation
Eukaryotic Translation Elongation
0.360 0.365 0.370 0.375 0.380 0.385
Gene Ratio
-Log10
Adjust p-value
84
82
80
Count
56
57
58
59
60

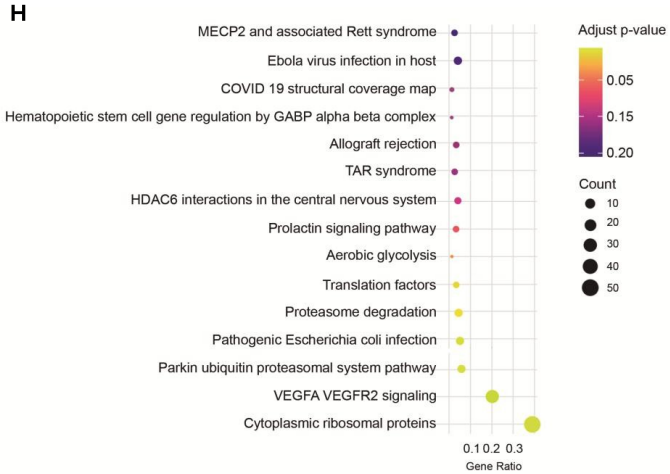
H
MECP2 and associated Rett syndrome
Ebola virus infection in host
COVID 19 structural coverage map
Hematopoietic stem cell gene regulation by GABP alpha beta complex
Allograft rejection
TAR syndrome
HDAC6 interactions in the central nervous system
Prolactin signaling pathway
Aerobic glycolysis
Translation factors
Proteasome degradation
Pathogenic Escherichia coli infection
Parkin ubiquitin proteasomal system pathway
VEGFA VEGFR2 signaling
Cytoplasmic ribosomal proteins
0.1 0.2 0.3
Gene Ratio
Adjust p-value
0.05
0.15
0.20
Count
10
20
30
40
50

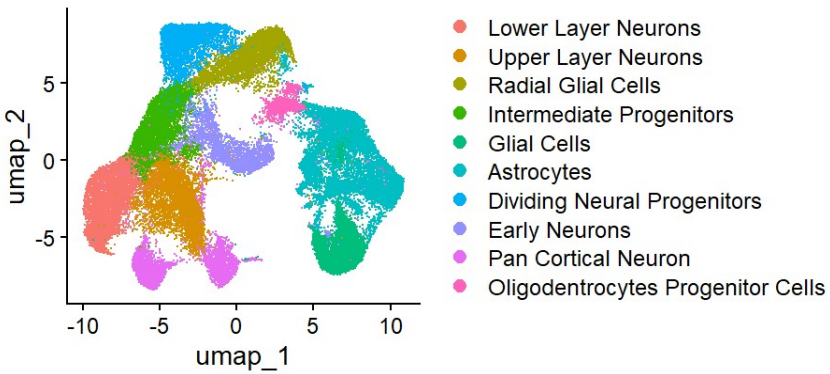
umap_2
umap_1
5
0
-5
-10
-5
0
5
10
Lower Layer Neurons
Upper Layer Neurons
Radial Glial Cells
Intermediate Progenitors
Glial Cells
Astrocytes
Dividing Neural Progenitors
Early Neurons
Pan Cortical Neuron
Oligodentrocytes Progenitor Cells

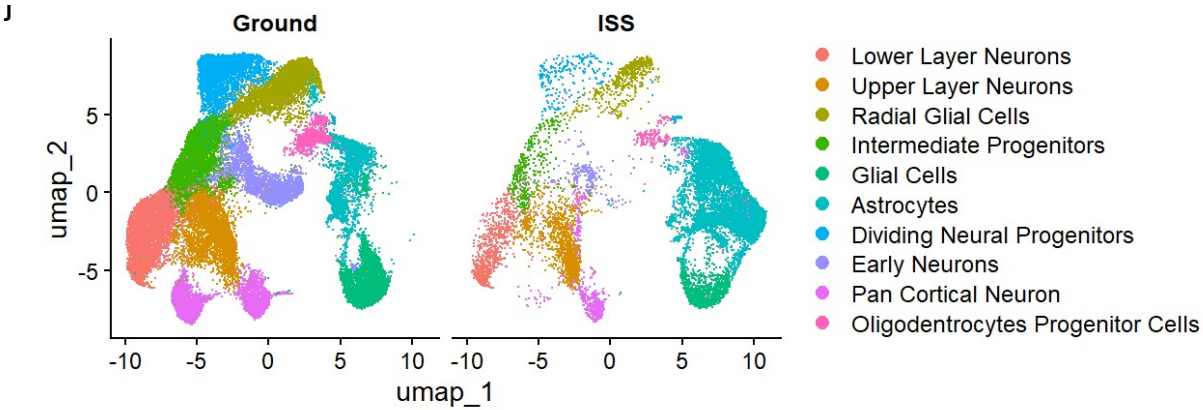
J
Ground
ISS
umap_2
umap_1
5
0
-5
-10
-5
0
5
10
Lower Layer Neurons
Upper Layer Neurons
Radial Glial Cells
Intermediate Progenitors
Glial Cells
Astrocytes
Dividing Neural Progenitors
Early Neurons
Pan Cortical Neuron
Oligodentrocytes Progenitor Cells

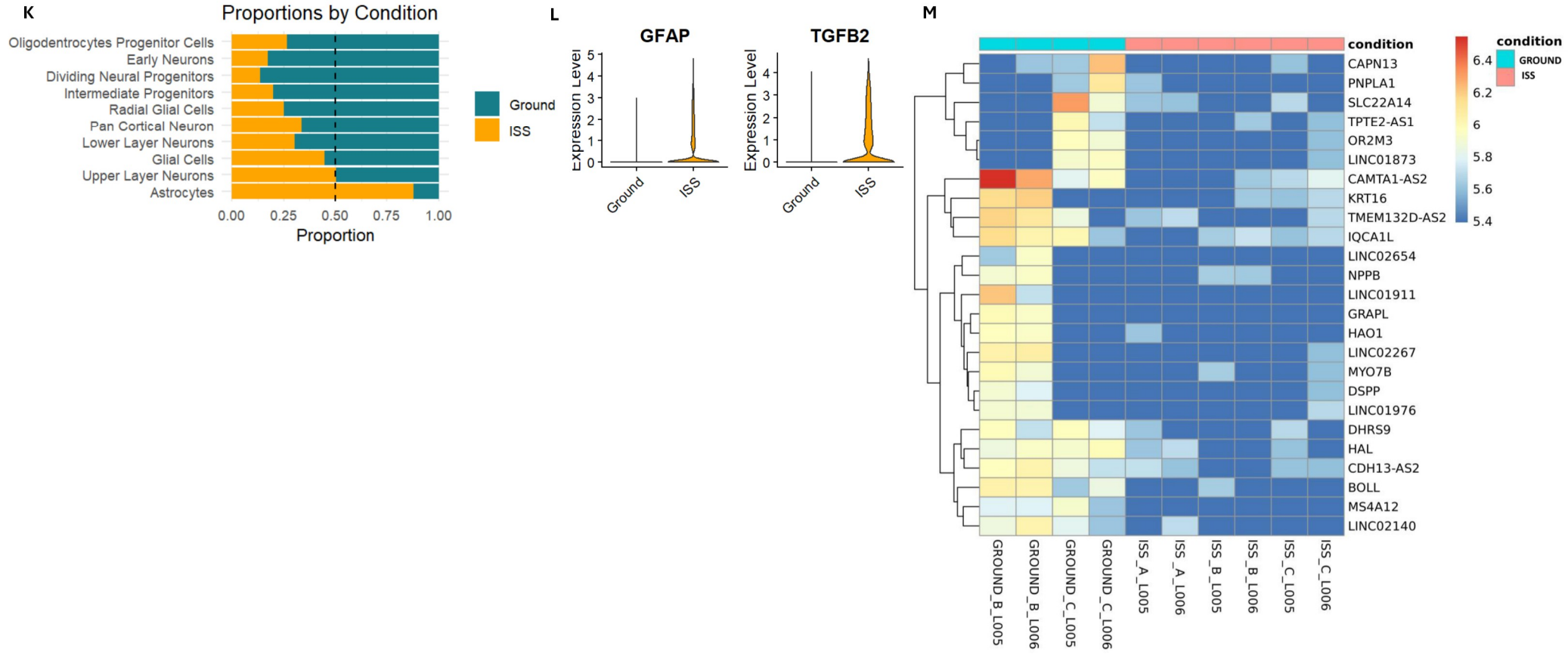
K
Proportions by Condition
Oligodentrocytes Progenitor Cells
Early Neurons
Dividing Neural Progenitors
Intermediate Progenitors
Radial Glial Cells
Pan Cortical Neuron
Lower Layer Neurons
Glial Cells
Upper Layer Neurons
Astrocytes
0.00
0.25
0.50
0.75
1.00
Proportion
Ground
ISS
L
GFAP
TGFB2
Expression Level
Ground
ISS
M
condition
GROUND
ISS
CAPN13
PNPLA1
SLC22A14
TPTE2-AS1
OR2M3
LINC01873
CAMTA1-AS2
KRT16
TMEM132D-AS2
IQCA1L
LINC02654
NPPB
LINC01911
GRAPL
HAO1
LINC02267
MYO7B
DSPP
LINC01976
DHRS9
HAL
CDH13-AS2
BOLL
MS4A12
LINC02140
GROUND_B_L005
GROUND_B_L006
GROUND_C_L005
GROUND_C_L006
ISS_A_L005
ISS_A_L006
ISS_B_L005
ISS_B_L006
ISS_C_L005
ISS_C_L006

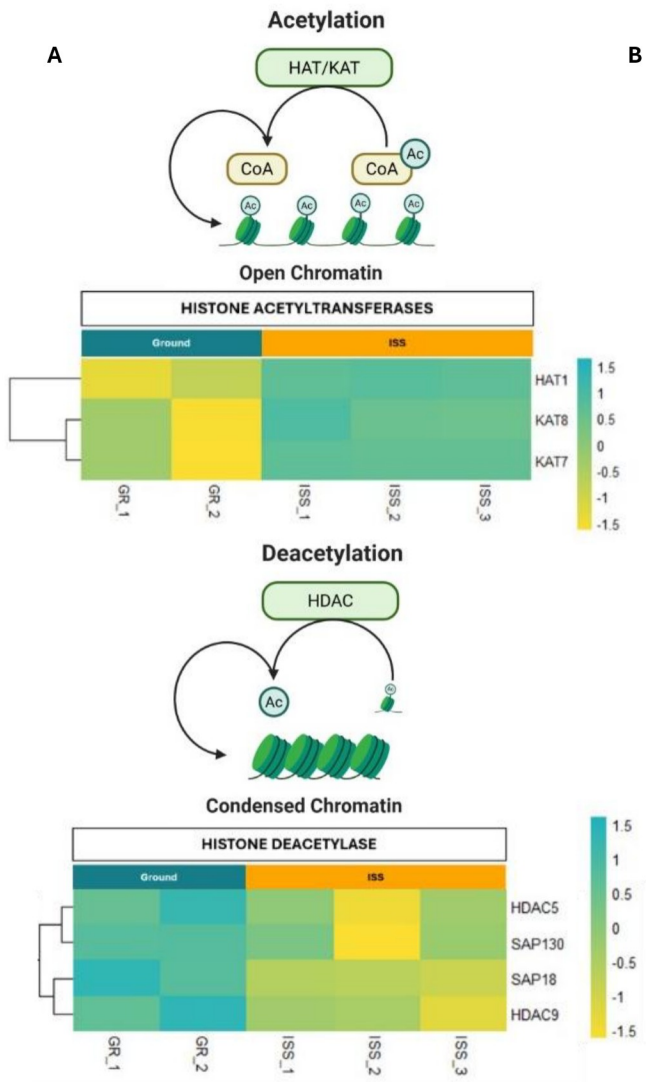
A
Acetylation
HAT/KAT
CoA
CoA
Ac
Open Chromatin
HISTONE ACETYLTRANSFERASES
Ground
ISS
HAT1
KAT8
KAT7
GR_1
GR_2
ISS_1
ISS_2
ISS_3
1.5
1
0.5
0
-0.5
-1
-1.5
Deacetylation
HDAC
Condensed Chromatin
HISTONE DEACETYLASE
HDAC5
SAP130
SAP18
HDAC9

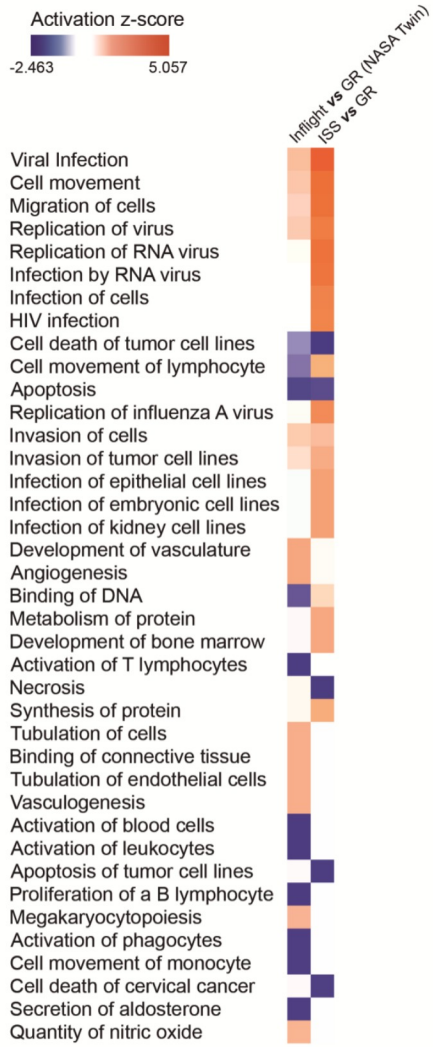
B
Activation z-score
-2.463
5.057
Inflight vs GR (NASA Twin)
ISS vs GR
Viral Infection
Cell movement
Migration of cells
Replication of virus
Replication of RNA virus
Infection by RNA virus
Infection of cells
HIV infection
Cell death of tumor cell lines
Cell movement of lymphocyte
Apoptosis
Replication of influenza A virus
Invasion of cells
Invasion of tumor cell lines
Infection of epithelial cell lines
Infection of embryonic cell lines
Infection of kidney cell lines
Development of vasculature
Angiogenesis
Binding of DNA
Metabolism of protein
Development of bone marrow
Activation of T lymphocytes
Necrosis
Synthesis of protein
Tubulation of cells
Binding of connective tissue
Tubulation of endothelial cells
Vasculogenesis
Activation of blood cells
Activation of leukocytes
Apoptosis of tumor cell lines
Proliferation of a B lymphocyte
Megakaryocytopoiesis
Activation of phagocytes
Cell movement of monocyte
Cell death of cervical cancer
Secretion of aldosterone
Quantity of nitric oxide

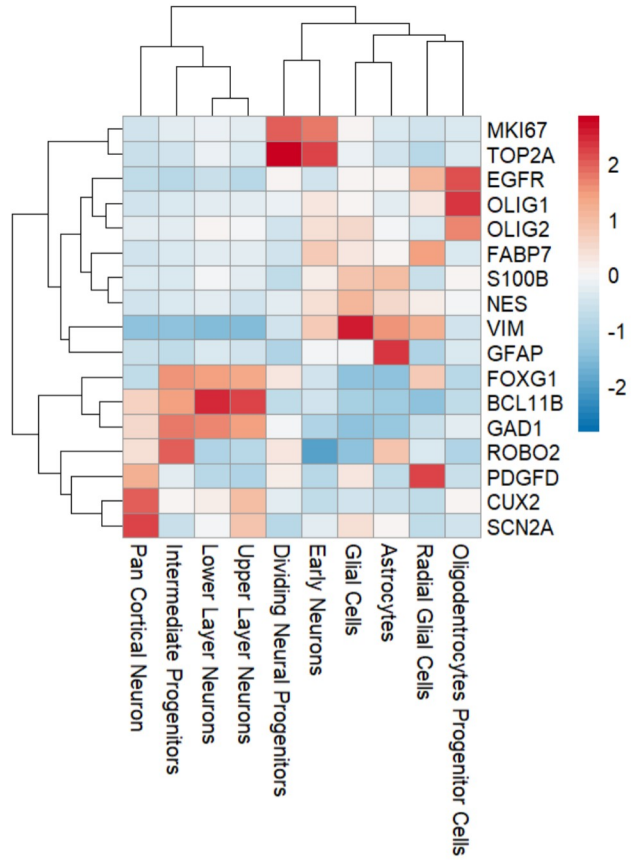
C
MKI67
TOP2A
EGFR
OLIG1
OLIG2
FABP7
S100B
NES
VIM
GFAP
FOXG1
BCL11B
GAD1
ROBO2
PDGFD
CUX2
SCN2A
Pan Cortical Neuron
Intermediate Progenitors
Lower Layer Neurons
Upper Layer Neurons
Dividing Neural Progenitors
Early Neurons
Glial Cells
Astrocytes
Radial Glial Cells
Oligodentrocytes Progenitor Cells
2
1
0
-1
-2

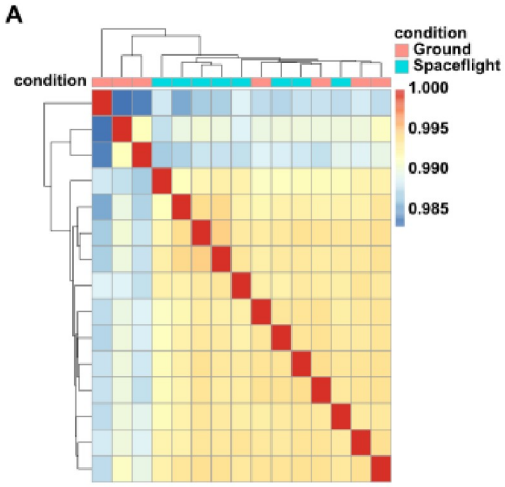
A
condition
condition
Ground
Spaceflight
1.000
0.995
0.990
0.985

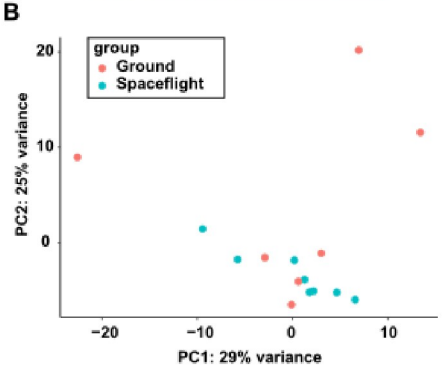
B
group
Ground
Spaceflight
PC2: 25% variance
PC1: 29% variance
20
10
0
−20
−10
0
10

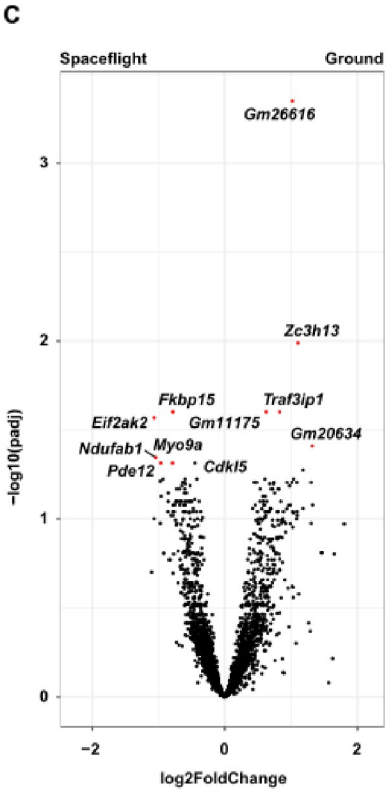
C
Spaceflight
Ground
Gm26616
Zc3h13
Fkbp15
Traf3ip1
Eif2ak2
Gm11175
Gm20634
Ndufab1
Myo9a
Pde12
Cdkl5
−log10(padj)
log2FoldChange
3
2
1
0
−2
0
2

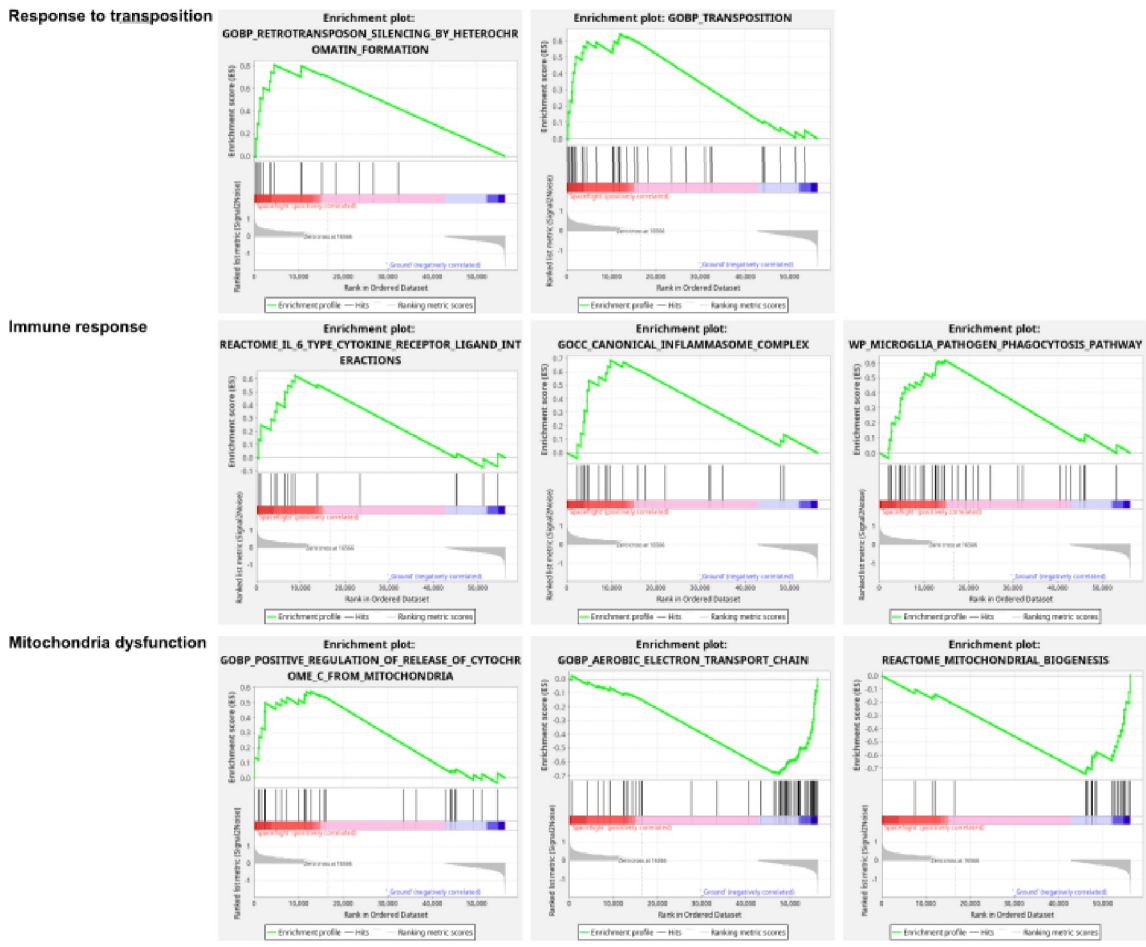
D
Response to transposition
Enrichment plot: GOBP_RETROTRANSPOSON_SILENCING_BY_HETEROCHROMATIN_FORMATION
Enrichment plot: GOBP_TRANSPOSITION
Immune response
Enrichment plot: REACTOME_IL_6_TYPE_CYTOKINE_RECEPTOR_LIGAND_INTERACTIONS
Enrichment plot: GOCC_CANONICAL_INFLAMMASOME_COMPLEX
Enrichment plot: WP_MICROGLIA_PATHOGEN_PHAGOCYTOSIS_PATHWAY
Mitochondria dysfunction
Enrichment plot: GOBP_POSITIVE_REGULATION_OF_RELEASE_OF_CYTOCHROME_C_FROM_MITOCHONDRIA
Enrichment plot: GOBP_AEROBIC_ELECTRON_TRANSPORT_CHAIN
Enrichment plot: REACTOME_MITOCHONDRIAL_BIOGENESIS

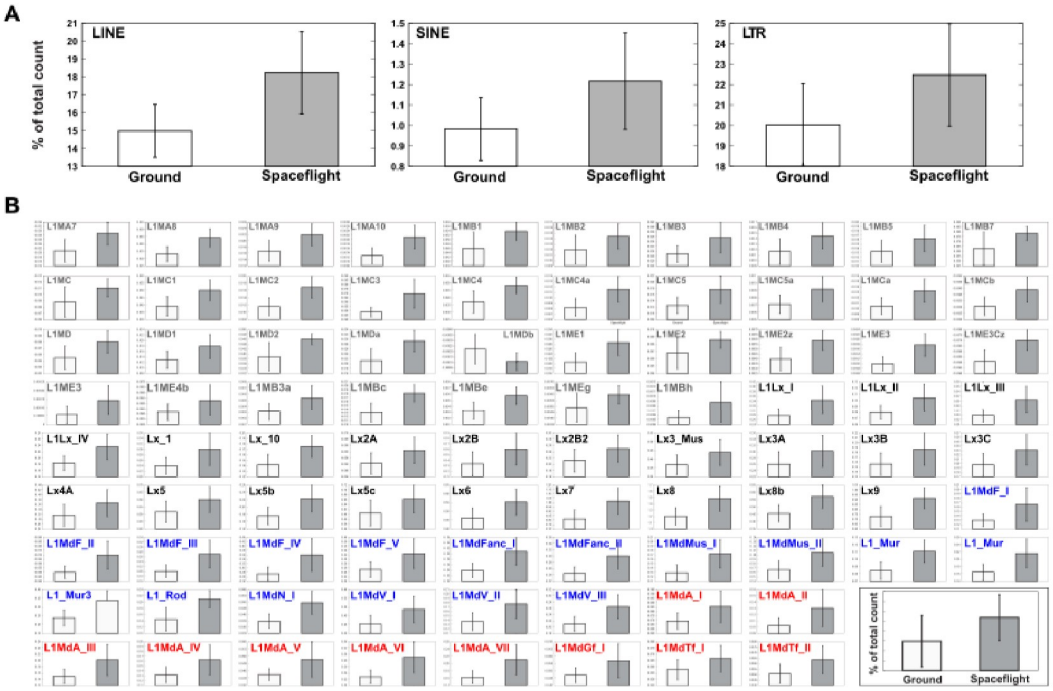
A
LINE
SINE
LTR
% of total count
Ground
Spaceflight
B
L1MA7
L1MA8
L1MA9
L1MA10
L1MB1
L1MB2
L1MB3
L1MB4
L1MB5
L1MB7
L1MC
L1MC1
L1MC2
L1MC3
L1MC4
L1MC4a
L1MC5
L1MC5a
L1MCa
L1MCb
L1MD
L1MD1
L1MD2
L1MDa
L1MDb
L1ME1
L1ME2
L1ME2z
L1ME3
L1ME3Cz
L1ME3
L1ME4b
L1MB3a
L1MBc
L1MBe
L1MEg
L1MBh
L1Lx_I
L1Lx_II
L1Lx_III
L1Lx_IV
Lx_1
Lx_10
Lx2A
Lx2B
Lx2B2
Lx3_Mus
Lx3A
Lx3B
Lx3C
Lx4A
Lx5
Lx5b
Lx5c
Lx6
Lx7
Lx8
Lx8b
Lx9
L1MdF_I
L1MdF_II
L1MdF_III
L1MdF_IV
L1MdF_V
L1MdFanc_I
L1MdFanc_II
L1MdMus_I
L1MdMus_II
L1_Mur
L1_Mur
L1_Mur3
L1_Rod
L1MdN_I
L1MdV_I
L1MdV_II
L1MdV_III
L1MdA_I
L1MdA_II
L1MdA_III
L1MdA_IV
L1MdA_V
L1MdA_VI
L1MdA_VII
L1MdGf_I
L1MdTf_I
L1MdTf_II
% of total count
Ground
Spaceflight
C
LINE
SINE
LTR
% of total count
Mock
Radiation
D
L1MA10
L1MB5
L1MB7
L1MC
L1MC3
L1MC5a
L1MD
L1ME3G
L1ME4c
L1MEb
L1MEf
Lx2AI
Lx2B
Lx5b
Lx7
Lx9
L1Lx_III
L1_Mur1
L1_Rod
L1MdF_II
L1MdV_IIII
L1MdA_V
% of total count
Mock
Radiation

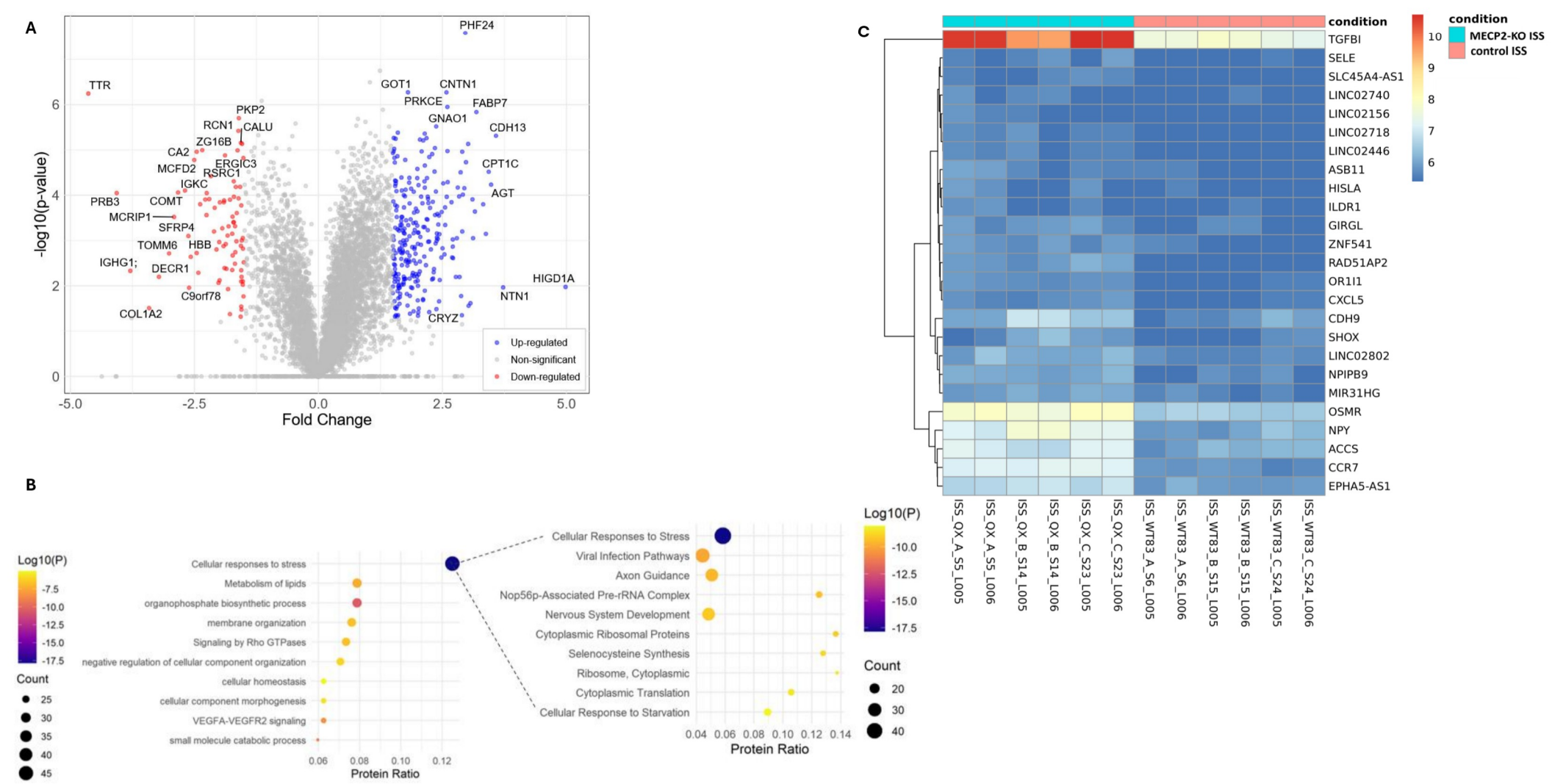
A
PHF24
TTR
GOT1
CNTN1
PRKCE
FABP7
PKP2
GNAO1
RCN1
CALU
CDH13
ZG16B
CA2
ERGIC3
CPT1C
MCFD2
RSRC1
IGKC
AGT
PRB3
COMT
MCRIP1
SFRP4
TOMM6
HBB
IGHG1;
DECR1
HIGD1A
C9orf78
NTN1
COL1A2
CRYZ
Up-regulated
Non-significant
Down-regulated
-log10(p-value)
Fold Change
B
Log10(P)
Count
Cellular responses to stress
Metabolism of lipids
organophosphate biosynthetic process
membrane organization
Signaling by Rho GTPases
negative regulation of cellular component organization
cellular homeostasis
cellular component morphogenesis
VEGFA-VEGFR2 signaling
small molecule catabolic process
Protein Ratio
Cellular Responses to Stress
Viral Infection Pathways
Axon Guidance
Nop56p-Associated Pre-rRNA Complex
Nervous System Development
Cytoplasmic Ribosomal Proteins
Selenocysteine Synthesis
Ribosome, Cytoplasmic
Cytoplasmic Translation
Cellular Response to Starvation
Protein Ratio
Log10(P)
Count
C
condition
MECP2-KO ISS
control ISS
TGFBI
SELE
SLC45A4-AS1
LINC02740
LINC02156
LINC02718
LINC02446
ASB11
HISLA
ILDR1
GIRGL
ZNF541
RAD51AP2
OR1I1
CXCL5
CDH9
SHOX
LINC02802
NPIPB9
MIR31HG
OSMR
NPY
ACCS
CCR7
EPHA5-AS1
ISS_QX_A_S5_L005
ISS_QX_A_S5_L006
ISS_QX_B_S14_L005
ISS_QX_B_S14_L006
ISS_QX_C_S23_L005
ISS_QX_C_S23_L006
ISS_WT83_A_S6_L005
ISS_WT83_A_S6_L006
ISS_WT83_B_S15_L005
ISS_WT83_B_S15_L006
ISS_WT83_C_S24_L005
ISS_WT83_C_S24_L006

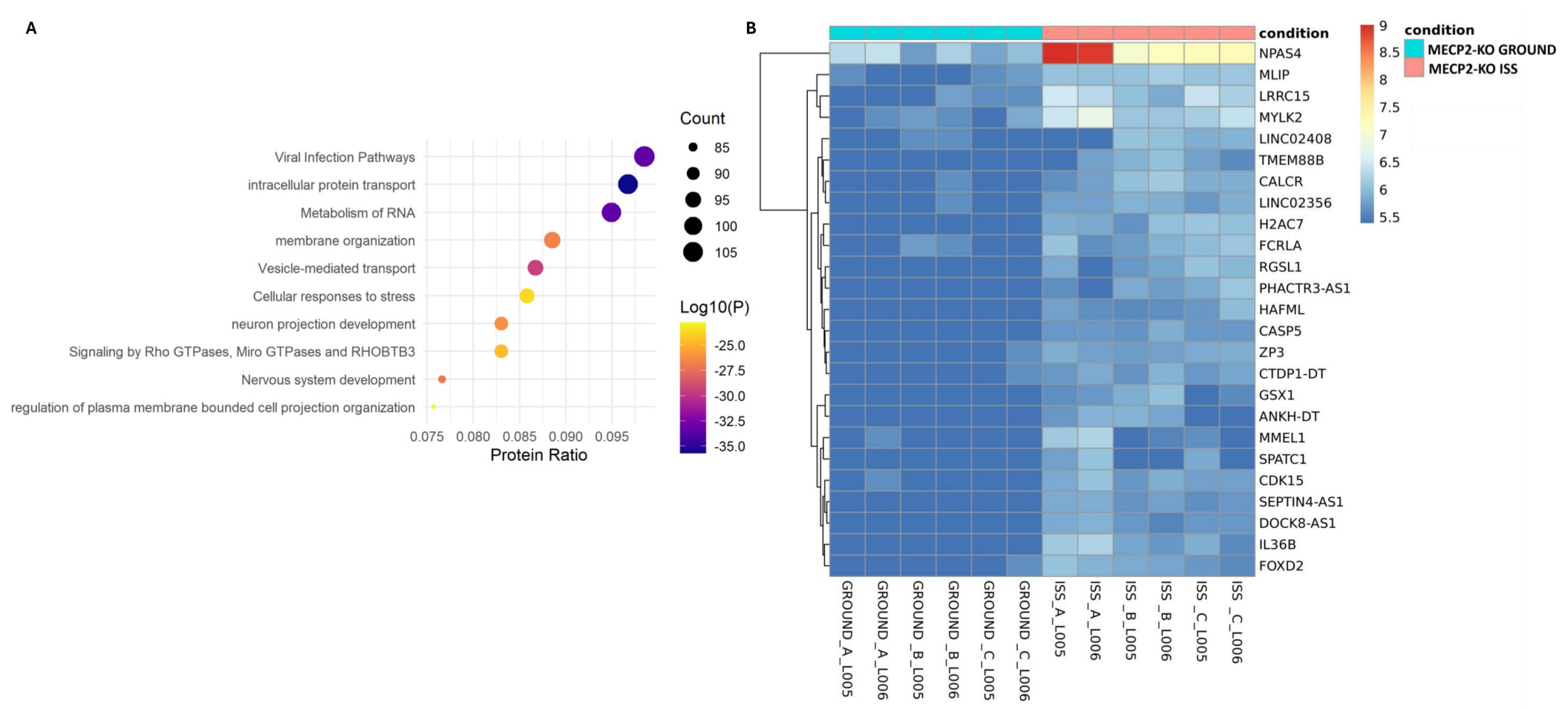
A
Viral Infection Pathways
intracellular protein transport
Metabolism of RNA
membrane organization
Vesicle-mediated transport
Cellular responses to stress
neuron projection development
Signaling by Rho GTPases, Miro GTPases and RHOBTB3
Nervous system development
regulation of plasma membrane bounded cell projection organization
0.075 0.080 0.085 0.090 0.095
Protein Ratio
Count
85
90
95
100
105
Log10(P)
-25.0
-27.5
-30.0
-32.5
-35.0
B
condition
NPAS4
MLIP
LRRC15
MYLK2
LINC02408
TMEM88B
CALCR
LINC02356
H2AC7
FCRLA
RGSL1
PHACTR3-AS1
HAFML
CASP5
ZP3
CTDP1-DT
GSX1
ANKH-DT
MMEL1
SPATC1
CDK15
SEPTIN4-AS1
DOCK8-AS1
IL36B
FOXD2
GROUND_A_L005
GROUND_A_L006
GROUND_B_L005
GROUND_B_L006
GROUND_C_L005
GROUND_C_L006
ISS_A_L005
ISS_A_L006
ISS_B_L005
ISS_B_L006
ISS_C_L005
ISS_C_L006
9
8.5
8
7.5
7
6.5
6
5.5
condition
MECP2-KO GROUND
MECP2-KO ISS

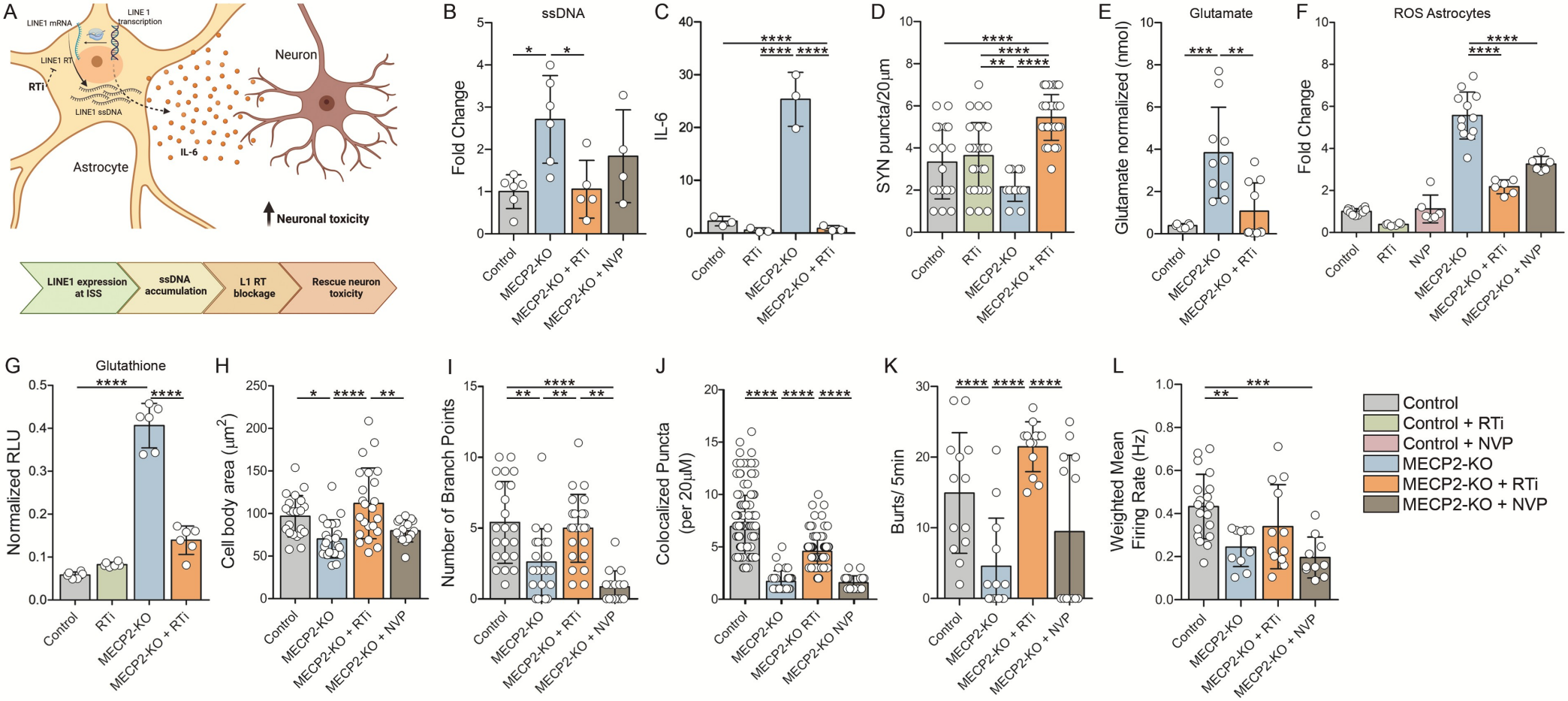
A
LINE1 mRNA
LINE 1 transcription
LINE1 RT
RTi
LINE1 ssDNA
IL-6
Neuron
Astrocyte
Neuronal toxicity
LINE1 expression at ISS
ssDNA accumulation
L1 RT blockage
Rescue neuron toxicity
B
ssDNA
Fold Change
Control
MECP2-KO
MECP2-KO + RTi
MECP2-KO + NVP
C
IL-6
Control
RTi
MECP2-KO
MECP2-KO + RTi
D
SYN puncta/20µm
Control
RTi
MECP2-KO
MECP2-KO + RTi
E
Glutamate
Glutamate normalized (nmol)
Control
MECP2-KO
MECP2-KO + RTi
F
ROS Astrocytes
Fold Change
Control
RTi
NVP
MECP2-KO
MECP2-KO + RTi
MECP2-KO + NVP
G
Glutathione
Normalized RLU
Control
RTi
MECP2-KO
MECP2-KO + RTi
H
Cell body area (µm2)
Control
MECP2-KO
MECP2-KO + RTi
MECP2-KO + NVP
I
Number of Branch Points
Control
MECP2-KO
MECP2-KO + RTi
MECP2-KO + NVP
J
Colocalized Puncta (per 20µM)
Control
MECP2-KO
MECP2-KO RTi
MECP2-KO NVP
K
Burts/ 5min
Control
MECP2-KO
MECP2-KO + RTi
MECP2-KO + NVP
L
Weighted Mean Firing Rate (Hz)
Control
MECP2-KO
MECP2-KO + RTi
MECP2-KO + NVP
Control
Control + RTi
Control + NVP
MECP2-KO
MECP2-KO + RTi
MECP2-KO + NVP

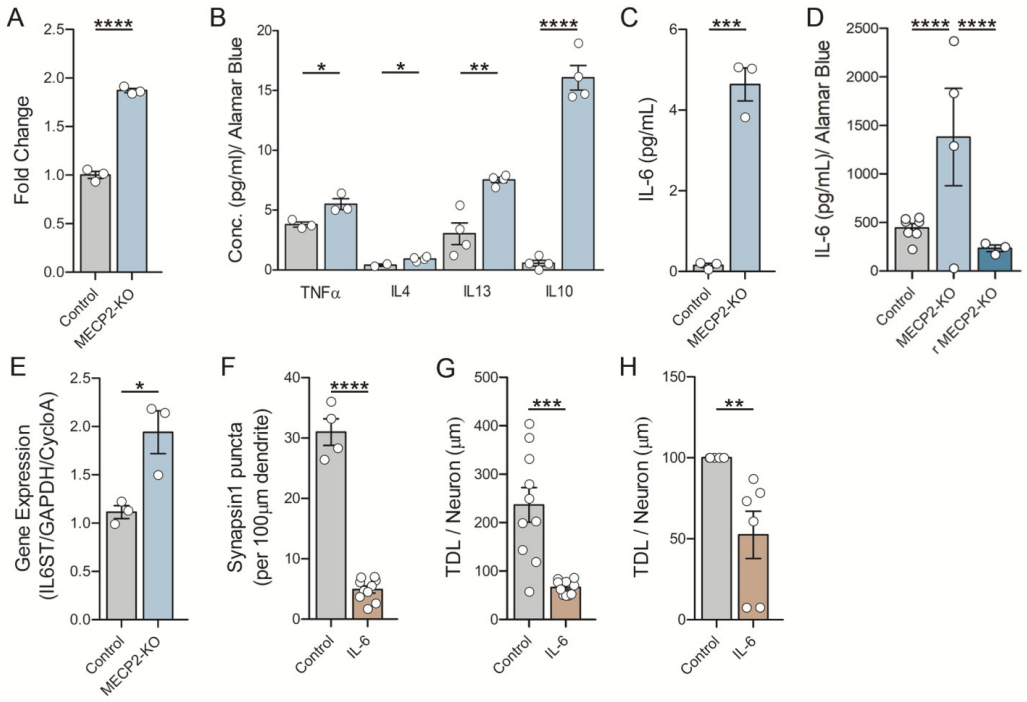
A
Fold Change
2.5
2.0
1.5
1.0
0.5
0.0
****
Control
MECP2-KO
B
Conc. (pg/ml)/ Alamar Blue
20
15
10
5
0
*
*
**
****
TNFα
IL4
IL13
IL10
C
IL-6 (pg/mL)
6
4
2
0
***
Control
MECP2-KO
D
IL-6 (pg/mL)/ Alamar Blue
2500
2000
1500
1000
500
0
****
****
Control
MECP2-KO
r MECP2-KO
E
Gene Expression
(IL6ST/GAPDH/CycloA)
2.5
2.0
1.5
1.0
0.5
0.0
*
Control
MECP2-KO
F
Synapsin1 puncta
(per 100μm dendrite)
40
30
20
10
0
****
Control
IL-6
G
TDL / Neuron (μm)
500
400
300
200
100
0
***
Control
IL-6
H
TDL / Neuron (μm)
150
100
50
0
**
Control
IL-6

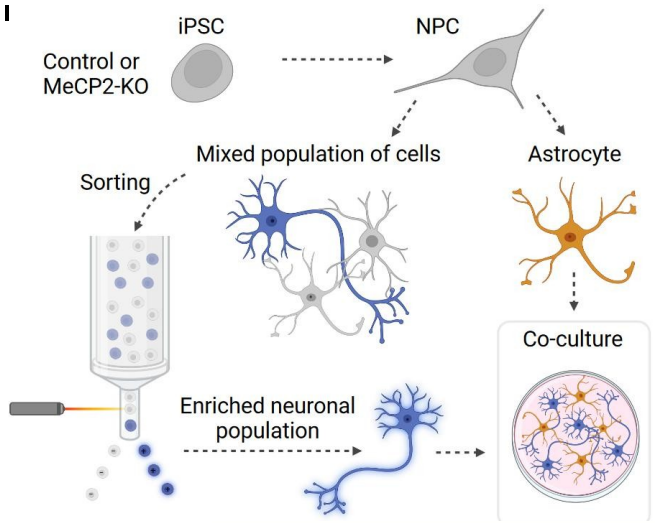
I
iPSC
NPC
Control or
MeCP2-KO
Mixed population of cells
Astrocyte
Sorting
Co-culture
Enriched neuronal
population

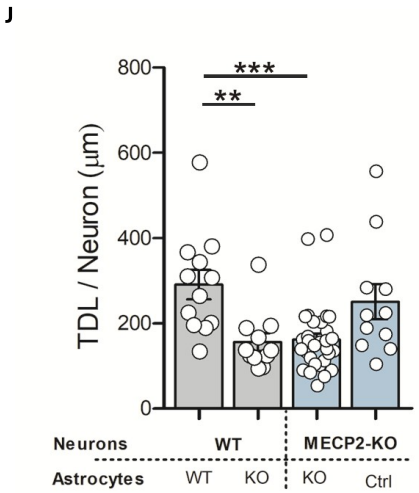
J
TDL / Neuron (µm)
800
600
400
200
0
***
**
Neurons
WT
MECP2-KO
Astrocytes
WT
KO
KO
Ctrl

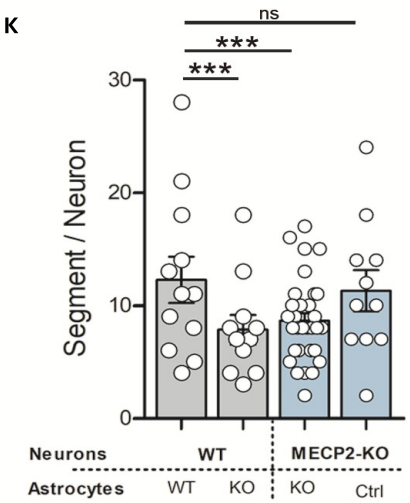
K
Segment / Neuron
30
20
10
0
ns
***
***
Neurons
WT
MECP2-KO
Astrocytes
WT
KO
KO
Ctrl

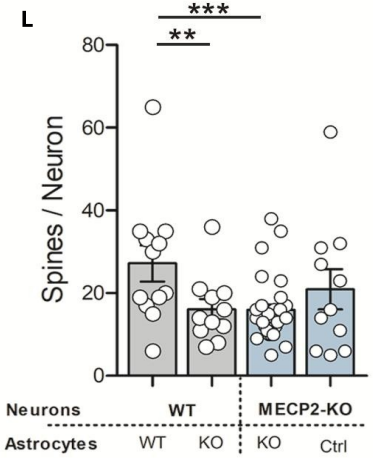
L
Spines / Neuron
80
60
40
20
0
***
**
Neurons
WT
MECP2-KO
Astrocytes
WT
KO
KO
Ctrl

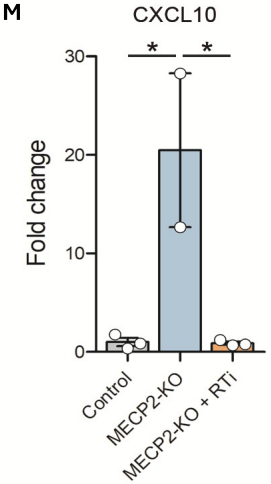
M
CXCL10
Fold change
30
20
10
0
*
*
Control
MECP2-KO
MECP2-KO + RTi

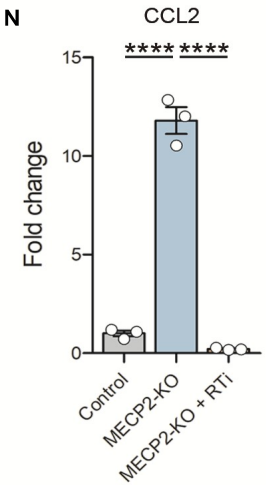
N
CCL2
Fold change
15
10
5
0
****
****
Control
MECP2-KO
MECP2-KO + RTi

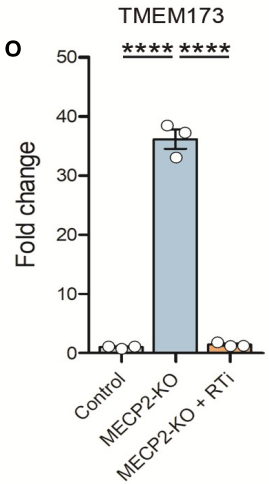
O
TMEM173
Fold change
50
40
30
20
10
0
****
****
Control
MECP2-KO
MECP2-KO + RTi

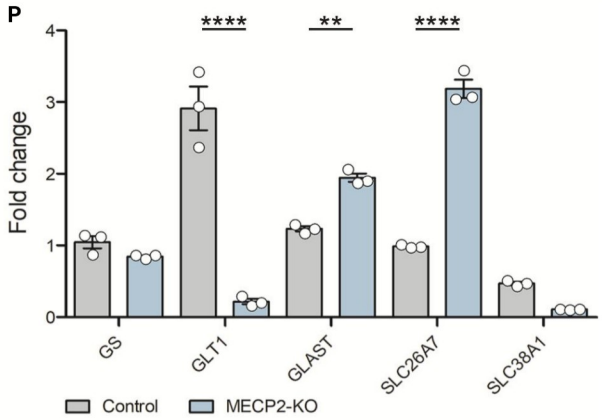
P
Fold change
****
**
****
GS
GLT1
GLAST
SLC26A7
SLC38A1
Control
MECP2-KO

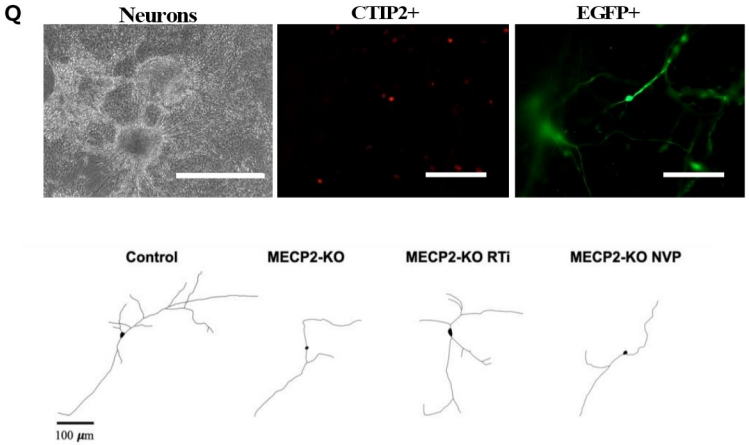
Q
Neurons
CTIP2+
EGFP+
Control
MECP2-KO
MECP2-KO RTi
MECP2-KO NVP
100 μm

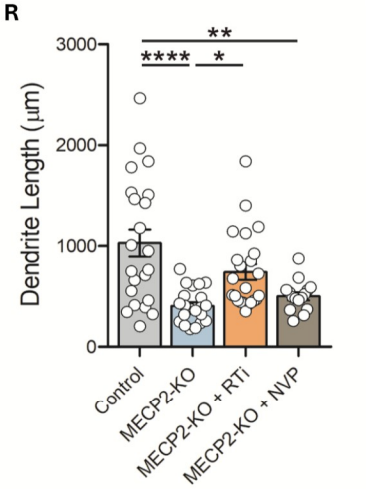
R
Dendrite Length (μm)
**
****
*
Control
MECP2-KO
MECP2-KO + RTi
MECP2-KO + NVP

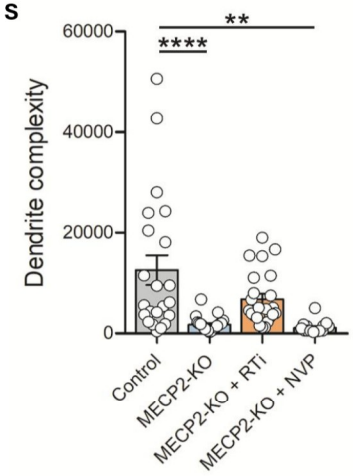
S
Dendrite complexity
**
****
Control
MECP2-KO
MECP2-KO + RTi
MECP2-KO + NVP

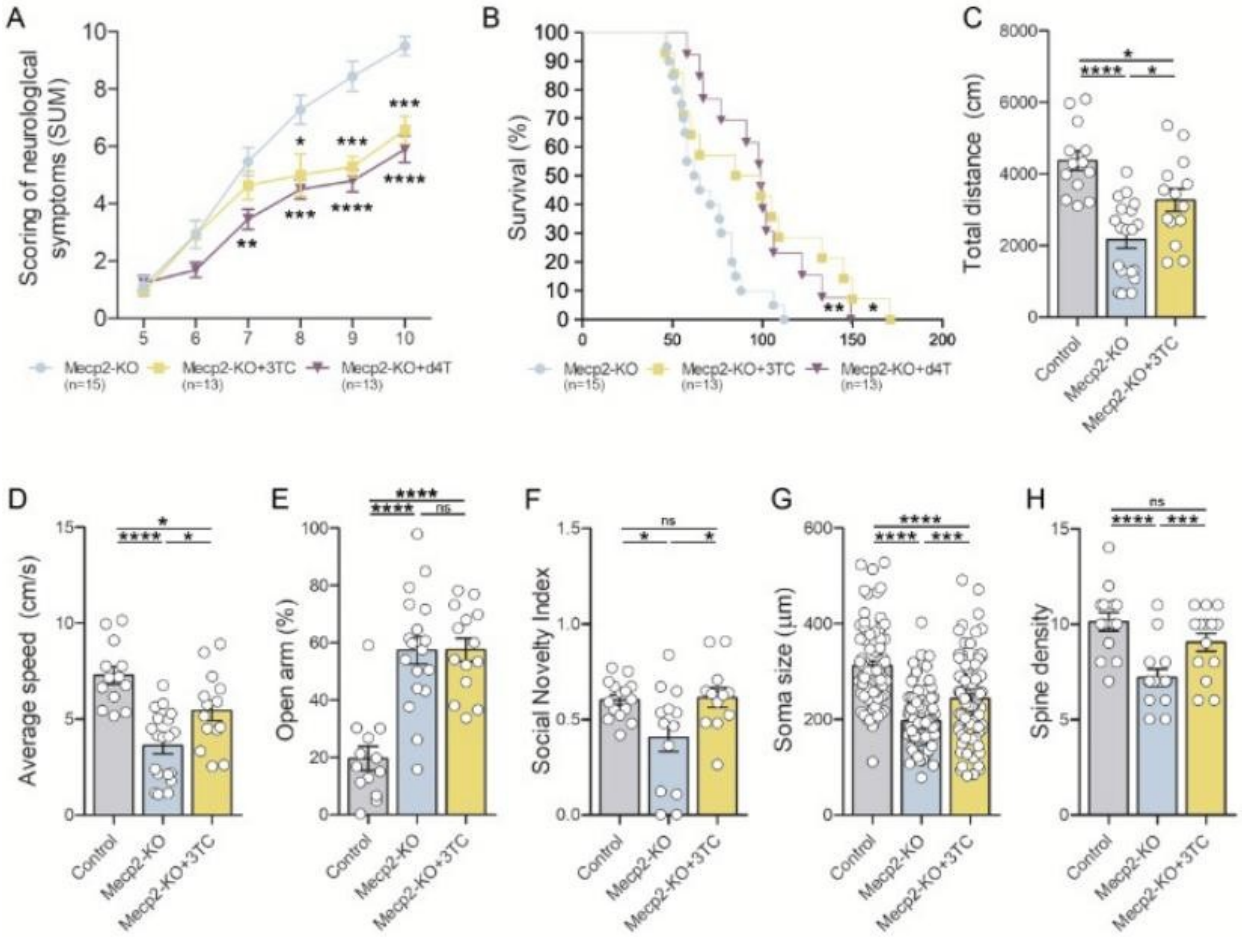
A
Scoring of neurological symptoms (SUM)
Mecp2-KO (n=15)
Mecp2-KO+3TC (n=13)
Mecp2-KO+d4T (n=13)
B
Survival (%)
C
Total distance (cm)
Control
Mecp2-KO
Mecp2-KO+3TC
D
Average speed (cm/s)
E
Open arm (%)
F
Social Novelty Index
G
Soma size (μm)
H
Spine density

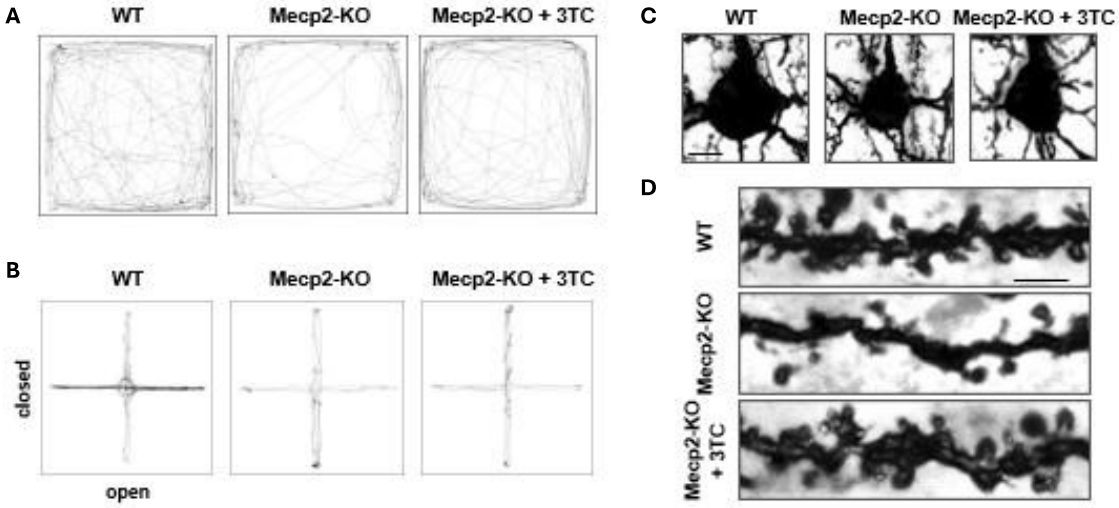
A
WT
Mecp2-KO
Mecp2-KO + 3TC
B
WT
Mecp2-KO
Mecp2-KO + 3TC
closed
open
C
WT
Mecp2-KO
Mecp2-KO + 3TC
D
WT
Mecp2-KO
Mecp2-KO + 3TC

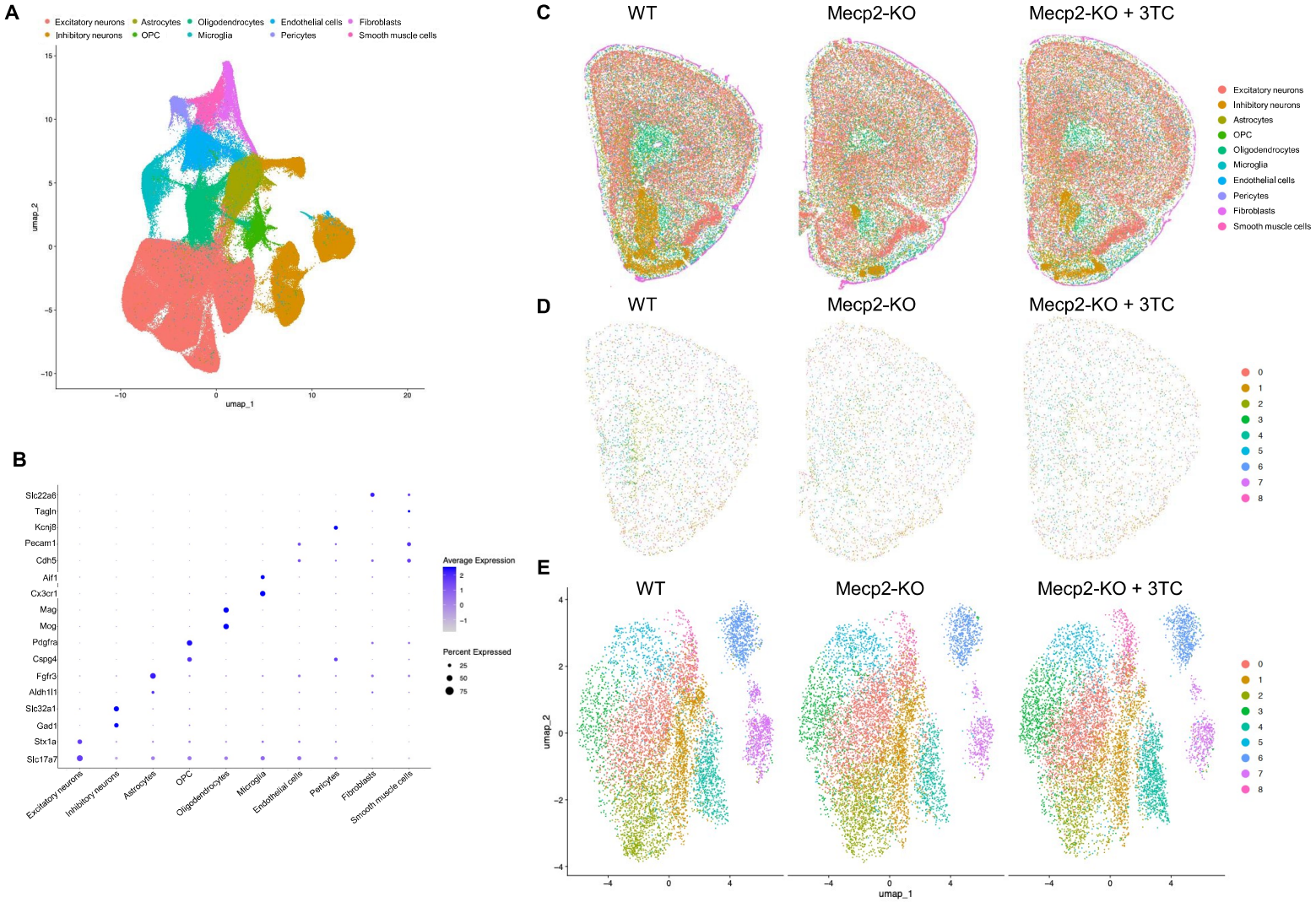
A
Excitatory neurons
Inhibitory neurons
Astrocytes
OPC
Oligodendrocytes
Microglia
Endothelial cells
Pericytes
Fibroblasts
Smooth muscle cells
umap_1
umap_2
B
Slc22a6
Tagln
Kcnj8
Pecam1
Cdh5
Aif1
Cx3cr1
Mag
Mog
Pdgfra
Cspg4
Fgfr3
Aldh1l1
Slc32a1
Gad1
Stx1a
Slc17a7
Average Expression
Percent Expressed
C
WT
Mecp2-KO
Mecp2-KO + 3TC
D
E
umap_1
umap_2

F
carboxylic acid metabolic process
oxoacid metabolic process
carbohydrate metabolic process
negative regulation of intracellular signal transduction
Wnt signaling pathway
cell−cell signaling by wnt
generation of precursor metabolites and energy
hexose metabolic process
monosaccharide metabolic process
small molecule biosynthetic process
response to oxygen levels
response to hypoxia
positive regulation of small molecule metabolic process
small molecule catabolic process
cellular response to oxygen levels
cellular response to hypoxia
negative regulation of transmembrane transport
somatic stem cell population maintenance
gluconeogenesis
hexose biosynthetic process
glycolytic process
ATP generation from ADP
regulation of fatty acid metabolic process
nucleoside diphosphate phosphorylation
nucleotide phosphorylation
positive regulation of gluconeogenesis
positive regulation of transcription from RNA polymerase II promoter involved in cellular response to chemical stimulus
regulation of transcription from RNA polymerase II promoter in response to oxidative stress
response to interleukin−7
cellular response to interleukin−7
0.05
0.10
0.15
GeneRatio

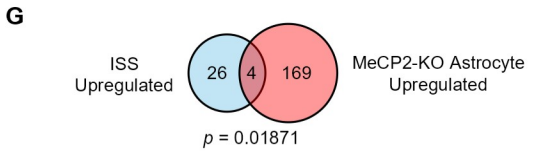
G
ISS Upregulated
26
4
169
MeCP2-KO Astrocyte Upregulated
p = 0.01871

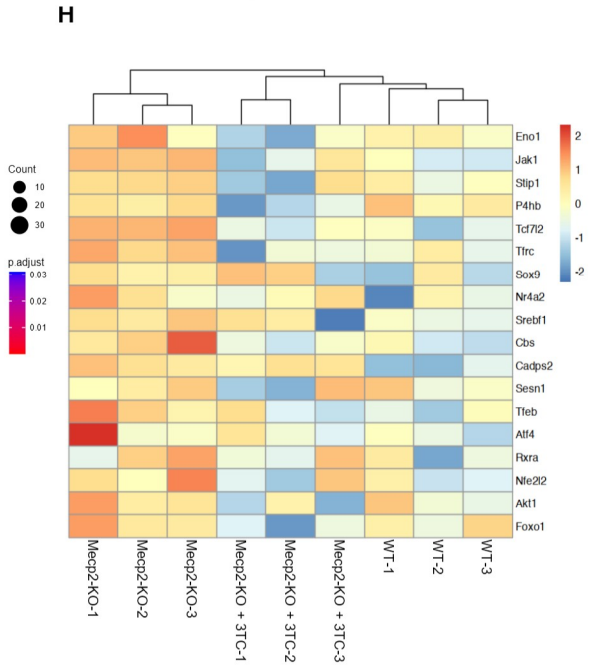
H
Count
10
20
30
p.adjust
0.03
0.02
0.01
Eno1
Jak1
Stip1
P4hb
Tcf7l2
Tfrc
Sox9
Nr4a2
Srebf1
Cbs
Cadps2
Sesn1
Tfeb
Atf4
Rxra
Nfe2l2
Akt1
Foxo1
2
1
0
-1
-2
Mecp2-KO-1
Mecp2-KO-2
Mecp2-KO-3
Mecp2-KO + 3TC-1
Mecp2-KO + 3TC-2
Mecp2-KO + 3TC-3
WT-1
WT-2
WT-3

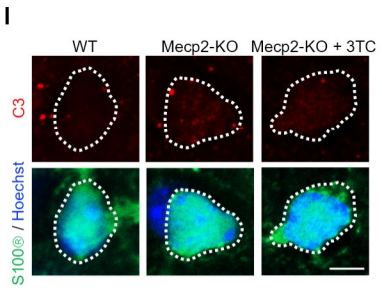
I
WT
Mecp2-KO
Mecp2-KO + 3TC
C3
S100® / Hoechst

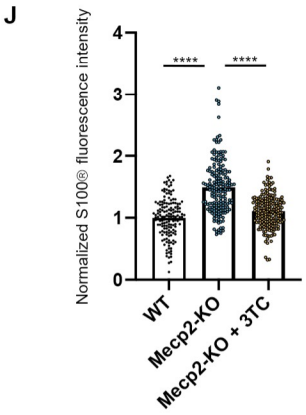
J
Normalized S100® fluorescence intensity
4
3
2
1
0
****
****
WT
Mecp2-KO
Mecp2-KO + 3TC

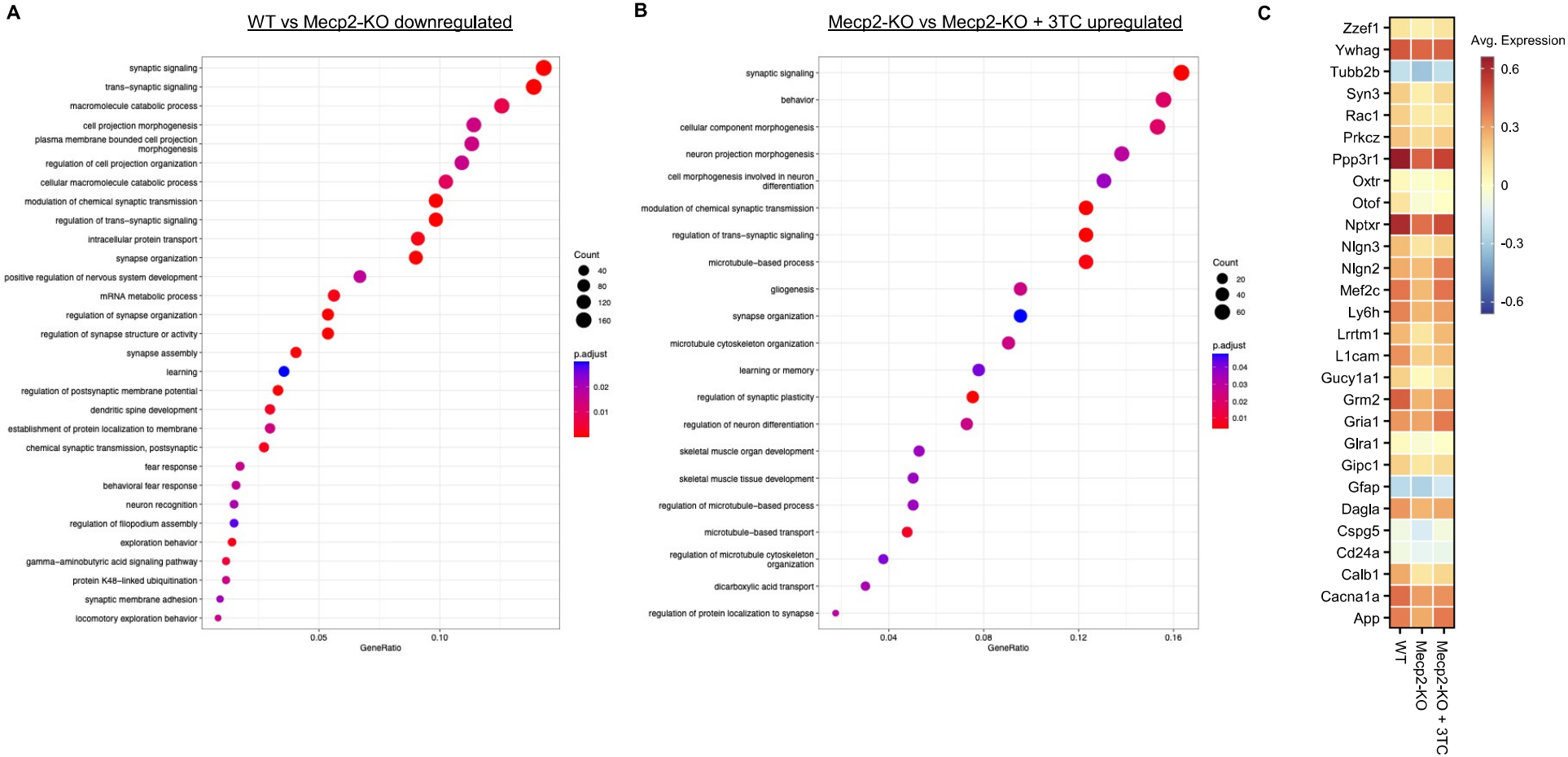
A
WT vs Mecp2-KO downregulated
synaptic signaling
trans−synaptic signaling
macromolecule catabolic process
cell projection morphogenesis
plasma membrane bounded cell projection morphogenesis
regulation of cell projection organization
cellular macromolecule catabolic process
modulation of chemical synaptic transmission
regulation of trans−synaptic signaling
intracellular protein transport
synapse organization
positive regulation of nervous system development
mRNA metabolic process
regulation of synapse organization
regulation of synapse structure or activity
synapse assembly
learning
regulation of postsynaptic membrane potential
dendritic spine development
establishment of protein localization to membrane
chemical synaptic transmission, postsynaptic
fear response
behavioral fear response
neuron recognition
regulation of filopodium assembly
exploration behavior
gamma−aminobutyric acid signaling pathway
protein K48−linked ubiquitination
synaptic membrane adhesion
locomotory exploration behavior
0.05
0.10
GeneRatio
Count
40
80
120
160
p.adjust
0.02
0.01
B
Mecp2-KO vs Mecp2-KO + 3TC upregulated
synaptic signaling
behavior
cellular component morphogenesis
neuron projection morphogenesis
cell morphogenesis involved in neuron differentiation
modulation of chemical synaptic transmission
regulation of trans−synaptic signaling
microtubule−based process
gliogenesis
synapse organization
microtubule cytoskeleton organization
learning or memory
regulation of synaptic plasticity
regulation of neuron differentiation
skeletal muscle organ development
skeletal muscle tissue development
regulation of microtubule−based process
microtubule−based transport
regulation of microtubule cytoskeleton organization
dicarboxylic acid transport
regulation of protein localization to synapse
0.04
0.08
0.12
0.16
GeneRatio
Count
20
40
60
p.adjust
0.04
0.03
0.02
0.01
C
Zzef1
Ywhag
Tubb2b
Syn3
Rac1
Prkcz
Ppp3r1
Oxtr
Otof
Nptxr
Nlgn3
Nlgn2
Mef2c
Ly6h
Lrrtm1
L1cam
Gucy1a1
Grm2
Gria1
Glra1
Gipc1
Gfap
Dagla
Cspg5
Cd24a
Calb1
Cacna1a
App
WT
Mecp2-KO
Mecp2-KO + 3TC
Avg. Expression
0.6
0.3
0
-0.3
-0.6

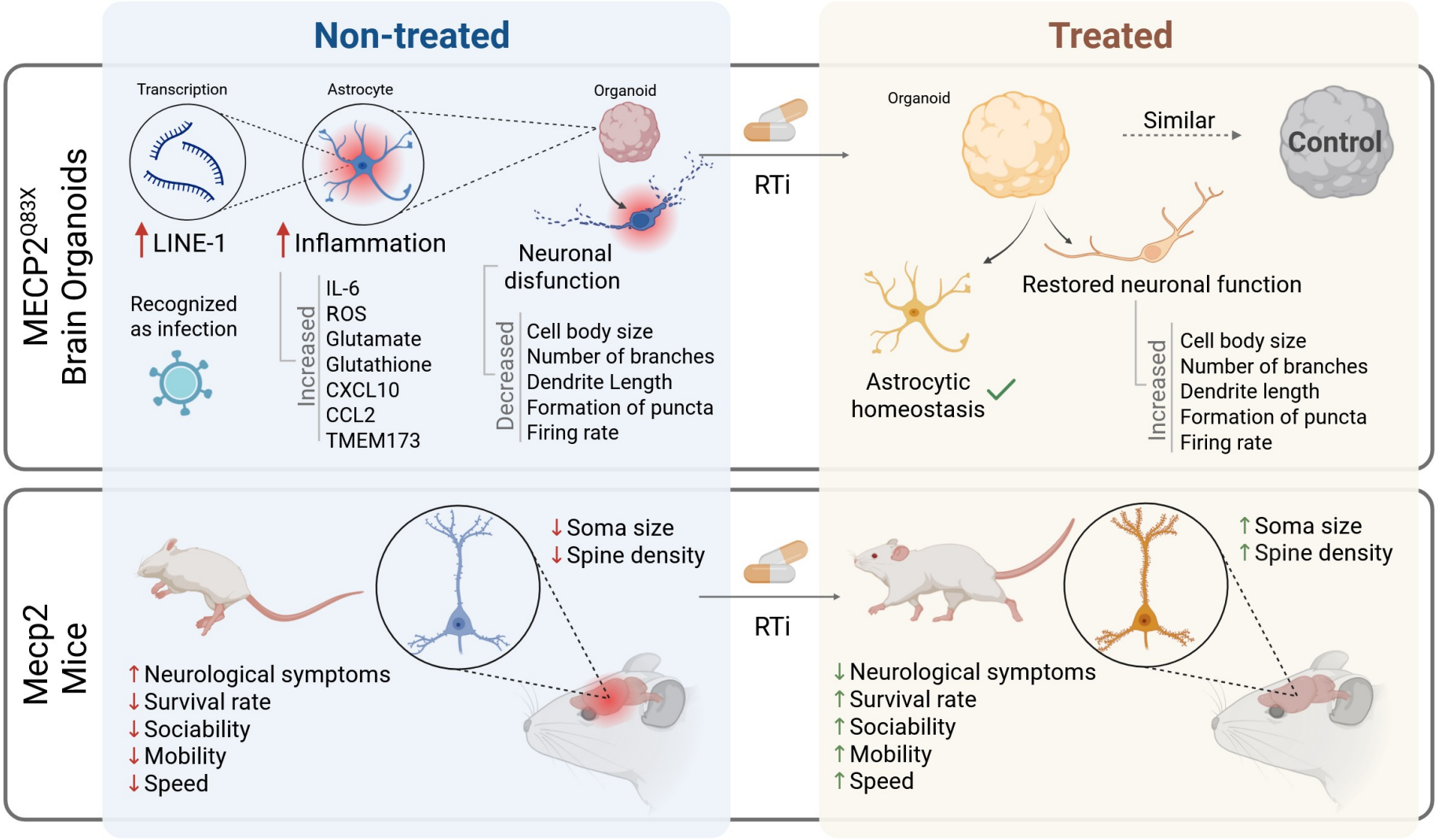
Non-treated
Treated
MECP2Q83X Brain Organoids
Transcription
Astrocyte
Organoid
LINE-1
Inflammation
Neuronal disfunction
Recognized as infection
Increased
IL-6
ROS
Glutamate
Glutathione
CXCL10
CCL2
TMEM173
Decreased
Cell body size
Number of branches
Dendrite Length
Formation of puncta
Firing rate
RTi
Organoid
Similar
Control
Restored neuronal function
Astrocytic homeostasis
Increased
Cell body size
Number of branches
Dendrite length
Formation of puncta
Firing rate
Mecp2 Mice
Soma size
Spine density
Neurological symptoms
Survival rate
Sociability
Mobility
Speed
RTi
Soma size
Spine density
Neurological symptoms
Survival rate
Sociability
Mobility
Speed